NMR STUDY OF EXCHANGE AND HYDRATION SITE IDENTIFICATION IN MCM-41

by

Jamal Hassan

A thesis
presented to the University of Waterloo
in fulfillment of the
thesis requirement for the degree of
Doctor of Philosophy
in
Physics

Waterloo, Ontario, Canada 2006

I hereby declare that I am the sole author of this thesis. This is a true copy of the thesis, including any required final revisions, as accepted by my examiners.

I understand that my thesis may be made electronically available to the public.

Abstract

Deuteron 1D and 2D NMR spectroscopy was used to study the dynamics of water molecules within the mesoporous material MCM-41. The deuteron spectra show three magnetization components for a sample hydrated to a 0.2 monolayer level. One component was assigned to the pore surface silanol group deuterons that exhibit a broad Gaussian line of 32.6 kHz FWHM and the other components were assigned to the water deuterons. At room temperature one water deuteron component has a powder-pattern line shape (splitting of about 4.2 kHz and population of about 61%) and the other has a Lorentzian line shape (about 388 Hz FWHM and population of 39%). Magnetization exchange occurs between these components. An exchange model, based on multi-site exchange, was constructed and used to analyse the results for exchange. For the 0.2 monolayer sample the rate of magnetization exchange out of the hydration site, where the water deuterons exhibit a Lorentzian line in the ^{2}H spectra is, 1.3 ms^{-1}. 2D measurements at 233 K and room temperature confirmed the magnetization exchange scenario for the two water deuteron sites.

By combining the deuteron results with proton-silicon cross polarization magic angle spinning experiments, together with heat treatment of the sample, definitive hydration site identification for MCM-41 was achieved. This study has shown that the water molecules bound to the hydrogen-bonded silanol groups produce the powder pattern while water molecules bound to the single silanol groups produce the Lorentzian line. This represents a necessary first step toward a meaningful modeling of NMR observables in terms of site-specific water molecule coordination and dynamics in MCM-41.

Acknowledgements

I would like to sincerely thank my supervisor Dr. H. Peemoeller for his valuable insights, enthusiasm, support and encouragements. I appreciate his time and effort which guided me through this research experience and provided me with valuable feedback on this thesis. I would like to thank my co-supervisor Dr. E. Reardon for his help and assistance.

I would like to thank all my program committee members: Dr. B.-Y. Ha, Dr. G. A. Scholz, and Dr. C. M. Hansson, for their time and comments on this thesis work. Also, I wish to thank Dr. A. D. Bain who accepted to be in my Ph.D. thesis defence.

My special appreciation to the administration staff of the Physics department, specially Judy McDonnell, the wonderful graduate secretary. My acknowledgment to all members of the NMR group, specially to Jianzhen Liang. He is a real friend and always there when needed. Most of the programs for simulation in this study were initiated by him. I would like to thank Firas Mansour who helped me prepare my first MCM-41 sample. Thanks to Rose Teymoori, Sean Jackson, Dr. R. Holly and Tingting Ren.

I am lucky to work with Dr. C. Lemaire. I always took his advice before starting a new experiment. Claude I would never forget your help.

I would like to thank my family back home, Kurdistan, for their unconditional faith in me and full support during tough times. Thanks to my brother and sister in U.K., and my mother, who taught me to be patient She taught me to be strong in face of adversities. Finally, I have special appreciation to my wife, Sawsan, who put up with lots of late nights and is always supportive. Without her care and love I would never have managed to complete this work. Also, I have to mention my son, Dylan, who came to this world during my Ph.D. program. He showed me the real beauty of life.

Dedication

To the good soul of my father

with all love and respect

Notation and Abbreviation

a.u.	arbitrary units
B_1	radio frequency magnetic field
B_o	Zeeman magnetic field
CP	cross polarization
CPMAS	cross polarization magic angle spinning
E_a	activation energy
FID	free induction decay
FWHM	full width at half maximum
H-bonded	hydrogen bonded
k_{ab}	magnetization exchange from site a to b
MAS	magic angle spinning
PAS	principle-axis-system
P_i	magnetization population of site i
R	direct spin-spin coupling constant
t_m	mixing time
T_s/T_L	spin temperature/lattice temperature
$Q^4/Q^3/Q^2$	silanol groups with zero/one/two hydrogens
V	magnetization exchange rate constant
$\underline{\underline{C}}$	spin-rotation interaction tensor
$\underline{\underline{J}}$	indirect spin-spin coupling tensor
$\underline{\underline{\sigma}}$	chemical shift interaction tensor
γ	gyromagnetic ratio
μ_o	permeability constant in vacuum
χ	quadrupolar coupling constant
$\Delta\nu_Q$	quadrupolar splitting
$\Delta\nu_G/\Delta\nu_L$	FWHM of Gaussian/FWHM of Lorentzian line
δ	chemical shift

Contents

List of Tables

List of Figures

Chapter 1

Introduction

The behaviour of water in the vicinity of surfaces and in confined geometries is of interest in various areas in science, engineering and medicine. For example, the physical properties of hygroscopic polymer based materials, the effectiveness of many catalysts or catalyst particles, multi-phase (oil and water) flow in rock reservoirs, ground water remediation, and the state of biomolecular, cellular and tissue components all involve water interacting with surfaces inside porous media. Although, the properties of bulk water have been studied for more than a century, their complete description is still being discovered, and water-surface interactions and confinement add complexity. Due to the complexity of water behaviour in real systems (e.g., biological tissue, cement, soil and rocks) investigations have resorted to studies of simpler model systems in order to shed light on the water molecule-surface site interaction. Model systems commonly utilized until recently (e.g., controlled pore glass) suffered from two important shortcomings: non-uniform pore sizes and many pore interconnections providing ill-defined geometries. This made data interpretation difficult.

MCM-41, a mesoporous material discovered in 1992 (this material will be fully described in chapter 4), is considered to be an excellent model system for the study of water in confined geometry due to its large internal surface area and its uniform pore structure. Many potential applications of the material involve an aqueous phase. In such cases water-surface interactions play an important role in

determining the properties of the systems of interest and in controlling catalysis, chemical reactions, and water mediated biological interactions. Although extensive literature exists on the elucidation of water molecule behaviour in MCM-41 controversy still surrounds various aspects of the hydration dynamics. These include the identification of hydration sites involved, the coordination, dynamics and residence times of water at such sites, as well as formation of different water phases with increasing hydration levels. There is also uncertainty about physical, chemical and magnetic exchange between phases, the influence of surface on structure and dynamics of water not directly associated with the surface.

Nuclear Magnetic Resonance (NMR) is considered one of the most important noninvasive tools for the study of surface and confinement effects on water. The main goal of the present study is to investigate water dynamics and the interactions of water with the different silanol groups in MCM-41 using NMR as the main physical technique.

This study includes detailed 1D and 2D deuteron NMR spectral measurements in dry and hydrated MCM-41 samples as a function of temperature. These measurements, combined with cross polarization MAS experiments in a heat-treated sample, and proton MAS measurements in selected MCM-41 samples hydrated with H_2O, are utilized to identify the surface silanol hydration sites and their relation to the water dynamics at these sites.

Chapter 2 presents basic theoretical background of NMR including magnetization exchange and the effect of motion on NMR line shapes. Some aspects about MCM-41 as well as a literature review are given in Chapter 3. The preparation and characterization of MCM-41 is presented in Chapter 4. This chapter also describes the different NMR experiments used in this study. Results and discussion of this research are presented in Chapter 5. The conclusions reached in this study with recommendations for future work are summarized in Chapter 6.

Chapter 2

NMR Theory

Introduction

The spin, I, of a nucleus is a multiple of 1/2 and given as I= n/2 where n= 0, 1, 2, ... For example, for protons (^{1}H), deuterons (^{2}H) and helium nuclei (^{4}He) the spin I= 1/2, 1, and 0, respectively. Nuclear Magnetic Resonance (NMR) is based on the interaction between nuclei of non-zero spin quantum number and magnetic fields. In the NMR experiment, the spins are placed in a magnetic field $\overrightarrow{\mathrm{B}_o} = \mathrm{B}_o\,\widehat{k}$ and due to the Zeeman interaction (discussed in more detail in section 2.1.1), a thermal equilibrium population of states will be established such that the lower energy levels are more populated than the upper energy levels. A net macroscopic magnetization $\overrightarrow{\mathrm{M}} = \mathrm{M}_o\,\widehat{k}$ results. As in other kinds of spectroscopy, in NMR one needs to perturb the equilibrium states of the energy levels and then record the response. In pulsed NMR, a Radio Frequency (RF) field is applied for a very short time. This results in $\overrightarrow{\mathrm{M}}$ being tipped away from $\widehat{k}$ or the Z-direction so as to have XY-components. The response of the nuclei is then recorded by detecting the time evolution of the magnetization in the XY-plane. The recorded signal is called Free Induction Decay (FID).

Vectorially, the time evolution of $\overrightarrow{\mathrm{M}}$ is given by the Bloch equations [1]

$$\begin{aligned} \frac{dM_z}{dt} &= -\frac{(M_z - M_o)}{T_1} \\ \frac{dM_x}{dt} &= -\frac{M_x}{T_2} \\ \frac{dM_y}{dt} &= -\frac{M_y}{T_2} \end{aligned} \tag{2.1}$$

where M_o is the magnetization at thermal equilibrium, T_2 is the spin-spin relaxation, and T_1 is the spin-lattice relaxation time. Spin-lattice relaxation involves the exchange of energy between the spins and their surrounding (the lattice). This process produces a population re-distribution, back to the equilibrium distribution. Spin-spin relaxation involves interaction among spins without any change in the net spin energy (no change in relative population of the energy levels). Thus T_1 is the time constant for $\mathbf{M_z}$ to return to (1-e^{-1}) of M_o and T_2 is the time constant for the transverse magnetization components $\mathbf{M_x}$ and $\mathbf{M_y}$ to decay to 1/e of their initial values.

2.1 Spin Interactions in NMR

The general nuclear spin Hamiltonian could be written as two parts; a part which arises from external effects such as a strong Zeeman field (B_o) and the RF field (B_1) while the other part arises from internal effects that are related with the spin system itself. Therefore the full Hamiltonian of a nucleus in a strong magnetic field is given by [2]

$$\begin{aligned} \mathbf{H} &= \mathbf{H}_{ext.} + \mathbf{H}_{int.} \\ \mathbf{H}_{ext} &= (\mathbf{H}_Z + \mathbf{H}_{RF}) \\ \mathbf{H}_{int} &= (\mathbf{H}_{CS} + \mathbf{H}_J + \mathbf{H}_{SR} + \mathbf{H}_{DD} + \mathbf{H}_Q) \end{aligned} \tag{2.2}$$

$\mathbf{H}_Z$ is the Zeeman interaction, $\mathbf{H}_{RF}$ is the radiofrequency interaction, $\mathbf{H}_{CS}$ is the chemical shielding Hamiltonian, $\mathbf{H}_J$ is the indirect spin-spin coupling, and $\mathbf{H}_{SR}$

is the spin rotation Hamiltonian. $\mathbf{H}_{DD}$ and $\mathbf{H}_Q$ are the dipolar and quadrupolar interaction Hamiltonians, respectively. In many cases, the dominant interaction is due to the Zeeman Hamiltonian while the remaining interactions are considered as a perturbation. In the following section each of the above interactions will be discussed briefly while $\mathbf{H}_{DD}$ and $\mathbf{H}_Q$ will be explained in more detail.

2.1.1 Interaction with Static Magnetic Field-Zeeman Interaction

When a nucleus with non zero spin (I) and magnetic moment (μ) is placed in a strong magnetic field (B_o), according to quantum mechanics there will be (2I+1) non-degenerate energy levels corresponding to the (2I+1) values of m_I, where m_I is the magnetic quantum number. The Zeeman Hamiltonian for the interaction between each spin and the strong static magnetic field is given by

$$\mathbf{H} = -\gamma\hbar\overrightarrow{I}.\overrightarrow{B_o} \tag{2.3}$$

where γ is the gyromagnetic ratio, which has a constant value for a given nuclear isotope. Assuming the magnetic field is directed in the Z-direction then

$$\mathbf{H} = -\gamma\hbar I_z B_o \tag{2.4}$$

The allowed energies (E_m) for a given spin I (has m_I= I, I-1,...., -I) are

$$E_m = -\gamma\hbar B_o m_I \tag{2.5}$$

The energy difference between adjacent energy levels is given as $\gamma\hbar B_o$. The quantity γB_o divided by 2π is defined as the Larmor frequency (ν_o). This frequency is the precession rate at which a spin precesses around the Zeeman field B_o.

The population of spins is distributed according to the Boltzman distribution

as

$$\frac{N_{m_I\ -1}(upper)}{N_{m_I}(lower)} = e^{-\gamma\hbar B_o/kT} \tag{2.6}$$

where $N_{m_I\ -1}$ and N_{m_I} are the spin populations of the upper and lower energy levels, respectively; k is the Boltzman constant; $\hbar$ is Plank's constant divided by 2π and T is the absolute temperature. As seen from equation (2.6), the lower energy levels are occupied by a higher number of spins than the higher energy levels. For example, a sample containing protons placed in a magnetic field of 11.7 Tesla (500 MHz) , as used in this study, generates a population ratio (equation (2.6)) equal to 0.999478, at room temperature. The deviation of this population ratio from unity is very important in NMR since the magnetization and the signal only arise from this deviation. At equilibrium the magnetization is along the Z-axis.

2.1.2 Interaction with Radiofrequency Field

To perturb the equilibrium of the spin states in the Zeeman field (B_o) , an oscillatory magnetic field (B_1) is applied in an NMR experiment. The interaction between the RF pulse and the spin system is given as

$$\mathbf{H}_{RF} = -\gamma\hbar\overrightarrow{I}.\overrightarrow{B_1} \tag{2.7}$$

The B_1 field redistributes the spin populations to an extent that depends on the time that the RF field is on as well as its amplitude. For example, in the case known as a 90^o pulse, the RF field is on for a time that results in the energy levels being equally occupied, while in the case of a 180^o pulse the duration of the pulse is doubled compared to the 90^o pulse to produce the inversion of the spin populations. Vectorially the effect of the 90^o and 180^o pulses, is to flip the magnetization, initially in the Z-direction, into the XY-plane and the negative Z-direction, respectively.

Thus, the spin system is being influenced by two fields B_o and B_1. After B_1 is

switched off , the spins dephase and are redistributed again among the Zeeman levels and the magnetization returns to the equilibrium state. The response from the spins during this process is recorded in an NMR experiment.

2.1.3 Chemical Shielding Interaction

When a molecule is placed in a magnetic field, its electron cloud is affected so that a small current is set up resulting in an induced magnetic field $\overset{*}{\mathrm{B}} = \sigma \mathrm{B}_o$, where σ is a chemical shielding parameter. This induced field is small compared to the field B_o. The direction of $\overset{*}{\mathrm{B}}$ at a particular point in the molecule, may be quite different from that of B_o. Thus the total magnetic fields experienced by spins in the molecule will be different from B_o, and their resonance frequencies will be different from $\gamma \mathrm{B}_o$. The Hamiltonian for the chemical shift interaction is written as

$$\mathbf{H}_{\mathrm{CS}} = \text{-}\gamma\hbar\mathbf{I}.\underline{\underline{\sigma}}.\mathbf{B}_o \tag{2.8}$$

where $\underline{\underline{\sigma}}$ is a second rank chemical shielding tensor, describing how the shielding varies with molecular orientation. The tensor is diagonal in a principal axis system (PAS) with principal components σ_{11}, σ_{22} and σ_{33}. In a solution sample the isotropic chemical shift (σ_{iso}) is usually defined as

$$\sigma_{iso} = \frac{1}{3}(\sigma_{11} + \sigma_{22} + \sigma_{33}) \tag{2.9}$$

In the solid case, a structure in the NMR lineshape, that could be described using the anisotropic chemical shielding tensor $\underline{\underline{\sigma}}$ is typically obtained.

2.1.4 Spin Rotation Interaction

A rotational motion of the molecules (or part of the molecules) in a sample generates small magnetic fields that interact with the spins. This interaction is

called spin rotation interaction. The corresponding Hamiltonian is given as

$$\mathbf{H}_{\mathrm{SR}} = \mathbf{I}.\underline{\underline{C}}.\mathbf{J} \tag{2.10}$$

where $\mathbf{I}$ and $\mathbf{J}$ are spin angular and rotational angular momenta of the molecule, respectively. $\underline{\underline{C}}$ is the spin-rotation interaction tensor. This interaction is important in liquids and gases. In NMR of the solid state, because the spins are usually restricted in their motion, this interaction is not important.

2.1.5 Indirect Spin-Spin Interaction

The indirect spin-spin interaction (also named J-coupling) is the interaction between spins on a molecule mediated by the electronic clouds of the molecule. This Hamiltonian is given as

$$\mathbf{H}_J = \mathbf{I}.\underline{\underline{J}}.\mathbf{S} \tag{2.11}$$

where $\mathbf{I}$ and $\mathbf{S}$ are the nuclear spin angular momentum operators of spin I and S, respectively. $\underline{\underline{J}}$ is the indirect spin-spin coupling tensor. This second rank tensor is usually assumed to be axially symmetric, but in general it is a non symmetric tensor (like $\underline{\underline{\sigma}}$). In a liquid, due to rapid molecular tumbling, only the isotropic part of this tensor is observed.

2.1.6 Direct Dipole-Dipole Interaction

This dipolar interaction is the direct, through-space interaction between the point dipoles associated with the different spins. This interaction carries both information about the orientation of the internuclear vectors in the Zeeman field and separation of the interacting nuclear spins. The Hamiltonian of the dipolar interaction for a spin pair is given by [3]

$$\mathbf{H}_{DD} = -\gamma_{_1}\gamma_{_2}\hbar^2 \ \frac{\mu_o}{4\pi}\left\{\frac{\mathbf{I}_1.\mathbf{I}_2}{r^3} - 3\frac{(\mathbf{I}_1.\ \overrightarrow{r})\ \ (\mathbf{I}_2.\ \overrightarrow{r})}{r^5}\right\} \tag{2.12}$$

where the subscript 1 refers to one spin and 2 refers to the other spin. When the scalar products are expanded and the expression is put into polar coordinates, Equation (2.12) becomes

$$\mathbf{H}_{DD} = \frac{\mu_o \gamma_1 \gamma_2 \hbar^2}{4\pi r^3} [A + B + C + D + E + F] \tag{2.13}$$

where

$$\begin{aligned}
A &= -\mathbf{I}_{1z}\mathbf{I}_{2z}(3\cos^2\theta - 1) \\
B &= \frac{1}{4}[\mathbf{I}_{1+}\mathbf{I}_{2-} + \mathbf{I}_{1-}\mathbf{I}_{2+}](3\cos^2\theta - 1) \\
C &= -\frac{3}{2}[\mathbf{I}_{1z}\mathbf{I}_{2+} + \mathbf{I}_{1+}\mathbf{I}_{2z}]\sin\theta\cos\theta\exp(-i\phi) \\
D &= -\frac{3}{2}[\mathbf{I}_{1z}\mathbf{I}_{2-} + \mathbf{I}_{1-}\mathbf{I}_{2z}]\sin\theta\cos\theta\exp(i\phi) \\
E &= -\frac{3}{4}\mathbf{I}_{1+}\mathbf{I}_{2+}\ \sin^2\theta\exp(-2i\phi) \\
F &= -\frac{3}{4}\mathbf{I}_{1-}\mathbf{I}_{2-}\ \sin^2\theta\exp(2i\phi)
\end{aligned}$$

The common factor $(\mu_o \gamma_1 \gamma_2 \hbar^2/4\pi r^3)$ is referred to as the dipolar coupling constant (R), μ_o is the permeability constant in a vacuum $(= 4\pi.10^{-7}\,\mathrm{T\,m\,A^{-1}})$, r is the distance between the two dipoles, and the raising $(\mathbf{I}_+)$ and lowering $(\mathbf{I}_-)$ operators are defined as

$$\mathbf{I}_+ = \mathbf{I}_x + i\mathbf{I}_y \ \text{ and } \ \mathbf{I}_- = \mathbf{I}_x - i\mathbf{I}_y \tag{2.14}$$

The dipolar interaction acts along the internuclear vector, and is axially symmetric and traceless in the Principal Axis System (PAS) of the molecules. Therefore R is sufficient to describe the dipolar coupling completely. In liquids, due to rapid tumbling, there is no direct effect of the dipolar interaction on observed spectra, however, it provides a local field fluctuation resulting in relaxation of spins. In a solid, for a powder sample[1], a powder NMR line shape is expected.

[1] Powder sample will be described in section (2.2).

For heteronuclear spin pairs, normally only term A contributes to the observed spectrum, while, due to the flip-flop operator appearing in term B, both terms A and B contribute to the spectrum of homonuclear spin pairs. When dealing with NMR line shapes, one can see that the dipolar interaction is one of the factors that causes broadening of the line. In some experiments involving polarization transfer (e.g. Cross Polarization), this interaction plays the main role in obtaining NMR spectra.

2.1.7 Quadrupolar Interaction

Nuclei with spin I > 1/2 have a non-spherically symmetric charge distribution and a quadrupolar moment. The majority of the nuclei (more than 70% [4]) in the periodic table are quadrupolar nuclei. Deuterium has a nucleus with spin angular I= 1 and its magnetic moment is a factor of 6.5 smaller than that of hydrogen, for which it is often substituted [4]. The quadrupole coupling constant[2] (χ) of ^{2}H in ^2H_2O is between 208 and 259 kHz [7][8][9]. The value of 213 kHz [9] was used for ^{2}H of heavy water confined in MCM-41. This value is much smaller than the Larmor frequency of about 76 MHz (in a magnetic field of 11.7 Tesla used in this study for deuteron spectra). The ^{2}H - ^{2}H and ^{2}H - ^{1}H dipolar couplings are both negligible relative to the quadrupolar interaction strength and the chemical shift dispersion is about 1 kHz. Thus, in a ^{2}H NMR experiment, dipolar interaction with other nuclei and chemical shift dispersion are often neglected, and the deuteron may be treated as an isolated spin-1 nucleus. This is one advantage of using spin 1 in studies of dynamics by NMR. There are other advantages of ^{2}H over ^{1}H, that have prompted its use in many dynamics studies using NMR. First its large χ value permits the study of motions over a large range of time scales. Second, one can selectively deuterate a part of a molecule at a reasonable cost. The quadrupolar interaction is then treated as a first order

[2] A definition of χ will be given later in this section.

perturbation. The Hamiltonian of equation (2.2) then reduces to the form

$$\mathbf{H} = \mathbf{H}_Z + \mathbf{H}_Q \tag{2.15}$$

Consider a deuteron in a magnetic field B_o along the Z-axis. In the absence of any quadruple interaction, the Zeeman interaction splits the ground state nuclear energy level as shown in Figure (2-1). The Zeeman Hamiltonian is given by

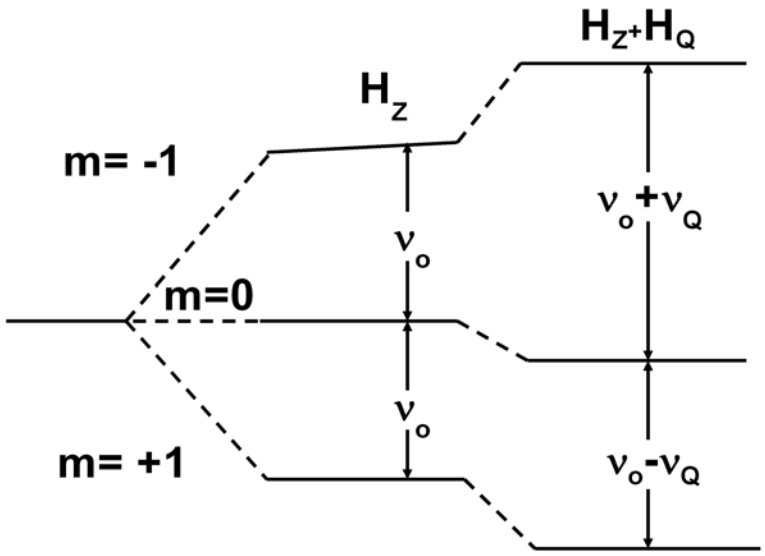

Figure 2-1: Splitting of the energy levels of a nucleus of spin 1 in a Zeeman field by Quadrupolar Hamiltonians.

equation (2.3) and the allowed values of I_z are m= -1, 0, +1, for I= 1. So the energy of the interaction is

$$E_m = -m\hbar w_o \tag{2.16}$$

In the O-^{2}H bond (in water molecule), the electron density has a highly anisotropic distribution which creates an Electric Field Gradient (EFG). For a nucleus with an electric quadruple moment, eQ, the interaction between the EFG and eQ results in a shift of these nuclear Zeeman levels [14]. The shifts in the

energy levels is shown in Figure (2-1).

In an electric potential $V(\overrightarrow{r})$, the energy of a charge density $\rho(\overrightarrow{r})$ is given as [5]

$$E = \int \rho(\overrightarrow{r}) V(\overrightarrow{r}) d^3\overrightarrow{r} \tag{2.17}$$

To evaluate the integral the volume of the nucleus needs to be considered. An expression for the energy can be found by the expansion of $V(\overrightarrow{r})$ using Taylor's series about the origin:

$$V(\overrightarrow{r}) = V(0) + \sum_{\alpha} x_\alpha \frac{\partial V}{\partial x_\alpha}|_{\overrightarrow{r}=0} + \frac{1}{2i}\sum_{\alpha,\beta} x_\alpha x_\beta \frac{\partial^2 V}{\partial x_\alpha \partial x_\beta}|_{\overrightarrow{r}=0} + ... \tag{2.18}$$

Thus for the energy E, we have

$$E = V(0)\int \rho(\overrightarrow{r}) d^3\overrightarrow{r} + \sum_{\alpha} V_\alpha \int x_\alpha \rho(\overrightarrow{r}) d^3\overrightarrow{r} + \frac{1}{2}\sum_{\alpha} V_{\alpha\beta} \int x_\alpha x_\beta \rho(\overrightarrow{r}) d^3\overrightarrow{r} + ... \tag{2.19}$$

where x_α ($\alpha = 1, 2, 3$) stands for the X, Y, and Z coordinates, respectively. The quantity

$$V_{\alpha\beta} = \frac{\partial^2 V}{\partial x_\alpha \partial x_\beta}|_{\overrightarrow{r}=0} \tag{2.20}$$

is the symmetric, traceless second order tensor, called EFG tensor. The first term, $E^{(0)}$, of equation (2.19) is the energy of a point charge in the electric potential $V(0)$ and the second term, $E^{(1)}$, is zero because all integrals which involve odd powers of x_α vanish for nuclear states with definite parity. The third term, $E^{(2)}$, is the electric quadrupole interaction and can be written as

$$E^{(2)} = \frac{1}{2}\sum_{\alpha,\beta} V_{\alpha\beta} Q^N_{\alpha\beta} \tag{2.21}$$

where the nuclear quadrupole moment is defined by

$$Q^N_{\alpha\beta} = \int (3x_\alpha x_\beta - \delta^2_{\alpha\beta}\, r^2)\rho dr \tag{2.22}$$

In the above equation the integral is over the nuclear volume. The tensor ,V , is symmetric with respect to an interchange of α and β, $V_{\alpha\beta} = V_{\beta\alpha}$.

This symmetric, second rank tensor is diagonalized by using the coordinate transformation through Euler angles (α, β, γ), which brings us from the laboratory coordinate system into the PAS of the EFG tensor [16]. With the assumption [15] that

$$|V_{yy}| \leq |V_{xx}| \leq |V_{zz}| \tag{2.23}$$

where the maximum value of the EFG component is defined as

$$eq = V_{zz} \tag{2.24}$$

the asymmetry parameter is

$$\eta = \frac{V_{xx} - V_{yy}}{V_{zz}} \tag{2.25}$$

This means that the values of η satisfy the following inequality

$$0 \leq \eta \leq 1 \tag{2.26}$$

H_Q is given by the scalar product of the electric field gradient tensor with the quadrupole moment tensor, and can be expressed as [2]

$$\begin{aligned} \mathbf{H}_Q &= \frac{eQ}{6I(2I-1)}\, \mathbf{I}.\underline{V}.\mathbf{I} \\ &= \frac{eQ}{6I(2I-1)} \sum_{\alpha,\beta} V_{\alpha\beta}\, [\frac{3}{2}(\mathbf{I}_\alpha \mathbf{I}_\beta + \mathbf{I}_\beta \mathbf{I}_\alpha) - \delta^2_{\alpha\beta}\mathbf{I}^2] \end{aligned} \tag{2.27}$$

This can be written in the principal axis system as [10]

$$\begin{aligned} \mathbf{H}_Q &= \frac{eQ}{6I(2I-1)} \left[V_{xx}(3\mathbf{I}_x^2 - \mathbf{I}^2) + V_{yy}(3\mathbf{I}_y^2 - \mathbf{I}^2) + V_{zz}(3\mathbf{I}_z^2 - \mathbf{I}^2)\right] \\ &= \frac{h\chi}{4I(2I-1)}[(3\mathbf{I}_z^2 - \mathbf{I}^2) + \frac{1}{2}\eta(\mathbf{I}_+^2 - \mathbf{I}_-^2)] \end{aligned} \tag{2.28}$$

where χ is the quadrupolar coupling constant which is defined as

$$\chi = \frac{e^2 qQ}{h} \tag{2.29}$$

If the quadrupolar interaction is smaller than the Zeeman interaction, we can use perturbation theory. The first order perturbation[3] quadrupolar correction to the energy level of state m is given as [29]

$$E_m = \frac{-h\chi}{4I(2I-1)}(I(I+1) - 3m^2)[\frac{1}{2}(3\cos^2\theta - 1) - \eta\ \cos 2\phi\ (\cos^2\theta - 1)] \tag{2.30}$$

where θ is the angle between eq_{zz} and B_o and ϕ is the angle between the projection of eq_{zz} on the XY-plane and the X-axis (laboratory frame).

In the case of I= 1(m= -1, 0, +1) and assuming $\eta = 0$ we have [10]

$$\begin{aligned} E_{-1} &= \frac{1}{8}h\chi(3\cos^2\theta - 1) \\ E_0 &= -\frac{2}{8}h\chi(3\cos^2\theta - 1) \\ E_{+1} &= \frac{1}{8}h\chi(3\cos^2\theta - 1) \end{aligned} \tag{2.31}$$

so that each spin produces two absorption lines as

$$\begin{aligned} \nu &= \nu_o \pm \nu_Q \\ &= \nu_o \pm \frac{3}{8}\chi(3\cos^2\theta - 1) \end{aligned} \tag{2.32}$$

where ν_o is the Larmor frequency of the nucleus inside the field B_o as described by the Hamiltonian given in equation (2.16). ν_Q is the frequency shift associated with the the quadrupolar interaction. In the case of a sample having different orientations of nuclear interaction vectors (distribution of angle θ) each orientation will produce two absorption lines positioned symmetrically with respect to the Larmor frequency. The final spectrum will be a superposition of these lines.

[3] The second order correction is much more complicated but mainly depends on χ^2 and $(1/\nu_o)$. It becomes significant with nuclei of very large χ (for instance,^{17}O).

A powder sample is one such case and will be discussed in the next section.

2.2 Polycrystalline (powder) Sample

In the case of a powder sample, each crystallite gives rise to two lines (as described in the preceding section). The separation (h) between these lines is

$$h = \pm\frac{3}{4}\chi(3\cos\theta^2 - 1) \tag{2.33}$$

In order to obtain an equation for the powder spectrum, we first re-write the above equation as [10]

$$\begin{aligned} h &= \epsilon\lambda\ (3u^2 - 1) \qquad (2.34)\\ \text{where } \epsilon &= \pm,\\ \lambda &= \frac{3}{4}\chi,\\ \text{and } u &= \cos\theta \end{aligned}$$

In a powder sample, crystallites are oriented randomly in all possible directions. Therefore different values of $u = \cos\theta$ are equally probable, and the superposition of the lines arising from individual crystals gives a continuous spectrum of a density defined by a function $f(h)$ given as [10]

$$f(h) \backsim |du/dh| \tag{2.35}$$

using equation (2.34) we obtain

$$f(h) \backsim \frac{1}{|u|} \backsim (\frac{\epsilon h}{\lambda} + 1)^{-\frac{1}{2}} \tag{2.36}$$

The transition from m= +1 to m= 0, which corresponds to ϵ= +1, contributes to $f(h)$, in the interval -$\lambda < h < 2\lambda$: $f_+(h) = (\frac{h}{\lambda} + 1)^{-\frac{1}{2}}$. Similarly the

transition from m= -1 to m= 0 corresponds to ϵ= -1 and contributes to $f(h)$ in the interval $-2\lambda < h < \lambda$: $f_{-}(h) = (\frac{-h}{\lambda} + 1)^{-\frac{1}{2}}$.

The final ^{2}H powder spectrum is defined by the following equation [10], [11]:

$$f(h) = \left\{ \begin{array}{ll} (\frac{-h}{\lambda} + 1)^{-\frac{1}{2}} & -2\lambda < h < -\lambda \\ (\frac{-h}{\lambda} + 1)^{-\frac{1}{2}} + (\frac{h}{\lambda} + 1)^{-\frac{1}{2}} & -\lambda < h < \lambda \\ (\frac{h}{\lambda} + 1)^{-\frac{1}{2}} & \lambda < h < 2\lambda \end{array} \right\} \quad (2.37)$$

The shape of the powder pattern, for different values of the asymmetry parameter, is shown in figure (2-2). It is shown that if the η= 0 the quadrupolar splitting $(\Delta\nu_Q) = \Delta\nu_{xx} = \Delta\nu_{yy}$. Different η values give the same $\Delta\nu_{zz}$ but results in $\Delta\nu_{xx} \neq \Delta\nu_{yy}$. The parameters $\Delta\nu$ are defined in the caption of the figure. In a real spectrum each of these lines is broadened by the interaction of the spins with the neighboring spins in the sample. Thus the spikes of the powder pattern will be broadened and smoothened. In order to reproduce the real powder spectrum, a convolution of equation (2.37) with a shape function, $Sh(\nu)$, is often used [6] and the final equation for the powder NMR line shape is given as:

$$F(\nu) = \int_{-\infty}^{+\infty} f(\bar{\nu} - \nu_o) Sh(\nu - \bar{\nu}) d\bar{\nu} \quad (2.38)$$

For the shape function a Gaussian line shape is usually used [10]

$$Sh(\nu - \bar{\nu}) = \frac{1}{\Delta\nu_G\sqrt{2\pi}} \exp[-\frac{(\nu - \bar{\nu})^2}{2(\Delta\nu_G)^2}] \quad (2.39)$$

where $\Delta\nu_G$ is the width of the Gaussian line at half of maximum intensity.

2.3 Effect of Motions on NMR Line Shape

The discussion above was based on the spins satisfying the rigid lattice condition, in which the frequency of the motion of the molecules is less than the

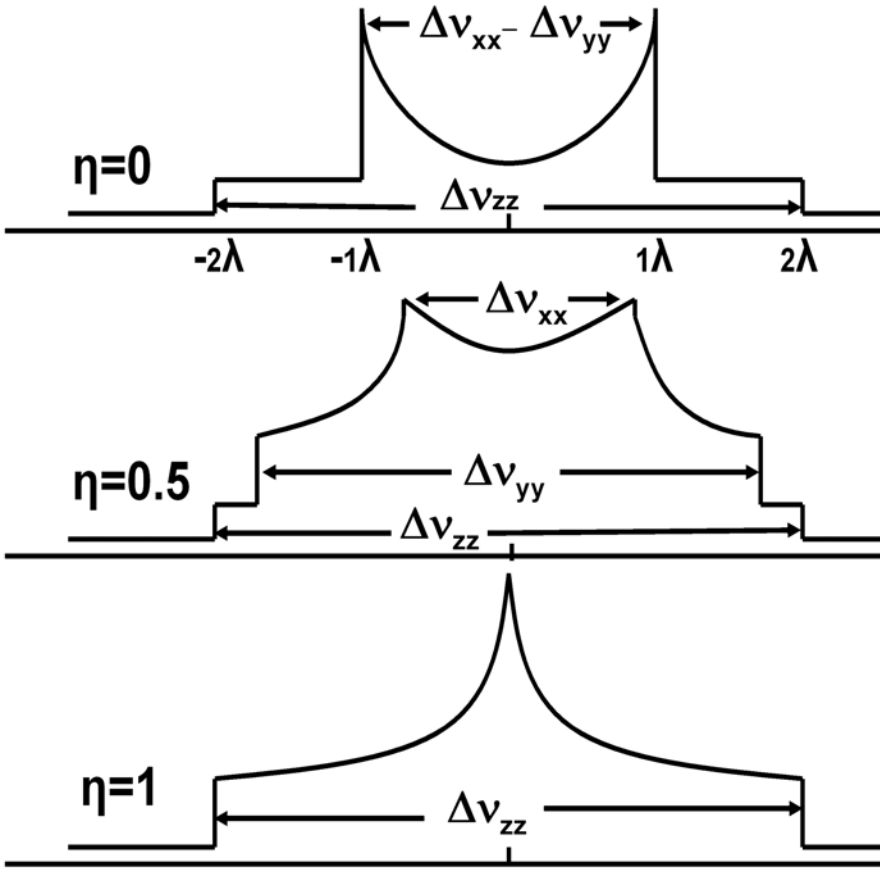

Figure 2-2: ^{2}H spectra for a powder sample with different values of asymmetry parameter. $\Delta\nu_{xx} = \frac{3}{4}\chi(1-\eta)$, $\Delta\nu_{yy} = \frac{3}{4}\chi(1+\eta)$ and $\Delta\nu_{zz} = \frac{3}{2}\chi$ [18]. In the real spectrum, these lines are broadened and smoothened by the dipolar interaction [10, chapter 7].

linewidth. From equations (2.33) and (2.37) it is seen that the frequency of absorption is angle dependent. This angle may change as the molecule undertakes a motion. Therefore, molecular motion can affect the NMR line shape. That is why many researchers focus on the study of the lineshape as a means of extracting information about the molecular dynamics of the system under study. There are three distinct cases when discussing the effect of motion (at rate k) on the lineshape [19]

1. Slow motion case: k$<$ 0.1 χ. The rigid lattice shape is not affected by the motion.

2. Intermediate motion case: 0.1 χ $<$k $<$ 100 χ. The line shape is strongly dependent on the rate of motion.

3. Fast exchange case: k$>$ 100 χ. The line shape has been affected by the motion but no longer depends on k.

The dipolar and quadrupolar Hamiltonians contain the angle dependent factor $(3\cos^2\theta - 1)$, and therefore the effect of molecular motion on line shape may be understood by determining how the motion affects θ. To elaborate on this, an example involving the effect of motion on the dipole-dipole interaction between two spins j and k (see Figure 2-3) is explored. This example applies equally well to the effect of the motion considered on the quadrupolar interaction by replacing the j-k interaction vector by the interaction vector of the quadrupolar spin. The two spins are separated by the internuclear distance r_{jk} and the internuclear vector $\overrightarrow{r_{jk}}$ makes an angle θ_{jk} with the magnetic field $\overrightarrow{\mathrm{B}_o}$. In this example the molecule is free to rotate about one axis (referred to as *a director* [13]). As the molecule rotates, the angle θ_{jk} is changing and varies with time. If we assume that the frequency of such motion is higher than the resonance linewidth, then the time average of the factor $(3\cos^2\theta_{jk} - 1)$ affects the line shape calculation. If we assume that the motion has three fold or higher symmetry, then this time average is given as [3][13]

$$\left\langle (3\cos^2\theta_{jk} - 1) \right\rangle_{avg} = (3\cos^2 \overset{*}{\theta} - 1)\frac{(3\cos^2\beta_{jk} - 1)}{2} \tag{2.40}$$

where the angles $\overset{*}{\theta}$ and β_{jk} are described in the figure. For instance, if the axis

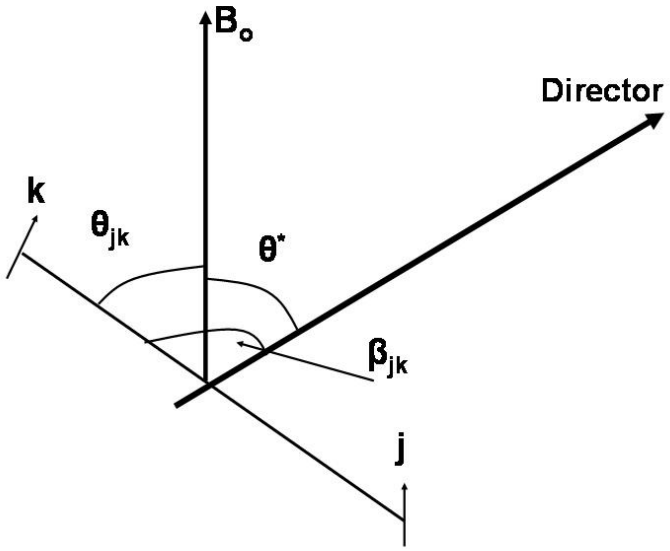

Figure 2-3: Angles involved when two spins j and k fixed in a molecule, are rotating around a given axis (director). During the rotation θ_{jk} is changing, which in turn affects the frequency of absorption and the NMR line shape.

of rotation were parallel to the internuclear axis ($\overrightarrow{r_{jk}}$) then the angle $\beta = 0$ and the motion would have no effect on the term $(3\cos^2\theta - 1)$ and the line shape. If the angle $\beta = \pi/2$ then

$$\left\langle (3\cos^2\theta_{jk} - 1) \right\rangle_{avg} = -\frac{1}{2}(3\cos^2 \overset{*}{\theta} - 1) \tag{2.41}$$

and the separation h between lines, or the splitting between lines, for each crystallite is reduced to half of the rigid lattice value.

In the ^{2}H case, the β is the angle between the axis of rotation and the maximum component of the EFG, namely the angle between the rotation axis and eq which is defined earlier. For the deuteron powder pattern for a sample involving this relatively simple motion, the following expression is often used [3]

$$\Delta\nu_Q = \Delta\nu_Q(RL)\frac{(3\cos^2\beta - 1)}{2} \tag{2.42}$$

where $\Delta\nu_Q(RL)$ refers to the quadrupolar splitting for the ^{2}H NMR line shape in the absence of motion.

2.4 Water and Hydrogen Bond

Water is the most common liquid on our planet, and is vital to all life forms. Despite the simplicity of the chemical formula of the water molecule (two hydrogen atoms with one oxygen atom), the physical properties of water are amazing. When the water molecule forms, the oxygen becomes sp^3 hybridized. In this formation, the oxygen atom is approximately centered on its 1s orbital while the hydrogen nuclei will be enclosed by two of the four p orbitals as shown in Figure (2-4)

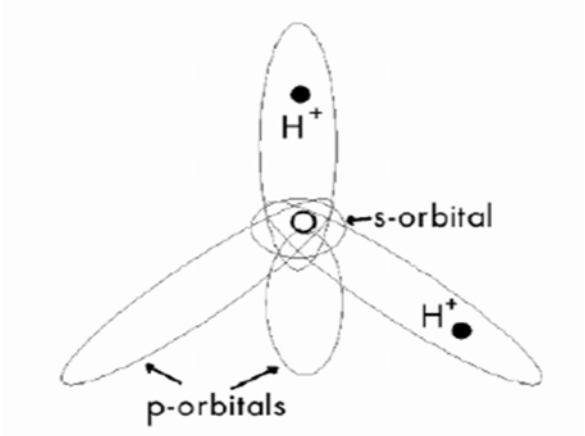

Figure 2-4: The arrangement of orbitals in a water molecule (from [20]).

Since the repulsion force between the two lobes containing the two hydrogen nuclei is smaller than that between the other two lobes, the angle of H–O–H is 105^o (smaller than 109^o if the lobes were oriented towards the corners of an ideal tetrahedron). Molecules in bulk water are bind with each other through hydrogen bonds. Each molecule has 3.5 hydrogen bonds on average at room

temperature. Most of the unique properties of water are related to this bond. In the water molecule, the oxygen has two unshared electron pairs that do not contribute to the H–O bonds of the water molecule. These electrons can interact with a nearby hydrogen atom to form a hydrogen bond. In a simple model of the water molecule in the bulk phase, molecules are located at the corners of an imaginary tetrahedron that minimize the potential energy of the group. However, the molecules still undergo rapid thermal motions on a time scale of 10^{-12} s. Thus, hydrogen bonds are being broken and reformed on this time scale.

The hydrogen bond is a weak bond and considered to be a combination of an ionic (90%) and a covalent bond (10%) [21]. It involves bonding between a partial positive charge (hydrogen) and a partial negative charge (oxygen, nitrogen, fluorine). In the case of water, it forms between a hydrogen atom of a water molecule and an oxygen atom of another water molecule. The strength of the H-bond depends on its length and angle. Generally, this bond is not stable if it is longer than 3.1 $\mathring{A}$ or the bond angle is less than 146^o [22]. The length of a hydrogen bond is a function of temperature and pressure. At room temperature the average length of this bond in water is about 1.9 $\mathring{A}$. Values ranging from 3 to 8 kcal/mole are reported for the strength of the hydrogen bond in H_2O [23] but typically a value of 4.2 kcal/mole is accepted among researchers. Table (2.1) shows some other parameters for H_2O and D_2O.

Parameters	**H_2O**	**D_2O**
Bond Energy O–H/O–^{2}H (kcal/mole)	111.3	113.2
Maximum Density (kg m^{-3})	999.9	1105.3
NMR chemical shift (ppm)	4.82	4.76

Table 2.1: Physical parameters for H_2O and D_2O [24].

2.5 Cross Polarization Experiment

In the Cross Polarization (CP) experiment the sensitivity of a dilute nuclear spin X (such as ^{13}C or ^{29}Si) is enhanced by increasing this spin's population dif-

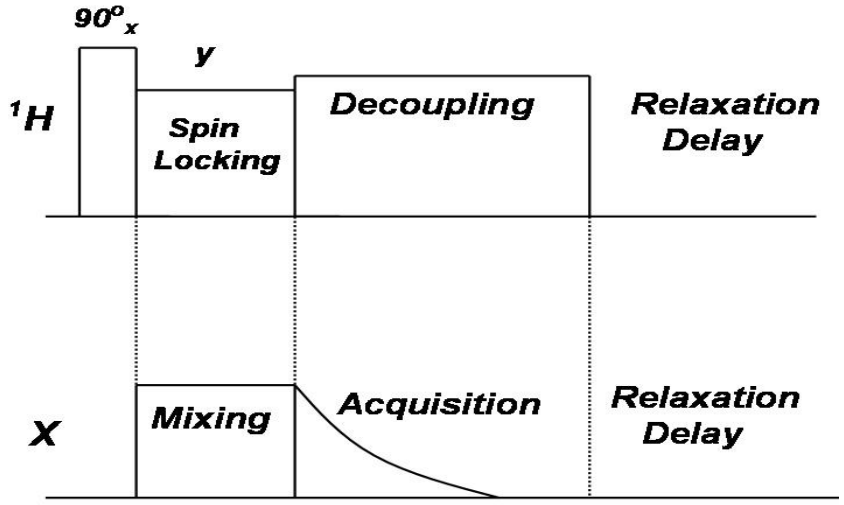

Figure 2-5: Pulse sequence for the Cross Polarization NMR experiment between ^{1}H and X (such as ^{29}Si) nuclei.

ference between up and down spin states through dipolar coupling with abundant spins (such as ^{1}H) in a double resonance experiment. An important aspect of a CP experiment is that the repetition time for the pulse sequence is governed by the T_1 of the abundant spins (^{1}H) rather than that of the dilute spins [25]. It is well known that T_1 becomes longer for smaller gyromagnetic ratio nuclei (for instance, ^{13}C or ^{29}Si). Thus considerable time can be saved in CP experiments compared with the case of studying dilute nuclei[4] directly using conventional pulse sequences.

The following is a brief description of the CP experiment detailing some of its features. In this description a *doubly rotating frame* is used: the ^{1}H and X spins are considered in frames in which all magnetic fields due to their respective RF pulses appear static. The starting point for any CP experiment is to rotate the proton magnetization by 90^o, to the y-axis, using an RF pulse along the x-axis (the standard CP pulse sequence is shown in Figure 2-5). The ^{1}H magnetization,

[4]For example, in ^{1}H- ^{29}Si CP, one only needs to repeat the pulse sequences every 5-8 seconds, while a repetition time of 60 minutes is needed if conventional techniques were used for ^{29}Si.

in the rotating frame, is then *spin-locked* along the y-axis by a pulse along the y-axis for a period of time called the *contact time* (or *mixing time*). Magnetization is transferred from the ^{1}H to the X nuclei during the mixing time. The extent of magnetization transfer is based on the choice of the spin-locking fields (B_1) for both ^{1}H and X nuclei. The magnitude of the two fields are chosen so that the Hartmann-Hahn condition [28] is satisfied

$$(\gamma B_1)_{protons} = (\gamma B_1)_{Xnuclei} \tag{2.43}$$

The dipole-dipole Hamiltonian $\mathbf{H}_{DD}$ as described in section (2.1.6) contains terms A to F, but for the CP experiment (heteronuclear case) only term A is important. This term includes operators $\mathbf{I}_{1z}\mathbf{I}_{2z}$, which are not affected by transformation into the rotating frame. Thus, this dipole-dipole coupling operator cannot affect the net energy of the spin system. Therefore the sum of the magnetization is also conserved. After the 90^o pulse, B_{1X} and B_{1H} are the only applied fields acting on the spin system in the rotating frame.

When the Hartmann-Hahn condition (equation 2.43) is met, the energy gaps between ^{1}H and X nuclei in their rotating frame spin states are equal and the dipole-dipole coupling operator can effectively distribute the magnetizations between the two different spin systems. Since the ^{1}H magnetization, in its rotating frame, is much larger than that of X spins and every transition of an ^{1}H spin is accompanied by a transition in the opposite direction of an X spin, this process will results in an increase in the magnetization of X nuclei by a factor proportional to $(\gamma_{proton}/\gamma_{Xspin})$. The magnetization transfer takes place during the *contact time*. In the case of the $^1\mathrm{H} - {}^{29}\mathrm{Si}$ CP experiment an enhancement by a factor of about 5 is obtained. In addition, considerable time will be saved because the pulse sequence repetition time depends on T_1 of the ^{1}H spins rather than T_1 of the ^{29}Si spins.

Spin temperature phenomena [26] can be used to interpret the magnetization

transfer between ^{1}H and X in a CP experiment in a very simple way using thermodynamics [27]. In the following it is assumed that the contribution to the heat capacities from the dipolar coupling between the spins can be neglected, and that negligible relaxation occurs during the CP process. The proton magnetization produced by the B_o field in the laboratory frame is, according to Curie's law, given as [11]

$$M_o(H) = [\frac{1}{4}\frac{\gamma_H^2 \hbar^2 N_H}{k}]\frac{B_o}{T_L} = \frac{C_H B_o}{T_L} \tag{2.44}$$

where T_L is the lattice temperature. By applying a 90^o pulse to the ^{1}H magnetization along the x-axis, the proton magnetization will rotate to the y-axis of the rotating frame. If the magnetization is then immediately spin-locked by B_{1H}, along the y-axis, the following equation will be satisfied

$$\begin{aligned} \frac{C_H B_o}{T_L} &= \frac{C_H B_{1H}}{T_s(H)} \\ T_s(H) &= \frac{B_{1H}}{B_o} T_L \end{aligned} \tag{2.45}$$

Therefore the proton spins are at a very low temperature ($T_s(H) \simeq 0.3$ K for $T_L \simeq 300$ K and $B_{1H}/B_o = 1000$) and their total energy is equal to $-C_H B_{1H}^2/T_s(H)$. However, at the same time the X magnetization is equal to zero along the field B_{1X}. This corresponds to $T_s(X) = \infty$. If the Hartmann-Hahn condition (equation (2.43)) is met transfer of energy occurs between the spin systems so that they will come to a common temperature $\overset{*}{T}_s$, while conserving the total spin energy

$$\frac{C_H B_{1H}^2}{T_s(H)} = \frac{(C_H B_{1H}^2 + C_X B_{1X}^2)}{\overset{*}{T}_s} \tag{2.46}$$

Here $C_X << C_H$ so that $\overset{*}{T}_s \simeq T_s(H)$. This means that the temperature of the X-spins, which was infinite at the beginning of spin-locking, will be $T_s(X) = T_s(H) = \overset{*}{T}_s$. Thus, the magnetization for X nuclei, which would have been

$M(X) = C_X B_o/T_L$ with spin-locking by B_{1X}, but without thermal contact with ^{1}H spins, now becomes (using equations 2.45 and 2.43)

$$M(X) = C_X \frac{\gamma_{_H}}{\gamma_{_X}} \frac{B_o}{T_L} \tag{2.47}$$

Therefore, an enhancement by a factor of $(\gamma_{proton}/\gamma_{X spin})$ is achieved.

In a ^{1}H- ^{29}Si CP experiment the proton and silicon nuclei are coupled through dipolar interaction. Although rather weak dipolar coupling between the Si nuclei may broaden the silicon resonance slightly, the main broadening for this nucleus is due to anisotropic chemical shift interaction. The latter contains the term $(3\cos^2\theta - 1)$ which is normally diminished using an NMR technique, called Magic Angle Spinning (MAS). In this experiment, the sample is spun at a high speed (10 kHz, for example) about an axis that makes an angle φ with the field B_o. For φ= 54.74^o, called the magic angle, the term $(3\cos^2\theta - 1)$ goes to zero. MAS is widely used in solid state NMR and in certain cases can have a significant effect in reducing the quadrupolar splitting in the NMR spectra. In a part of this study a combination of this technique with CP has been used to study the ^{1}H-^{29}Si coupling. The method is called ^{1}H- ^{29}Si CPMAS.

2.6 Magnetization Exchange in NMR

In most solid state NMR experiments exchange implies motional exchange. The motion of a molecule makes the atoms exchange position with the neighboring atoms (e.g., in the case of the in plane rotation of benzene ring). In that case the exchange depends on the rate of the intra-molecular motion. When the sample under study contains spin systems or spin groups in different environments (motionally and/ or structurally), these may have different relaxation and spectral characteristics. There are cases where magnetization exchange takes place between these groups. When the exchange process involves the breaking of a chemical bond, it is called chemical exchange. This is the case when two protons from different water molecules exchange. If the exchange is governed by the

interaction between the two spins, it is called magnetic exchange. In addition, exchange can occur via the exchange of whole molecules between two (or more) sites in which spins have different relaxation/ spectral character. This is called physical exchange. Below we will describe the theoretical basis for two-site and multi-site magnetization exchange. Both exchange scenarios were used in this study.

2.6.1 Two-Site Magnetization Exchange

Consider a sample containing two spin groups a and b that are in different environments. If these two groups are exchanging with each other, the following two differential equations describe the time evolution of the two magnetizations [32]

$$\frac{\partial}{dt}\begin{pmatrix} M_a \\ M_b \end{pmatrix} = \begin{pmatrix} -R_a - k_{ab} & k_{ba} \\ k_{ab} & -R_b - k_{ba} \end{pmatrix}\begin{pmatrix} M_a \\ M_b \end{pmatrix},$$

where M_a and M_b are the magnetizations for the sites a and b, respectively. R is the relaxation rate (inverse of T_1 or T_2). k_{ab} is the exchange rate of magnetization from site a to site b, while k_{ba} is the exchange rate of magnetization from site b to site a. The exchange rates satisfy the detailed balance equation $M_{a0}k_{ab} = M_{b0}k_{ba}$. After solving the previous coupled equations we obtain the eigenvalues

$$\lambda\pm = \left[(R_{11} + R_{22}) \pm \sqrt{(R_{11} + R_{22})^2 + 4R_{12}R_{21}}\right]/2 \tag{2.48}$$

where

$$\begin{aligned} R_{11} &= -R_a - k_{ab}, \\ R_{12} &= k_{ba}, \\ R_{21} &= k_{ab}, \\ R_{22} &= -R_b - k_{ba}, \end{aligned}$$

and the eigenvectors, corresponding to these eigenvalues, are

$$\begin{pmatrix} 1 \\ (\lambda_+ - R_{11})/R_{12} \end{pmatrix} \text{ for } \lambda_+$$
$$\begin{pmatrix} (\lambda_- - R_{22})/R_{21} \\ 1 \end{pmatrix} \text{ for } \lambda_-$$

To obtain a final solution the following transformation matrices are introduced

$$U = \begin{pmatrix} 1 & b \\ a & 1 \end{pmatrix}$$
$$U^{-1} = \frac{1}{1-ab} \begin{pmatrix} 1 & -b \\ -a & 1 \end{pmatrix}$$

where $a = (\lambda_+ - R_{11})/R_{12}$ and $b = (\lambda_- - R_{22})/R_{21}$. Then

$$U \exp\left\{ \begin{pmatrix} \lambda_+ & 0 \\ 0 & \lambda_- \end{pmatrix} \right\} U^{-1} = \frac{1}{1-ab} \begin{pmatrix} e^{\lambda_+ t} & be^{\lambda_- t} \\ ae^{\lambda_+ t} & e^{\lambda_- t} \end{pmatrix} \begin{pmatrix} 1 & -b \\ -a & 1 \end{pmatrix}$$
$$= \frac{1}{1-ab} \begin{pmatrix} e^{\lambda_+ t} - abe^{\lambda_- t} & b(e^{\lambda_- t} - e^{\lambda_+ t}) \\ a(e^{\lambda_+ t} - e^{\lambda_- t}) & e^{\lambda_- t} - abe^{\lambda_+ t} \end{pmatrix}$$

and the final expression for time evolution of M_a and M_b is given as

$$\begin{pmatrix} M_a \\ M_b \end{pmatrix} = \frac{1}{1-ab} \begin{pmatrix} e^{\lambda_+ t} - abe^{\lambda_- t} & b(e^{\lambda_- t} - e^{\lambda_+ t}) \\ a(e^{\lambda_+ t} - e^{\lambda_- t}) & e^{\lambda_- t} - abe^{\lambda_+ t} \end{pmatrix} \begin{pmatrix} M_{a0} \\ M_{b0} \end{pmatrix} \tag{2.49}$$

The total magnetization M is the sum of M_a and M_b

$$M = \frac{1}{1-ab}\left\{\left[M_{a0}(1+a) - M_{b0}b(1+a)\right]e^{\lambda_+ t} + \left[M_{b0}(1+b) - M_{a0}a(1+b)\right]e^{\lambda_- t}\right\} \tag{2.50}$$

2.6.2 Multi-Site Magnetization Exchange

In this section we present a multi-site exchange approach for modelling magnetization exchange between spins exhibiting Lorentzian line shape and spins exhibiting a powder pattern line shape. A closely related problem has been discussed and analyzed previously [30], and the outline of the approach described below closely follows that given in this reference.

If the molecules containing the spins undergo isotropic motion at a rate much faster than the linewidth, and assuming that only dipole-dipole or quadrupolar interaction are involved, then the FID decays exponentially. The Fourier transform of this signal gives a Lorentzian line, $L(\nu)$, which is written as

$$L(\nu) = \frac{2\Delta\nu_L}{\pi\left[4\nu^2 + (\Delta\nu_L)^2\right]} \tag{2.51}$$

where ν is the frequency and $\Delta\nu_L$ is the standard half width at the half maximum of the Lorentzian line and is related to the spin-spin relaxation time T_2 as

$$T_2 = \frac{1}{\pi\Delta\nu_L} \tag{2.52}$$

In the case of the molecules containing the spins undergoing motion much slower than the linewidth, or anisotropic motion where at least one motional mode is slow compared to the linewidth, then the NMR lineshape typically contains structure and can not be described by an exponential or a Lorentzian line. In some cases, a powder pattern is produced. As we saw before, the absorption frequency is related to the orientation of the major component of EFG relative to B_o through the angle θ. Woessner [31] indicates that such a lineshape can be represented by a set of Lorentzian lines. The method starts from the idea that each line has a

discrete absorptive frequency (or specific angle θ). Thus, in a powder sample a series of θ values are introduced

$$\theta_i = \frac{\pi}{2n}(i - \frac{1}{2}) \ , \ (i = 1, 2, ...n) \tag{2.53}$$

where n is the number of θ_i values. Each individual θ_i is associated with a Lorentzian line and the total transverse magnetization can be written as

$$M^+(t) = \sum_{i=1}^{n} M_i^+(t, \theta_i) \tag{2.54}$$

At t= 0 the magnetization is M_0, which is governed by Currie's law such that

$$M_i^+(0, \theta_i) = M_0 P_i \quad \text{with} \quad \sum_{i=1}^{n} P_i = 1 \tag{2.55}$$

P_i is the magnetization population for each individual site. The evolution of the magnetization M_i is

$$\frac{\partial}{dt} M_i^+ = -iw_i M_i^+ - \frac{1}{T_2} M_i^+ \tag{2.56}$$

where the frequency shift w_i is the same as ν_Q, defined in equation (2.32), except here it is the shift for a particular angle θ_i. Since in the powder pattern case, the intensity of any point on the the pattern is orientation dependent, a weighting factor is introduced [31] such that

$$P_i = \frac{\sin\theta_i}{\sum_{i=1}^{n} \sin\theta_i} \tag{2.57}$$

Thus, the sum of the Lorentzian lines give the shape of the real powder pattern.

The above scenario is for a sample containing spins undergoing the same anisotropic motion. This is not the case in a sample investigated here in which some spins undergo relatively fast, isotropic motion while some undergo relatively slow or anisotropic motion. Thus the NMR lineshape is a mixture of a Lorentzian line and a powder pattern. If we introduce magnetization exchange between these

two sites, such exchange scenario can be represented by $n+1$ differential equations

$$\begin{aligned} \frac{\partial}{dt}M_i^+ &= -(iw_i + \frac{1}{T_2} + VM_{L0})M_i^+ + VM_{0i}M_L^+ \\ \frac{\partial}{dt}M_L^+ &= -(\frac{1}{T_{2L}} + VM_0)M_L^+ + V\sum_{i=1}^{n} M_{L0}M_i^+ \end{aligned} \tag{2.58}$$

The Lorentzian line is labelled by the subscript L while the powder line shape is represented by multi-Lorentzian lines each with subscript i. The individual site population p_i's have been replaced by the equilibrium values of magnetizations, the M_{0i}'s, which satisfy $\sum_i M_{0i} = M_0$. V is a magnetization exchange rate constant. In order to solve this set of equations, one needs to obtain the eigenvalues of the following matrix

$$\begin{pmatrix} iw_1 - \frac{1}{T_2} - VM_{L0} & 0 & \cdots & VP_1 \\ 0 & iw_2 - \frac{1}{T_2} - VM_{L0} & \cdots & VP_2 \\ \vdots & \vdots & \ddots & \vdots \\ VM_{L0} & VM_{L0} & \cdots & \frac{1}{T_{2L}} - VM_0 \end{pmatrix} \tag{2.59}$$

For each eigenvalue (λ_i) a unit vector $U_i^T = (U_{1i}, U_{2i}, ...U_{n+1,i})^T$ is defined, where T stands for the transpose. Thus, the magnetization vector is defined as

$$\begin{pmatrix} M_1 \\ M_2 \\ : \\ M_L \end{pmatrix} = U \begin{pmatrix} e^{\lambda_1} & 0 & \cdots & 0 \\ 0 & e^{\lambda_2} & \cdots & 0 \\ \vdots & \vdots & \ddots & 0 \\ 0 & 0 & 0 & e^{\lambda_{n+1}} \end{pmatrix} U^{-1} \begin{pmatrix} P_1 \\ P_2 \\ \vdots \\ M_{L0} \end{pmatrix} \tag{2.60}$$

The final NMR signal is given by the Fourier Transformation (FT) of the real part of the sum of all magnetization components

$$S(w) = \mathrm{Re}\, FT(M_1 + M_2 + ...M_L) \tag{2.61}$$

2.7 2D NMR Spectroscopy

In addition to the 1D NMR technique for studying magnetization exchange processes between different spin groups, two dimensional (2D) NMR spectroscopy is a proven, powerful approach. The time domain signal for 2D exchange NMR involves three different times (t_1, t_m and t_2), as shown in Figure (2-6). However, this signal is only Fourier transformed with respect to t_1 and t_2 to generate the frequency domain signal S(w_1, t_m, w_2) [33]. The signal is only recorded during the acquisition time t_2 while t_1 and t_m are systematically changed.

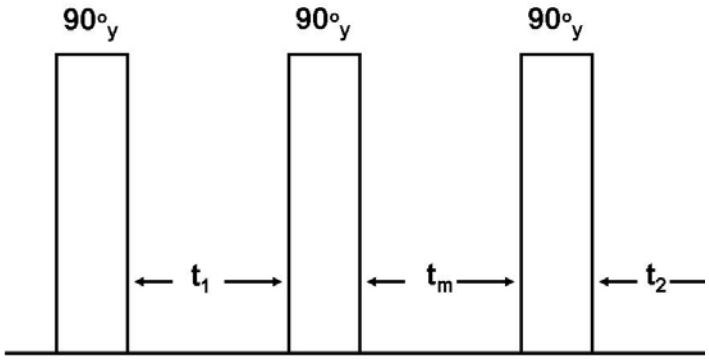

Figure 2-6: Basic scheme for 2D exchange spectroscopy. The spin groups evolve during t_1 and are detected only during t_2 while exchange is studied by varying the mixing time t_m. Different values of t_1 in conjuction with a set of t_2 values are needed in order to generate the 2D spectrum.

Consider the sample under study as consisting of two magnetization sites (a and b). The first 90^o pulse will turn the magnetization vector into the X-axis. During t_1 the magnetization is described using the following equations (ignoring

exchange and spin-lattice) [32]

$$\begin{aligned} M_a(t_1) &= M_{a0}[(cos(\Omega_a t_1) + i\sin(\Omega_a t_1)]\exp(-\frac{t_1}{T_{2a}}) \\ M_b(t_1) &= M_{b0}[(cos(\Omega_b t_1) + i\sin(\Omega_b t_1)]\exp(-\frac{t_1}{T_{2b}}) \end{aligned} \tag{2.62}$$

where M_{a0} and M_{b0} are the intrinsic equilibrium magnetizations at sites a and b, respectively. Ω_a and Ω_b are the angular frequencies at the respective sites due to chemical shifts. T_{2a} and T_{2b} are the spin-spin lattice relaxation times for sites a, and b respectively. The second pulse will generate two magnetization components along the Z-axis given as

$$\begin{aligned} M_{az}(t_1) &= M_{a0}cos(\Omega_a t_1)\exp(-\frac{t_1}{T_{2a}}) \\ M_{bz}(t_1) &= M_{b0}cos(\Omega_b t_1)\exp(-\frac{t_1}{T_{2b}}) \end{aligned} \tag{2.63}$$

It is worthwhile to mention that, during t_1 we still have two magnetization components on the Y-axis that can be ignored by using appropriate phase cycling or simply by considering longer mixing time during the experiment so that the Y-component decays through T_2 process. Therefore the two Z-components described in equation (2.63) can be considered as part of the initial conditions for the exchange. At this point, the problem is similar to the case of the classic two-site exchange discussed before.

During the mixing time (t_m) exchange takes place and the magnetization evolution can be described by

$$\begin{pmatrix} M_a(t_m) \\ M_b(t_m) \end{pmatrix} = \frac{1}{1-ab}\begin{pmatrix} e^{\lambda_+ t_m} - abe^{\lambda_- t_m} & b(e^{\lambda_- t_m} - e^{\lambda_+ t_m}) \\ a(e^{\lambda_+ t_m} - e^{\lambda_- t_m}) & e^{\lambda_- t_m} - abe^{\lambda_+ t_m} \end{pmatrix}\begin{pmatrix} M_{az}(t_1) \\ M_{bz}(t_1) \end{pmatrix} \tag{2.64}$$

where parameters a, b, λ_+, and λ_- have the same meaning as in the previous section. After the last 90^o pulse, during the acquisition time (t_2), the magnetiza-

tion is given by

$$\begin{pmatrix} M_a(t_2) \\ M_b(t_2) \end{pmatrix} = \frac{1}{1-ab} \begin{pmatrix} e^{(i\Omega_a t_2 - t_2/T_{2a})} & 0 \\ 0 & e^{(i\Omega_b t_2 - t_2/T_{2b})} \end{pmatrix} \begin{pmatrix} e^{\lambda_+ t_m} - abe^{\lambda_- t_m} & b(e^{\lambda_- t_m} - e^{\lambda_+ t_m}) \\ a(e^{\lambda_+ t_m} - e^{\lambda_- t_m}) & e^{\lambda_- t_m} - abe^{\lambda_+ t_m} \end{pmatrix} \begin{pmatrix} M_{az}(t_1) \\ M_{bz}(t_1) \end{pmatrix} \tag{2.65}$$

The total recorded magnetization is the sum of $M_a(t_2) + M_b(t_2)$ which represents the time domain signal as a function of the three times (t_1, t_m and t_2). The 2D spectrum is generated by performing double Fourier transformation with respect to t_1 and t_2. The final expression for the spectrum is given by [32]

$$\begin{aligned} S(w_1, t_m, w_2) = & \frac{4}{1-ab} x \\ & \{(e^{\lambda_+ t_m} - abe^{\lambda_- t_m}) \frac{M_{a0} T_{2a}^2}{[1 + (w_2 - \Omega_a)^2 T_{2a}^2][1 + (w_1 - \Omega_a)^2 T_{2a}^2]} \\ & + b(e^{\lambda_- t_m} - e^{\lambda_+ t_m}) \frac{M_{b0} T_{2a} T_{2b}}{[1 + (w_2 - \Omega_a)^2 T_{2a}^2][1 + (w_1 - \Omega_b)^2 T_{2b}^2]} \\ & + a(e^{\lambda_+ t_m} - e^{\lambda_- t_m}) \frac{M_{a0} T_{2a} T_{2b}}{[1 + (w_2 - \Omega_b)^2 T_{2a}^2][1 + (w_1 - \Omega_a)^2 T_{2b}^2]} \\ & + (e^{\lambda_- t_m} - abe^{\lambda_+ t_m}) \frac{M_{b0} T_{2a}^2}{[1 + (w_2 - \Omega_b)^2 T_{2b}^2][1 + (w_1 - \Omega_b)^2 T_{2b}^2]} \} \end{aligned}$$

In the presence of exchange between the two sites, two peaks will appear on the diagonal of the w_1, w_2 plane as well as two cross peaks that indicate the exchange between the sites. Only when exchange is negligible do both factors a and b approach zero. Then only two diagonal peaks are present, analogous to 1D spectra.

In the case of a sample containing spin 1 nuclei that have restricted mobility so as to yield a powder pattern, extra care needs to be taken when acquiring 2D exchange spectra. Using the classic 2D pulse sequence in this case will generate cross peaks that do not represent real exchange cross peaks. These artificial cross

peaks come about due to the dual frequency for each orientation in the case of spin 1. This problem can be solved by acquiring two 2D data sets using the two separate pulse sequences shown in Figure (2-7) [34].

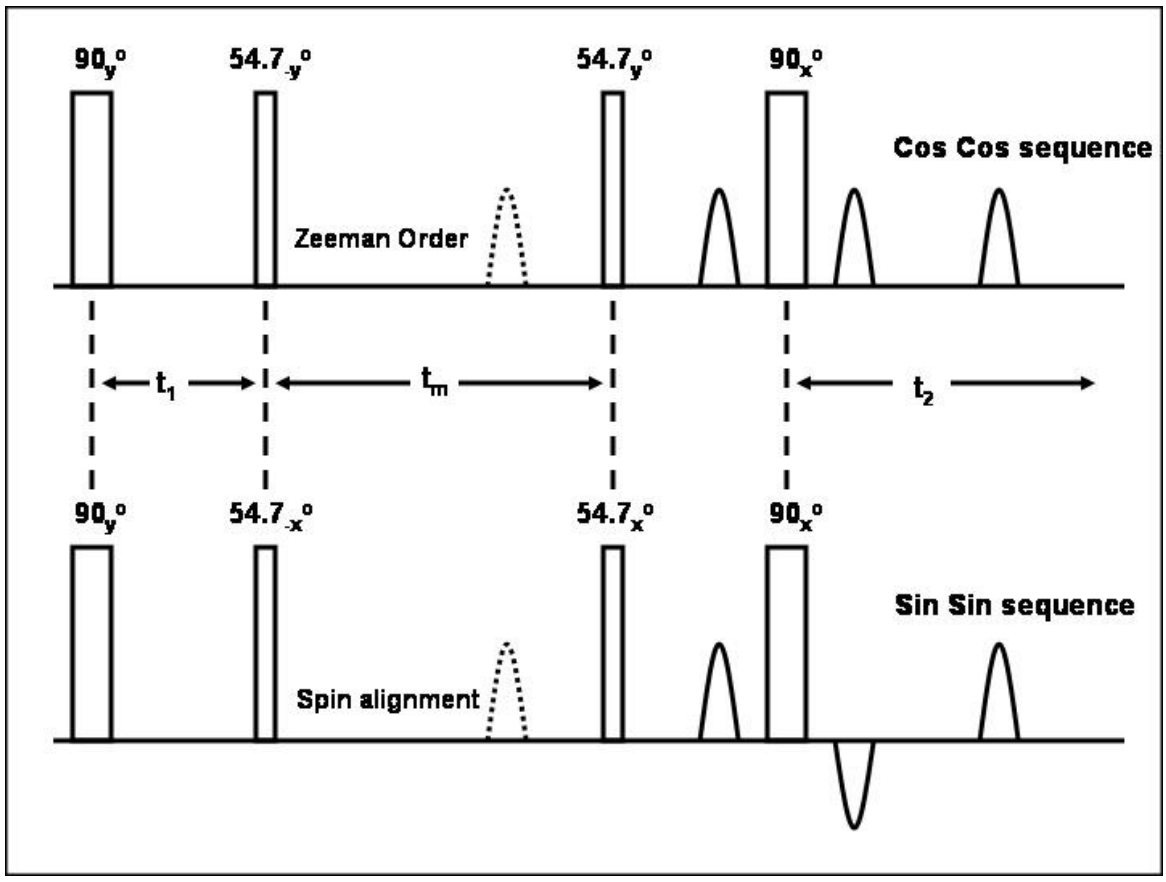

Figure 2-7: The pulse sequence used to measure the $<\mathrm{Cos}(w_1t_1)\mathrm{Cos}(w_2t_2)>$ and $<\mathrm{Sin}(w_1t_1)\mathrm{Sin}(w_2t_2)>$ correlation functions.

The time domain data for the top sequence is called Cos Cos part. The double Fourier transformation of this signal gives the classic 2D spectrum that includes real exchange cross peaks and the artificial cross peaks. The latter need to be filtered out by using the lower pulse sequence (Figure (2-7)) called the Sin Sin sequence. By subtracting this from the Cos Cos part yields the final 2D exchange spectrum that contains the diagonal powder pattern plus exchange ridges due to the exchange process. The details of the mathematical steps needed to follow

the magnetization using both sequences are explained in detail in references [34], [35].

If spin 1 nuclei under study undergo rapid isotropic motions, that average out the secular quadrupolar interactions, this dual pulse sequence is not necessary.

A more complicated case consists of the sample containing spin 1 nuclei undergoing restricted motion that produces a powder pattern and spin 1 nuclei undergoing isotropic motion that generate a Lorentzian spectrum. The study of exchange between these two groups using 2D exchange spectroscopy needs extra caution when it comes to the data interpretation.

Chapter 3

MCM-41

3.1 Introduction

Porous media play an important role in a wide range of disciplines. Geologists are interested in the flow of water through aquifers, and flow of oil-water mixture inside and out of reservoirs. Chemical engineers are interested in the effectiveness of porous catalyst particles and in multi-phase flow in a variety of porous media. Biomedical scientists are interested in the behavior of fluids (water, blood) in tissues, including flow of blood through organ tissues. Porous media are also important in the fields of soil science (transport of water and nutrients to roots), environmental science (soil remediation and wastewater treatment), food science and separation technologies (processes such as filtration, gas separation using membranes, and liquid chromatography), polymer science (e.g. the dehydration of contact lenses), and in the construction industry (e.g. the hydration of cement). As well, scientists in these disciplines are interested in the various ways of modeling porous media, and flow behavior within them, from a purely scientific point of view. In most of the applications mentioned, it is the transport of fluids within the porous media that is of interest and extensive literature exists on modeling such transport ([36] to [41]).

Zeolites are among the most widely used catalysts in industry. The reason for their success in catalysis is related to a number of specific features. They

have a high surface area and adsorption capacity, the adsorption properties of this material can be controlled, and the dimensions of their channels and cavities are in the range of the dimensions of many molecules, but not all. However, there was always a need to have available materials with more regular channels and with channels of larger diameters.

In 1992 the synthesis of a new family of silicate mesoporous molecular sieves, denoted as M41S, was reported [50][52]. MCM-41, which stands for Mobil Composition of Materials number 41, is one member of this family, has uniform hexagonal pores and is produced using rod-like micelles of cationic surfactant molecules as a template. The pore size of MCM-41 can be varied from 20 to 100 $\mathring{A}$ depending on the template used in the synthesis process. According to the definition of International Union of Pure and Applied Chemistry (IUPAC), mesoporous materials are those that have pore diameters between 20 and 500 $\mathring{A}$. Therefore MCM-41 is considered to be within the mesoporous category [78]. A full review of this material can be found in [42].

Upon its discovery, an explosion of scientific and commercial development using MCM-41 followed. New investigations on different aspects of this material, including synthesis, adsorption phenomena, catalytic properties were reported. Since MCM-41 has very regular pore channels, it should also be an ideal candidate as a model for studying water dynamics in a confined geometry.

3.2 Silanol Groups in MCM-41

It is known that MCM-41 is a silicate material. Therefore, for the study of water within this material, it is important to have available basic information about interaction between water and silica. The term silica is used to refer to the silicon dioxide in its various forms, including crystalline, amorphous, hydrated, and hydroxylated forms. Silica is soluble in water to a certain degree. The process can be represented by the following reaction [62]

$$Si\,O_2 + 2H_2O \implies Si\,(OH)_4$$

The surface groups of MCM-41 are silanol groups (SiOH) formed during the synthesis of the material. When water is introduced to the surface of MCM-41, it will attach to the hydration sites, SiOH, through hydrogen bonding. In the initial stages of adsorption, water molecules bind to the silanol groups through hydrogen bonds. Later, hydrogen bonded clusters of water molecule may begin to form as water molecules bond to the previously adsorbed water. This adsorption process can be represented as [63]

$Si_{surface}\,OH + H_2O \implies Si_{surface}\,OH{:}\,OH_2$ about 6.0 kcal/mole (released)

$Si_{surface}\,OH{:}\,OH_2 + H_2O \implies Si_{surface} : OH_2(OH_2)$ about 10.5 kcal/mole (released)

There are different silanol groups, denoted Q^{4-n}, in MCM-41 [69], where n refers to the number of hydroxyl groups attached to a silicon atom. Mainly there are three distinct Q groups in MCM-41. In all these groups, silicon has a tetrahedral arrangement with the four atoms it is bonded to. In a Q^4 group, silicon is attached to four oxygen atoms, which in turn are attached to other silicon atoms (no hydroxyl is involved). This group is mainly located within the pore wall of MCM-41. Q^2, $(SiO)_2Si(OH)_2$, referred to as a geminal group, is the silanol group that has only two hydroxyls attached to the silicon atom and contributes a very small fraction to the total number of Q groups in MCM-41 (around 3-5% [66][67]). From the view of the adsorption of water, the most important group is Q^3 . Here the silicon has only one hydroxyl group attached to it. This group is the dominant one in MCM-41 (around 40-60% [66][67], see Figure (3-1)). It is suggested in the literature [72] that hydroxyl groups are pointing toward the center of the pore. Q^3 could exist as a single, $(SiO)_3$Si-OH, or hydrogen bonded (H-bonded), $(SiO)_3$Si-OH-OH-Si$(SiO)_3$, group. In NMR, both give the same ^{29}Si chemical shift, while Infra Red (IR) measurements show

different absorption bands for the two types [71][79].

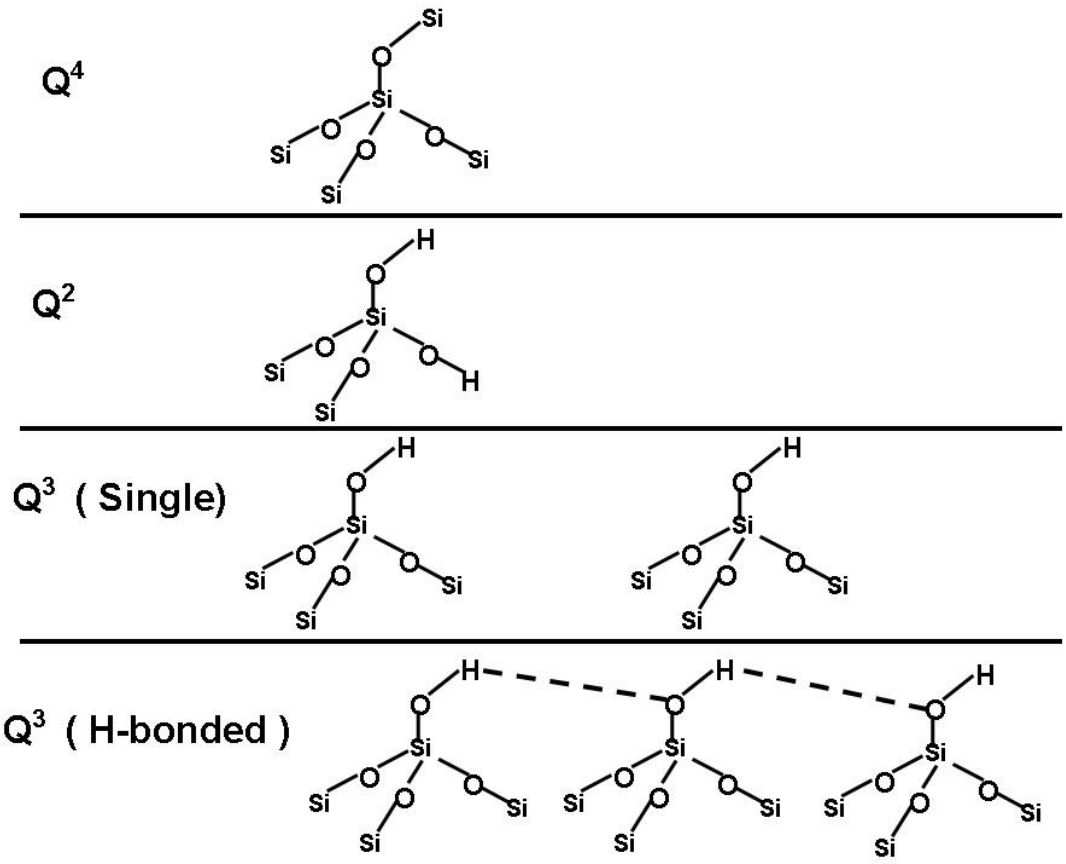

Figure 3-1: Different silanol groups in MCM-41.

The density of silanol groups on the pore surface of typical MCM-41 depends on the template removal method and varies between 2.5-5 nm^{-2} [72]. Most of the applications of this porous material include water as a major component and the adsorption of water depends strongly on the number of these silanol groups and their types. At the same time it is of interest to modify the surface groups (e.g., changing the number of single and H-bonded OH groups, replacing OH with other species) in various applications. Heating MCM-41 can remove OH groups, and different types of OH groups are removed at different temperatures. Therefore it is important to understand the influence of temperature on these groups.

3.2.1 Effect of Thermal Energy on the Silanol Groups

Many studies have shown that less heat is needed to affect the H-bonded silanol group than the single silanol group. Heating MCM-41 to 673 K (400 ^{o}C) only affects the H-bonded silanol groups [71][76][77]. The thermal energy converts these groups into single silanols plus siloxane groups [73][74]. At higher temperatures (but before collapsing the pores at around 1123 K [47]) the single silanol groups start to be removed [73][74]. In most cases the re-hydroxylation process is reversible to some extent [70]. It is expected that dehydroxylation of geminal groups (Q^2) is very difficult [75]. The process of silanol group conversion at different temperatures is illustrated in Figure (3-2).

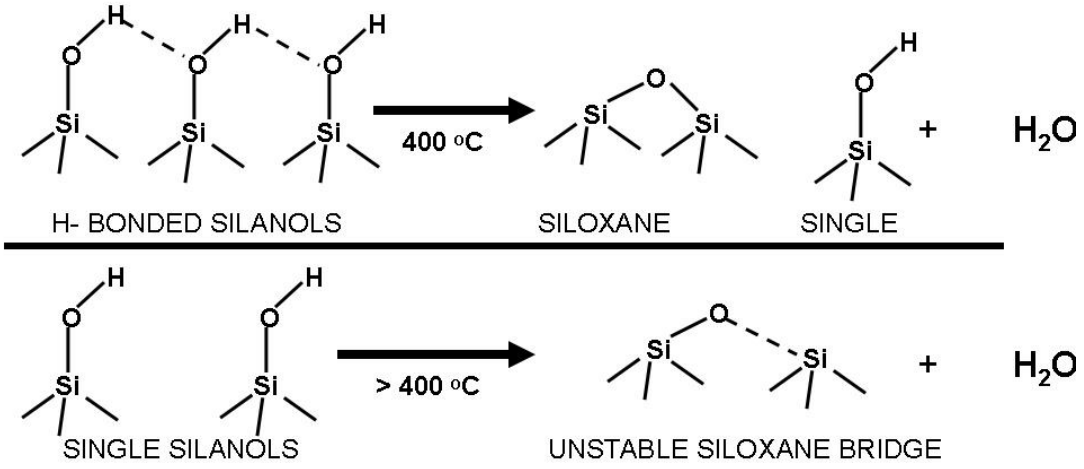

Figure 3-2: Effect of thermal energy on H-bonded and single silanol groups in MCM-41 (from [73] and [74]).

3.3 Literature Review

Over the last fifty years a significant number of studies has been performed to investigate the behavior of guest molecules (including water) in model confined geometries using different materials and different pore sizes. Different techniques, including IR, neutron scattering, dielectric spectroscopy and water sorption experiments have been used. NMR is considered one of the most important tools for addressing this issue. The main advantages of NMR methods are that they are noninvasive and nondestructive. They can be used to investigate both static and dynamic aspects of systems. In addition, NMR measurements may be made selectively on a particular component of a multi-phase mixture, for instance by using chemical shift selectivity or relaxation contrast techniques. In such studies, various materials have been used as models for confinement; e.g., vycor, Controlled Pore Glasses (CPG), clays, and glass beads. These materials are known to have interconnected pores with reasonable monodispersity and pore geometry definition. However, due to the random interconnection, it is difficult to resolve the relevant features of the host material. The outcome is that this complicates the interpretation of NMR results in terms of molecular dynamics of the confined guest molecules.

In the following, studies of surface effects on water using different techniques and materials, relevant to the present research, are summarized. In the later part we will focus on NMR studies of mesoporous MCM-41.

Woessner [80] investigated the range of the effect of the surface on the rotational motion of water molecule in clays using protons and deuterons as probes. This study, based on T_1 results, showed that the surface causes the nearby water molecules to rotate approximately five times more slowly than those in bulk water.

Overloop *et al.* [81] studied water behaviour in saturated silica gel samples using NMR. Two freezing points were recorded; one at 273 K for the water located outside the pores and the other at 264 K, for the water inside the pores. A value

of 7.5 kcal/mole was obtained for the activation energy for T_1 water protons inside the pores. It was concluded that the surface water extends to two or three adsorbed layers.

Two types of water adsorption sites exist on silica according to a study by Hanus *et al.* [82]; high energy sites (proton donors) and low energy sites (proton acceptors). It was concluded that deuterated water bonds preferentially to high energy sites and that proton bonding on silica is weaker than that for deuterons.

The detailed structure of the water/quartz interface was reported for the first time by Ostroverkhov *et al.* [84]. They used phase sensitive vibrational spectroscopy to distinguish between different water species. The presence of these different water species, or phases was attributed to the existence of different surface sites on this material.

Klier *et al.* [83] studied water adsorption isotherms for silica and silicate surfaces. The study showed that when water is introduced slowly to the dry surface, only half of the OH groups that exist on the surface bonded to the incoming water molecules before clusters of water molecules formed. The results were interpreted in terms of the surface having a partial hydrophobic property.

Proton rotating frame spin-lattice relaxation times ($T_1\rho$) of water in hydrated porous silica glass of different pore sizes was investigated by Holly *et al.* [85]. Pore surface water molecule correlation times were shown to be only slightly dependent on the pore dimensions (diameters in the range 74 to 491 $\mathring{A}$), and on the hydration levels. In the smallest pores (diameters equal to 74 $\mathring{A}$) studied all the water is affected by the surface and exhibits slow motion. A fast exchange model was used to interpret the data.

MCM-41 was modified by Sever *et al.* [79] for an IR study of its hydroxyl groups. Specifically, the surface was silylated with trimethylchlorosilane. The results indicate that 1.2 guest molecules are present for each nm^2 of MCM-41 and that the single and H-bonded silanol groups give different IR absorption peaks. The former gives a sharp band while the latter covers a broader IR band at

lower values of wave numbers. At higher temperature the broad band disappears indicating removal of H-bonded silanol, producing a siloxane and a single silanol.

Landmesser [70] studied the hydroxyl groups of the pore surface of MCM-41 using IR spectroscopy and NMR. In this study it was found that only about 30% of the silicon atoms have OH groups attached to them. Geminal groups contribute only 4% of the total silanol groups according to ^{29}Si MAS data. Heat treatment of MCM-41 powder affected the silanol groups. The H-bonded groups were affected at lower temperature and the single silanol groups were affected greatly at around 873 K (600 ^{o}C).

Chen [71] used IR technique to study the de-hydroxylation process in MCM-41. According to this study, H-bonded silanol groups could be completely removed from the material at around 673 K (400 ^{o}C) leaving the single silanol groups unaffected. The presence of C60, a spherical molecule consisting of 60 carbon atoms, changes the dehydroxylation process completely; at around 623 K (350 ^{o}C) (under pumping) both types of silanol groups were removed. It was concluded that introducing C60 changes the chemical bonding and builds new C-H and C-OH bonds. In normal MCM-41 both silanol groups were observed to exhibit two different IR bands.

Neutron scattering has been used to study water behaviour in MCM-41. For example, Takahara *et al.* [86] investigated the dynamics of water adsorbed on MCM-41 using quasi-elastic neutron scattering. Fully saturated samples with different pore diameters were studied for rotational and translational diffusion. The mobility of water in MCM-41 was found to be slower than in bulk water and its translational diffusion correlation times were longer than in bulk water.

Morineau *et al.* [87] studied the effect of pore size on the dynamics of water and on phase transition phenomena. For pores with diameters smaller than 30 Å, large deviations from the bulk structure were observed. These deviations are less noticeable for larger pore sizes because the contribution coming from the molecules at the water-pore surface interface is lower in this case.

Adsorption-desorption of water in MCM-41 was investigated with neutron

diffraction by Tun *et al.* [88]. Their results suggest that when MCM-41 powder is mixed with excess water, the water seeps into the entire length of the pore without voids or hollow spaces remaining within the pores. During drying, even at room temperature, most of the water left the pores but before the final stage of drying is reached the water re-distributed itself to form a layer covering the wall of the pores of this material. This confirmed the concept of monolayer formation at low hydration level in this material.

A correlation time of the order of nanoseconds has been determined for water confined in MCM-41 using high-resolution inelastic neutron scattering [49] [89]. The correlation time determined in [49] was longer, by an order of magnitude, from previous published results using similar techniques. Translational and rotational motion of water molecules were observed in saturated samples of MCM-41 and both motions were affected by the confinement. The effect of the confinement was much stronger on the translational motion than on the rotational motion.

Spanoudaki *et al.* [90] investigated the dynamics of water in nanoporous silica using dielectric spectroscopy. The study focused on the dynamics of water in MCM-41 with pore size of 32 Å for different hydration levels in the temperature range 150 to 250 K. The measurements distinguished the relaxation of the hydroxyl groups at the surface of silica from the orientational dynamics of hydration water. For the low hydration sample (about 0.29 monolayer) the activation energy for the water molecule reorientation obtained from the data was even smaller than the single hydrogen bond energy in ice (80 to 84% of that of ice). The interpretation was that a water molecule at this low hydration is hydrogen bonded to the silanol group of MCM-41 (hydrogen bond between the oxygen of water and OH of the surface) but that the water molecule forms no bonds with the other water molecules. This allows for more free rotation and consequently smaller activation energy. As the water layer builds up, a network of hydrogen-bonded water molecules is gradually formed and the activation energy reaches the value of that in ice when the hydration level exceeds about 1.6 monolayer.

MCM-41 was studied using water adsorption isotherm at room temperature

by Llewellyn *et al.* [91]. Their results indicated that the pores are filled before the completion of a compact monolayer. They concluded that MCM-41 has a relatively high hydrophobic character with a smaller hydrophilic contribution from surface OH sites.

An X-ray study performed by Edler *et al.* [92] on MCM-41 showed that the pore wall of MCM-41 has two distinct density regions not previously understood. These researcher postulated that denser walls in MCM-41 occur where two cylindrical surfactant micelles have touched and interpenetrated during synthesis.

Translational and rotational dynamics of two guest molecules, cyclohexane and cyclopentane, in MCM-41 has been investigated by Aksnes *et al.* [93] using NMR. The T_1 behavior was found remarkably similar for both molecules in MCM-41 while they show totally different T_1 behaviour in their bulk phases.

Benzene confined in MCM-41 of 30 $\mathring{A}$ pore size, shows a considerable slowing down of dynamics compared to the bulk state (Dosseh *et al.* [94]). However, no evidence of a sharp phase transition in the confined system was seen from temperature dependencies of T_1 and T_2 measurements.

Reactivity of the surface hydroxyl groups of MCM-41, towards silylation[1] with trimethyl chlorosilane, has been investigated by Wouters et. al. [95]. A silylation degree of 1.1 mmol per gram of MCM-41 was reported. ^1H NMR spectra of a dry sample (powder dried under vacuum at 388 K) showed a sharp peak at 2 ppm that was assigned to the single OH protons and a broader peak (3 to 6 ppm) that was assigned to the H-bonded OH group protons. The peak assigned to H-bonded OH groups started to disappear as the temperature of the sample was elevated up to 813 K. At that temperature only the peak attributed to single OH group protons at 2 ppm remained. ^{29}Si CPMAS data for the samples showed all Q-silanol groups except for the Q^1 group.

Landmesser *et al.* [70] studied the interior surface hydroxyl groups in MCM-41 focussing on the dehydroxylation process. Their results showed that as-

[1] This involves the replacement of an acidic hydrogen (H of Si–OH) on the compound with an alkylsilyl group, for example, -$SiMe_3$.

synthesized MCM-41 contains 53% Q^3 groups. Silicon NMR spectra showed that Q^4 gives a signal at -110 ppm, Q^3 at -101 ppm and Q^2 at -92 ppm. After calcination, all groups disappeared except for the Q^4 group. Dehydroxylation took place above 473 K (200 ^{o}C) and continued even up to 1273 K (1000 ^{o}C) (below 473 K (200 ^{o}C), only free water is removed). When the sample was re-hydrated again, it did not recover fully; the re-hydrated sample contains 27- 30% of SiOH (or Q^3 groups) present in the pre-calcination case.

Phase transitions of water, confined in MCM-41, have been studied in detail by Hanson *et al.* [96-98]. Water saturated samples of this material showed that water has two transition temperatures; one at around 223 K and the other over a wide range of temperature (centered at 207 K). They indicated the existence of multi-phase water in this material (solid ice, and the water in the rest of the pore (free water)). From their data, it was estimated that the surface water extends 5.4 ∓ 1 Å into the pore. No minimum in T_1 was observed over the range of temperatures studied (from 183 to 273 K).

Proton MAS was used by Grünberg *et al.* [99] to study the hydration process of MCM-41 as well as the filling and emptying process for the pores of this material. They reported that the filling and emptying of the pores with water was completely reversible and also proposed the axial filling of the pores. A material similar to MCM-41, SBA-15 was also studied using the same technique. They suggested that for the water filling-emptying process for the pores in the latter involved a radial progression of water. The study pointed out different possibilities of water bonding to the OH groups of MCM-41, each possibility giving a distinct chemical shift in the ^{1}H NMR spectrum.

A very detailed study of the surface of MCM-41 and its silanol groups was carried out by Zhao *et al.* [66]. Three different types of silanol groups were identified in this material; H-bonded, single and geminal. The estimated surface density of OH groups in MCM-41 was in the range 2.5 to 3 /nm^2. The H-bonded OH groups contribute 1.8- 2.3 per nm^2. About 70% of the total number of OH groups were indicated to be H-bonded silanol groups.

Hwang *et al.* [9] studied MCM-41 samples using deuterium NMR at three different levels of hydration. They suggested a three-site model for the water and labelled the sites slow, fast 1 and fast 2. From double quantum NMR and T_1 measurements they determined the exchange rate between the water in the fast 1 site and the surface water slow site to be of the order of 1000 s^{-1} and that between the two fast sites be of the order of 300 s^{-1}.

Proton and deuteron NMR spectra where obtained in hydrated (H_2O and D_2O) samples of MCM-41 by Pizzanelli *et al.* [100]. Sidebands of the ^2H MAS spectra were utilized to study the rotation of the single silanol groups, and the angle of rotation of the OD bond about the SiO bond was deduced to have values of 47^o and 63^o. They also assumed the presence of magnetization exchange between H-bonded and single silanol groups in this material.

Trebose *et al.* [101] studied the water mobility and characteristics of both types of silanol groups in MCM-41 using 1D and 2D NMR techniques. They deduced the exchange rate of magnetization between the two water sites in hydrated MCM-41 to be of the order of $(10\ ms)^{-1}$. The result showed weak hydrogen bonds between water and silanol groups.

Despite the many studies on MCM-41, as reviewed above, only limited information is available about its surface characteristics, hydration sites and pore-filling properties. In addition, detailed information about magnetization exchange between different water environments in MCM-41 is not available. Such information is necessary in order to obtain a realistic model for water dynamics in this material. This study is conducted to elucidate these aspects and to gain a better understanding of water dynamics within MCM-41.

Chapter 4

Experimental Methods

4.1 Synthesis of MCM-41

MCM-41 can be synthesized following a wide variety of preparation procedures. A schematic representation of the formation of MCM-41 is shown in Figure (4-1 A). Besides the necessary presence of a source of silica, these procedures all have in common the requirement of a *templating agent*. A template is a structure-directing agent, which is usually a relatively simple molecule or ion, around which a framework is built up. The most common templates are quaternary ammonium ions with short alkyl (C_nH_{2n+1}) chains, which are used for the syntheses of a large number of zeolites. For the synthesis of MCM-41 similar quaternary ammonium ions are frequently used. Here, the short alkyl chain, is replaced by a long chain. This slight modification has an enormous impact on the behavior of the template in aqueous solutions [42]. Due to the large hydrophobic alkyl chain the template ions will aggregate together in order to minimize energetically unfavorable interactions of the apolar alkyl chains with the very polar water solvent molecules. The resulting aggregates of ions are denoted *micelles*. These micelles have a hydrophobic core, containing the large alkyl chains.

The energetically most favorable form of micelle is spherical, because in this geometry the surface energy is minimized most efficiently. Moreover, this confor-

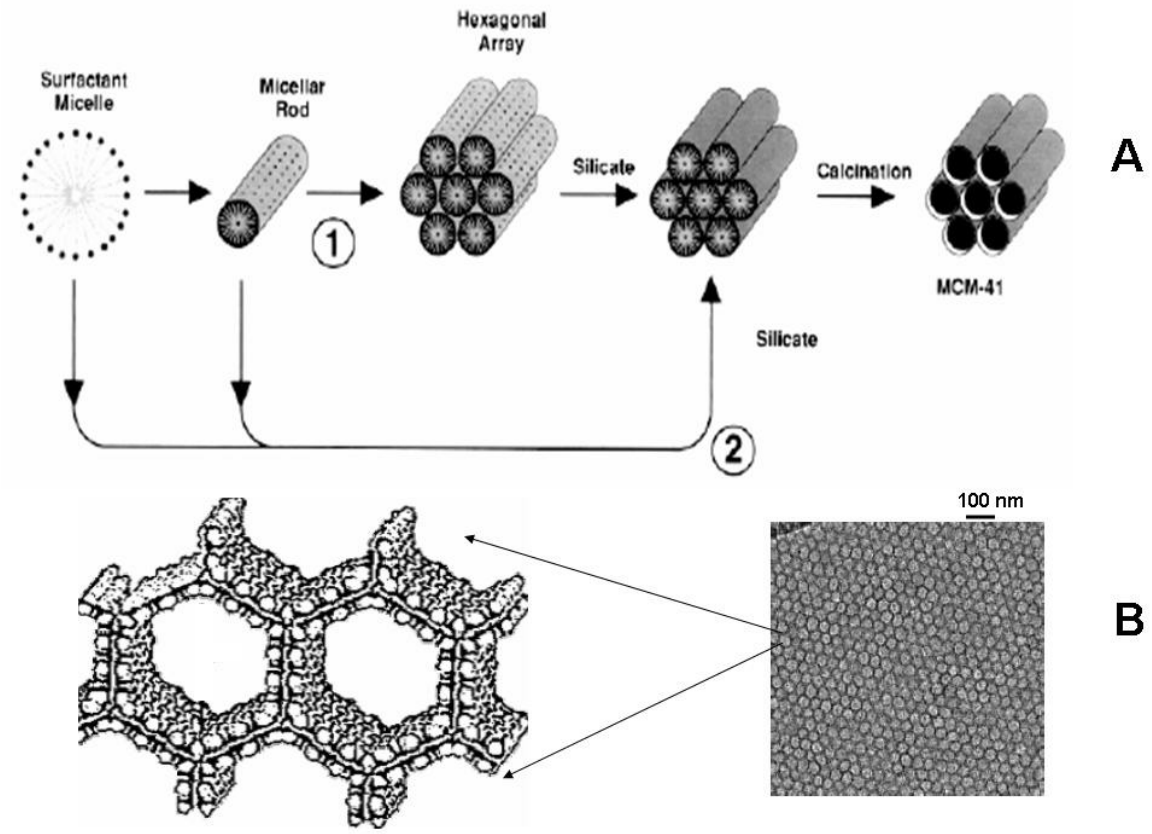

Figure 4-1: Schematic representation of the formation of MCM-41 (A) along with a high resolution transmission electron micrograph (B) that shows the hexagonal shape of the pores (from [48]).

mation allows the largest number of micelles to be formed out of a certain amount of template. Nevertheless, it is observed that at increasing amounts of template in water, a different micelle geometry evolves: the spherical micelles gradually transform into long tubes, often denoted as rod-like micelles. Increasing the template concentration even further results in aggregation of the rod-like micelles into hexagonal *liquid crystalline units*, resembling the MCM-41 structure [42]. If the template concentration is increased further this hexagonal liquid crystalline phase first transforms into a cubic liquid crystalline phase as in MCM-48, and at highest template concentration it transforms to a lamellar liquid crystalline phase MCM-50 [43]. The described templating mechanism is confirmed to be the case in preparing MCM-41 [44-46, 50]. Figure (4-1 B) shows a transmission electron micrograph of the pore geometry of MCM-41.

In addition to a structure-directing agent, and water as a solvent, two more ingredients are required for the synthesis of MCM-41; a source of silica and a mineralizing agent. The latter is used for the dissolution of the various silica sources which produce small silicon oxy-anions . In the presence of the rod-like template micelles, the silicate anions diffuse toward the surfaces of the micelles as a result of electrostatic attractions. Therefore, the concentration of silicate anions at the surface of the micelles rapidly increases, as does the electrostatic repulsion between the individual silicate ions. As a consequence, the ions condense into a monolayer on the micelle surface forming an amorphous silica template through the de-protonation of silanol groups. At this stage the silica 'coated' micelles can start to cluster together by condensation reactions between the silica layers of individual micelles, thus generating the MCM-41 framework. As a result of these processes the pore walls of MCM-41 are amorphous and only 2-3 monolayers thick [71]. Once MCM-41 has been formed its pores are filled with template material which needs to be removed. The template is removed by repeated washing of the material with de-ionized water and finally by *calcination*. During this process the template is decomposed into CO_2, NO_2 and steam.

Procedures for the synthesis of MCM-41 and its characterization have been

extensively discussed in the literature [50][51][53][54][55]. In this work the method described in [49] was used. Cetyltrimethyl ammonium bromide (CTABR, 99%) fumed silica powder (99.8%, particle size of 0.07 μm, metal free), and tetramethyl ammonium hydroxide pentahydrate (TMAOH, 97%) were obtained from Sigma-Aldrich. TMAOH and CTABR were added to 200 ml of distilled deionized water in a 400 ml beaker with continuous stirring (magnetic stirrer at 500 rpm) at 30 ^{o}C, until the solution became clear. The silica powder was then added to the solution and stirred for 3 hours until a uniform mixture of gel-like consistency was obtained. The molar composition used was as recommended in the literature (1 Si02: 0.19 TMAOH: 0.27 CTABR: 40 H_20) [68]. After letting the solution age for 24 hours at ambient temperature, it was transferred into a stainless steel Viton-lined autoclave, which was then heated in a furnace at 125 ^{o}C for 68 hours to allow the ingredients to react [49]. After cooling the autoclave the product was filtered, washed extensively (10 times) with deionized water, and dried in air at 50 ^{o}C overnight.

The polymeric template was then removed from the product by calcination at 650 ^{o}C (temperature was raised at a rate of 4 ^{o}C/min and once 650 ^{o}C was reached the sample left at that temperature for 8 hours). In the final stage of the MCM-41 synthesis the surface was hydroxylated by fully saturating it with H_2O (or D_2O) for one week. After drying the saturated powder, the desired NMR samples of different hydration levels (using H_2O or D_2O) were prepared. For the synthesized powder, the pore distribution was determined as described in the next section.

Experience has shown that the following additional points also need to be paid attention to during sample preparation:

- The sample material after the autoclave stage should be in a gel state. If it is a solid white composite means that the water has evaporated during the heating process. In this case the O-ring of the autoclave needs to be replaced by a new O-ring and the process needs to be repeated.

- The final calcination step should be performed with extra care. The furnace temperature needs to be increased gradually (rate of 4 ^{o}C/min. until 650 ^{o}C is reached). A black smoke produced at around 300 ^{o}C is an indication the template remained within some MCM-41 pores being burned. This will only last for a couple of minutes. After heating the sample at 650 ^{o}C for 8 hours the product should be a white, fine powder. If the calcination produced a yellowish outcome, its XRD would be different from that for highly ordered MCM-41.

- Different O-rings were tested with the MAS rotor with the goal of keeping the hydration level within the required limit. The best results were obtained when Viton O-rings along with Zirconia caps were used (Wilmad LabGlass company, catalogue number: WP-501-4181). Experiments proved that it is better to use a rotor and its cap from the same manufacturer. A combination of cap, O-ring, and rotor from Wilmad company gave the best result in our case.

4.2 Characterization of MCM-41

4.2.1 Pore Size Distribution

The mean pore size of the sample can be determined from the experimental data of nitrogen adsorption-desorption (that gives the volume (V) of N_2 gas versus the relative pressure (P_o/P)) utilizing the Kelvin equation [56][57]

$$R_k = \frac{4.14}{\ln(P_o/P)} \tag{4.1}$$

(P_o/P) is the relative pressure at which pore condensation of the adsorbate occurs. To find the pore size R_p one needs to calculate the correction factor t_{ads} which represent the thickness of the initially adsorbed layer on the pore surface and is given by [58]

$$t_{ads} = 3.5[\frac{5}{2.303Log(P_o/P)}]^{\frac{1}{3}} \tag{4.2}$$

so that

$$R_p = R_k + t_{ads} \tag{4.3}$$

Finally to determine the pore size distribution, an expression for dV/dR_p versus R_p is needed. We can get this expression from

$$\frac{dV}{dR_p} = \frac{dV}{d(\frac{P}{P_o})}\frac{d(\frac{P}{P_o})}{dR_k}\frac{dR_k}{dR_p} \tag{4.4}$$

where $dV/d(P/P_o)$ is determined, using the experimental nitrogen adsorption-desorption data for the sample, by numerical differentiation of the data with respect to P/P_o. The last two terms in the product, on the right hand side of equation (4.4), can be expressed in terms of P/P_o by combining all the above equations. The final expression is given by

$$\frac{dV}{dR_p} = 2.356\frac{dV}{d(\frac{P}{P_o})}[\ln^2(\frac{P_o}{P})]\frac{P}{P_o} \tag{4.5}$$

Thus, the pore size distribution of the mesoporous MCM-41 can be obtained by plotting dV/dR_p versus R_p.

Nitrogen adsorption/ desorption measurements were carried out on a Quantochrome Autosorb automated gas sorption system at 77 K with an outgas temperature of 473 K. Figure (4-2 A) shows a nitrogen sorption isotherm for MCM-41 synthesized in our laboratory. The data show three distinct regions; the initial linear increase of the curve is indicative of monolayer-multilayer adsorption on the pore walls, the steep increase represents capillary condensation within the pores, and the final part of the curve represents multilayer adsorption on the outer surface of the powder. The sharp step in the isotherm for the sample studied implies the uniformity in the pore size [102].

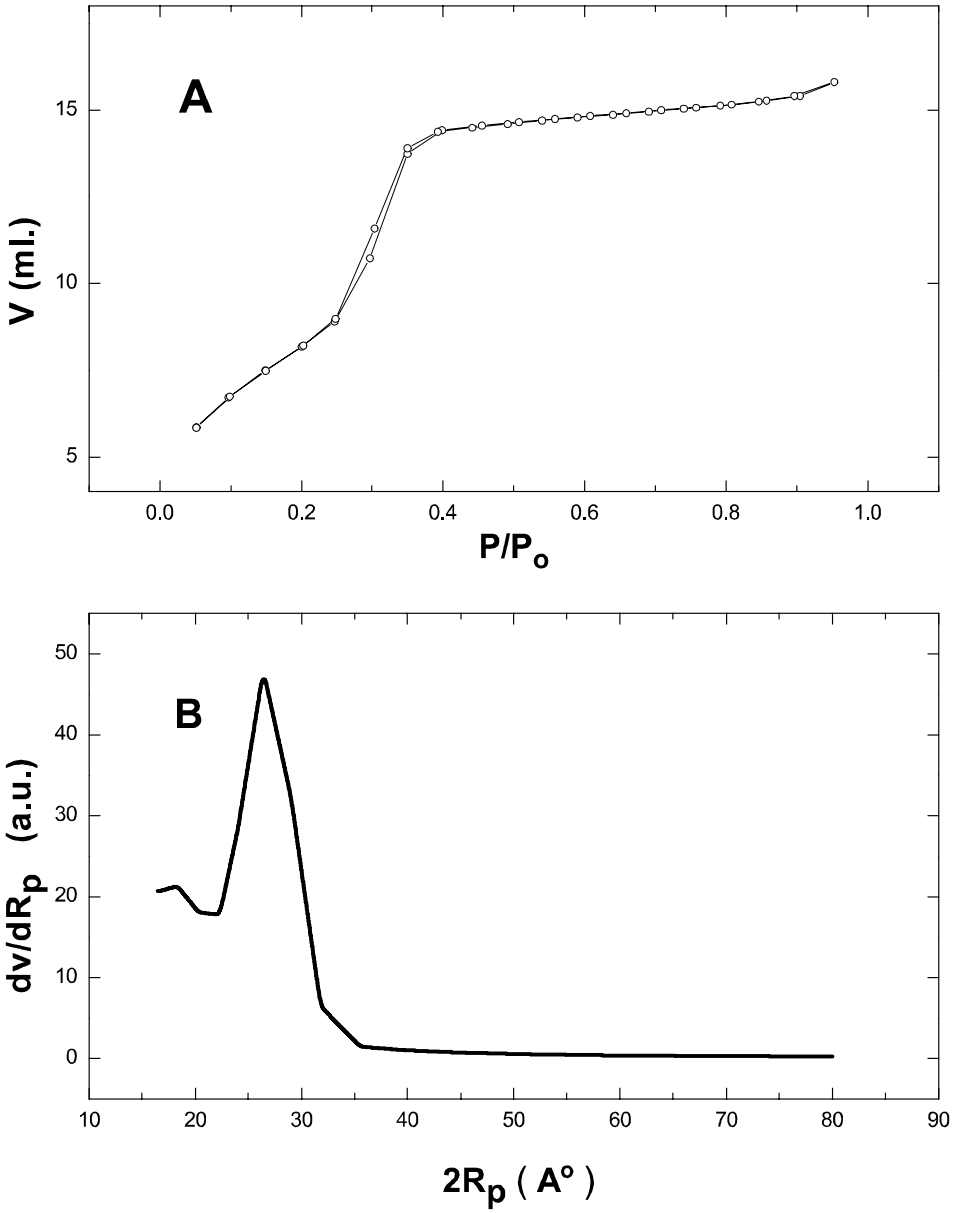

Figure 4-2: Nitrogen adsorption-desorption isotherm (A) and pore size distribution (B) (centered at around 27 $\mathring{A}$) for MCM-41 used in this study.

The pore size distribution of the MCM-41 used in this study, is shown in Figure (4-2 B) and was determined from the nitrogen adsorption-desorption data using equations (4.1) to (4.5). The figure shows a narrow distribution for the pore diameters (centered at 27 Å), consistent relatively high order in MCM-41 [49].

4.2.2 Specific Surface Area

In principle there are two kinds of adsorption of an adsorbate onto a surface depending on the strength of the interaction [61]; physical (physisorption) and chemical (chemisorption). In physical adsorption, the adsorbate bonds to the solid surface through a weak interaction (e.g., van der Waals interaction, hydrogen bond interaction). The energy of interaction is small and rarely exceeds values of 5 kcal/mole. This low interaction energy does not change the electronic state of the adsorbed molecule. In general, physical adsorption extends to several molecular layers from the solid surface [65].

To obtain the specific surface area of a porous material commonly nitrogen gas is physisorbed onto the material, and the adsorption behavior is analyzed using the BET adsorption model. The BET model (named after the researchers Brunauer, Emmett and Teller [59]) is based on the multilayer adsorption of the adsorbate on the surface. This model emerged from the Langmuir model [60], which assumes homogenous surface adsorption. In the BET model each adsorption site adsorbs only one molecule or atom. The model has been developed for physical adsorption and therefore allows multilayer formation. This model assumes that there are no interactions among adsorbed molecules or atoms. The BET isotherm is expressed by the following equation

$$\frac{P}{V(P_o - P)} = \frac{1}{V_m C} + \frac{C-1}{V_m C}\frac{P}{P_o} \tag{4.6}$$

In the above equation, V is the volume of the gas adsorbed, V_m is the volume of gas corresponding to a monolayer of the adsorbate, C is a constant, and P_o is

the saturating vapor pressure of the gas.

Equation (4.6) is used to determine the surface area of the material under study [56][64][65]. To this end one needs data for gas adsorption-desorption of that material. In this connection nitrogen adsorption-desorption is perhaps the most widely applied technique in the study of porous materials. Such data is of the form V(volume of the nitrogen adsorbed on the surface) versus P/P_o (relative pressure of the gas used). In the linear plot of $P/V(P_o - P)$ versus P/P_o the slope S is $C - 1/V_m C$ and the intercept I is $1/V_m C$. The volume of a monolayer $V_m = 1/(I + S)$. Therefore, the BET surface area will be given as $S_{BET} = V_m N A_{gas}/(MV)$, where N is Avogadro's number (6.0221367×10^{23} mole^{-1}), A_{gas} is the molecular cross-sectional area of the gas used (for N_2, A_{N_2}=(0.162 nm^2), and M is molecular weight of the gas. For the sample used in this study, the BET surface area is calculated to be equal to 1122 m^2/gm.

4.2.3 XRD Characterization

XRD measurements were carried out with $CuK\alpha$ radiation from a Siemens D5000 diffractometer operating at 40 kV and 30 mA using 0.020^o steps and a 2 s step time. Figure (4-3) shows XRD diffraction patterns of MCM-41 powder before and after calcination. By comparing the two patterns, one notices that the final calcination process results in an enhancement of the 100 peak intensity. This is indicative of improvement in the long-range ordering of the pores in MCM-41 [71] via removal of the template during the calcination stage. The sample before calcination shows an extra peak at $2\theta \sim 2.2^o$, which is likely attributable to the presence of different amounts of template material inside different pores. The XRD data shows well-resolved peaks typical of the hexagonal pattern in highly ordered MCM-41 [49].

The XRD spectrum of a sample left under ambient conditions for one year was the same as that shown in Figure (4-3 B), for a sample that was left under ambient condition only for two days after synthesis. This clearly demonstrates the stability of the material.

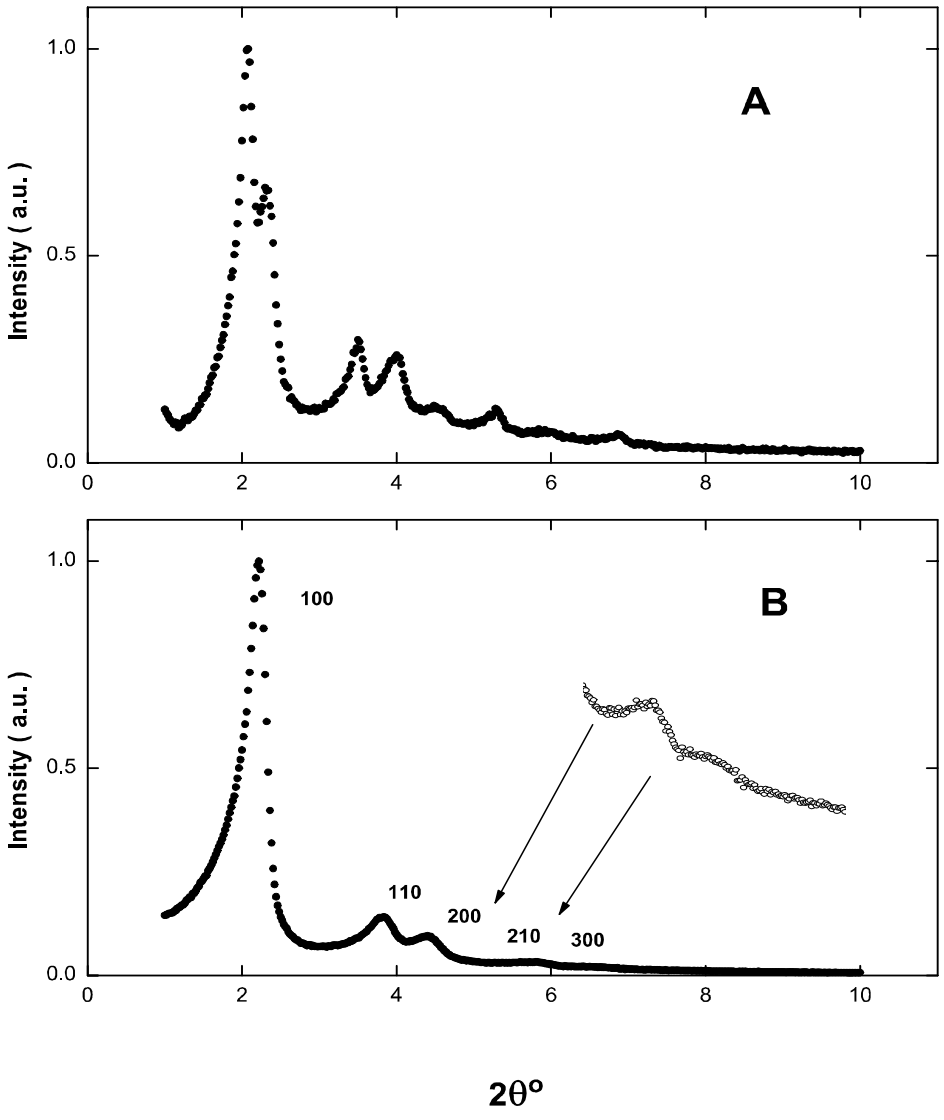

Figure 4-3: X-ray diffraction pattern for MCM-41, synthesized in our laboratory, before calcination (A) and after calcination (B). Five peaks can be seen in the latter case as an indication of the high order in the MCM-41 [49].

4.3 NMR Samples

The final process in the synthesis of MCM-41 was calcination at high temperature (650 ^{o}C). The next step is hydroxylation using H_2O or D_2O depending whether protonated or deuterated samples needed to be studied. Samples with the desired hydration level were prepared using the procedure described below.

The hydration level is expressed in terms of the number of monolayers of water molecules covering the MCM-41 surface. The hydration needed to cover the surface area of pores of 1 gram of MCM-41 by one layer of water molecules can be found by assuming one water molecule covers a square, d= 3 $\mathring{\text{A}}$ on a side. Here it is also assumed that the internal surface of the pores needs to be considered only, because the external area of the grains is negligible with respect to the pore surface area. Therefore, the mass of water needed for one monolayer coverage of a gram of MCM-41 is given as

$$h_{H_2O} = \frac{S}{d^2}\frac{M}{N_A} \tag{4.7}$$

where M is the gram molecular weight of water, N_A is Avogadro's number and S is the BET surface area for MCM-41. Thus, to hydrate one gram of MCM-41 to the one monolayer level of water requires 0.375 gm of H_2O (or 0.416 gm of D_2O).

Two different categories of NMR samples were prepared from the synthesized MCM-41 as described below.

First category: MCM-41 was hydroxylated by immersing the MCM-41 powder in D_2O and leaving it in a desiccator for about a week, at ambient temperature. Then excess water was removed by leaving the wet MCM-41 on filter paper in a glove box, with dry nitrogen atmosphere, over night. To finalize the drying process, for each NMR sample, an appropriate mass (about 30-35 mg) of the above powder was placed into the MAS rotor of 4 mm outer diameter, and dried at 105 ^{o}C, under vacuum (less than 10^{-3} torr), for 24 hours. For the dry sample, denoted as 0D, where 0 stands for zero water content, the rotor was

removed from the vacuum system, and moved to the glove box, filled with dry introgen gas, where it was immediately covered by the rotor cap. During the move from the vacuum system to the glove box the rotor containing the sample was kept under vacuum inside a glass vial that can be detached from the vacuum system which maintaining the vacuum inside it. A special O-ring (from Wilmad LabGlass Company) was used to maintain zero hydration level of the sample. To test the efficiency of the O-ring, a sample of MCM-41 with known hydration was prepared. The NMR spectrum was recorded, and then the sample was left for three weeks. Both mass of the sample and the area under its NMR line was found unchanged. This procedure was repeated for another sample that was left for six months. Again, neither the area under NMR line nor the mass changed. These two tests confirmed the effectiveness of the O-ring with the rotor cap in maintaining the hydration level of the prepared NMR sample. It is worthwhile to mention that, from our experience, the O-ring needed to be replaced with a new O-ring after using it for two or three different samples. This is important especially if the O-ring already has been used for a sample that was studied over a range of temperatures.

For the preparation of hydrated samples, the same drying process was repeated but in this case the dried sample is moved (while under vacuum) to a desiccator in which 100% relative humidity of D_2O is maintained. All handling of the sample (placement into or removal from the desiccator, capping the sample rotor) was done inside a glove box of flowing dry nitrogen gas. The sample was left in the desiccator for a specific length of time dictated by the hydration level desired. The hydration level was calculated from the known mass of the rotor, the dry powder, and the D_2O added to the sample during the hydration. For the mass measurements, an electronic balance, model A200DS from Denver Instrument company with accuracy of $\pm$ 0.5x 10^{-5} gm, was used.

Four different samples hydrated with D_2O were prepared by this method (0.2D, 0.6D, 1.6D and FullD). The numbers preceding the letters stand for the number of monolayers of water covering the pore surface of MCM-41. Letter D

indicates that the samples are deuterated (hydrated with D_2O).

Second category: These samples were prepared in order to identify and characterize the hydration sites in MCM-41. In this case the calcined powder of MCM-41 is hydroxylated using H_2O or D_2O by following the same procedure described previously. Then the powder samples from both the H_2O and D_2O batches were heated for 52 hours, at 400 ^oC or at 800 ^oC, and then allowed to cool to room temperature in a nitrogen glove box, before being used for the final NMR sample preparation. A similar method as described for the first-category sample preparation, was followed to dry or hydrate several samples (protonated and deuterated). These samples are denoted as 0H400, 0.2H400, 0.2D400, and 0H800. The numbers preceding the letters have the same meaning as defined before. Letter H, refers to the samples hydrated using H_2O and letter D refers to the samples deuterated and hydrated using D_2O. The numbers following the letters refer to the temperature at which the MCM-41 was treated thermally, after the calcination process, but before hydration. The samples in both categories are listed in Table (4.1)

MCM-41	**Sample Names**				
Normal condition	0D	0.2D	0.6D	1.6D	FullD
Heated to 400 ^oC	0H400	0D400	0.2H400	0.2D400	–
Heated to 800 ^oC	0H800	–	–	–	–

Table 4.1: List of samples used in this study. The letters and numbers are defined in the text. For example, 0.2H400 stands for a sample of MCM-41 that was heated to 400 ^oC after it was already calcinated and hydroxylated. After heating and subsequent cooling to room temperature this sample was hydrated with H_2O to the 0.2 monolayer level.

4.4 The Spectrometer

All NMR measurements in this study were performed using a 11.7 Tesla ultra shield magnet with a Bruker DMX500 spectrometer. For the MAS experiments, a Bruker MAS probe with a Zirconia rotor of 4 mm outer diameter was used. A special rotor cap with O-ring, obtained from Wilmad LabGlass Company, was used to maintain the hydration level in the sample. For some measurements a solids NMR probe was utilized.

4.5 Chemical Shift Calibrations

Chemical shifts for ^{1}H spectra were referenced to 2, 2-dimethy l-2- silapentane-5- sulfonate (DSS) through the water resonance. In the case of ^{2}H spectra, liquid D_2O of 99.9% purity was used by setting its peak position to 4.8 ppm with respect to zero chemical shift of DSS. Referencing the chemical shift for silicon in the case of ^{1}H -^{29}Si CPMAS spectra was done by using the zero chemical shift of DSS, together with the proton and silicon gyromagnetic ratio [103] ($\gamma_{\mathrm{Si}}/\gamma_{H}$= 0.19867211). The frequency corresponding to zero chemical shift of DSS is multiplied by this ratio and then this frequency is found in the ^{1}H -^{29}Si CPMAS spectrum and set to zero ppm.

4.6 Temperature Calibration

Data were taken for some samples over a range of temperatures (from 213 to 343 K). For measurements performed at temperatures below room temperature, nitrogen gas was cooled using a heat exchanger immersed in a dewar filled with liquid nitrogen and passed through a vacuum gas transfer tube inserted in the MAS probe. This tube is provided with a heater inside it to increase the temperature of the cold gas to the desired temperature. The temperature is sensed by a thermocouple placed close to the sample and controlled using a temperature controller of type BVT3000 provided with the spectrometer. For measurements

performed at temperatures higher than room temperature nitrogen gas, at room temperature, was passed through the gas transfer tube where it was heated by the heater to the desired temperature. For each measurement at a specific temperature, a period of 15 minutes was allowed before data acquisition to ensure that the entire sample has reached the desired temperature. In all cases the temperature is controlled to within $\pm$ 0.1 K.

To determine the correct temperature sensed by the sample a temperature calibration test was performed using pure methanol [107], which is suitable for the temperature range 178 to 330 K. The proton spectrum for pure methanol (CH_3-OH) typically shows two peaks in the range 3 to 5.5 ppm. The difference between these two chemical shifts is very sensitive to the temperature and can be used for temperature calibration.

The equation that governs the relationship between the calibrated temperature (T_c) and the difference between the two proton chemical shifts $\Delta\delta$ in pure methanol is given as [107]

$$T_c(K) = 409 - 36.54\ \Delta\delta\ - 21.85\ (\Delta\delta)^2 \tag{4.8}$$

The temperature calibration curve is shown in Figure (4-4).

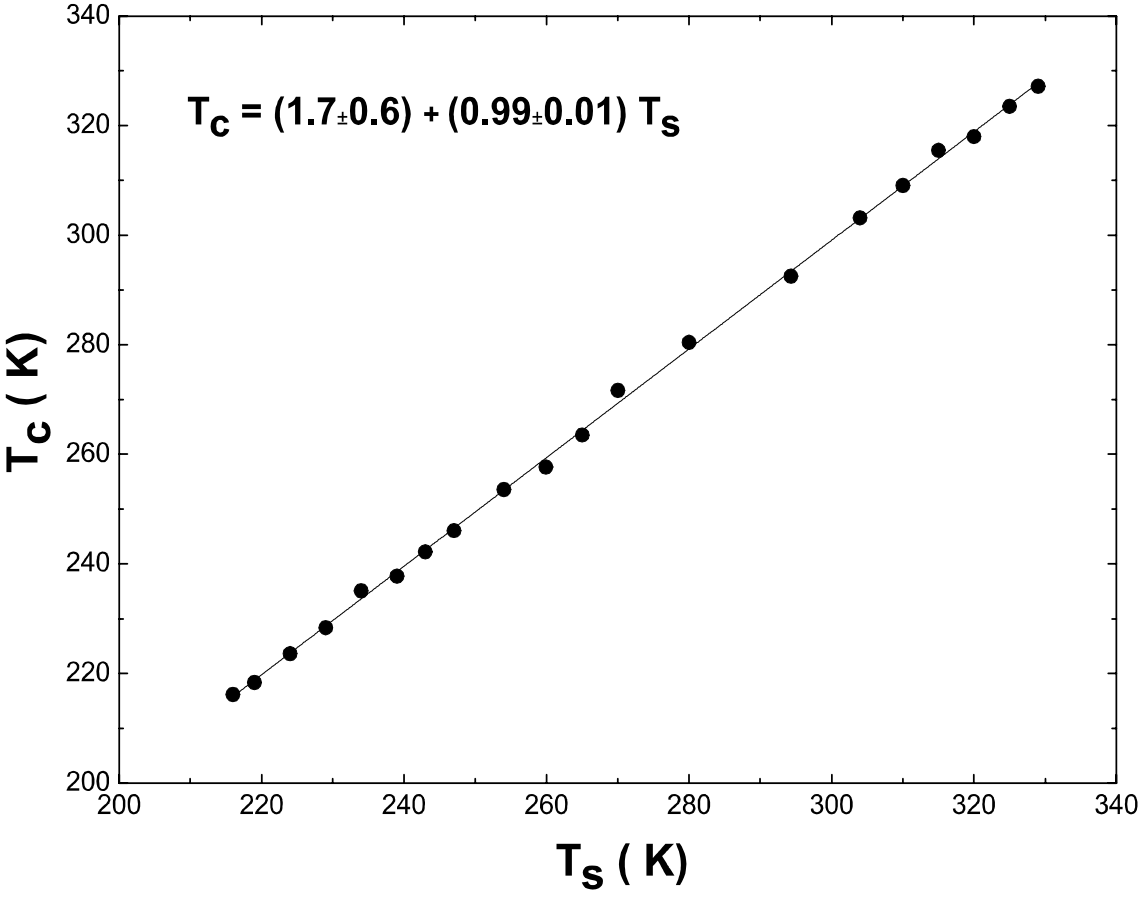

Figure 4-4: Temperature calibration for samples positioned in the MAS probe using pure methanol. T_c and T_s are calibrated and sample temperatures, respectively.

4.7 NMR Experiments

The following is a brief description of data acquisition parameters and pulse sequences used in the NMR experiments of this study.

4.7.1 ^{2}H Spectra

The quadrupolar echo sequence (Davis *et al.* [17]) was used to acquire ^{2}H spectra at 76.77 MHz in this study. The pulse sequence is described as

$$90^o_x - t_e - 90^o_y - t(Aqc) - Rep.Time$$

The sequence is effective in overcoming the dead time of the NMR probe by causing the formation of an echo at a time t_e after the second pulse so that fast-decay signals can be properly recorded. To eliminate the possibility of the formation of artifacts, due to the use of the solid echo sequence [108], 16 phase cycling (for both the transmitter and receiver) has been used [109]. The main reason for using this sequence, instead of a single pulse, is to be able to capture all of the spectral width of water ^{2}H and to record at least a portion from the surface O-D signal of the deuterated and dried NMR samples of MCM-41. The 90^o pulse was set to 9 μs with t_e of 14 μs. The dwell time was set to 0.5 μs and the dead time was 4.5 μs.

^{2}H spectra of different samples (0D, 0.2D, 0.6D, 1.6D and FullD) were recorded. For the 0D sample, the spectra were recorded only at room temperature because in this case it took 25 hours to obtain a spectrum with a reasonable signal-to-noise ratio.

For the hydrated samples, data over a range of temperatures between 213 K to 333 K were collected.

For the 0D sample a repetition time of 6 s was used with 15 k accumulation. Although the motion of the O–D group would not be isotropic, we assume isotropic motion so as to obtain a rough estimate for T_1 in this sample. Then using T_1(=2.1 s [30]) of dry protonated MCM-41 gives 2.1 s/ 6.5 s (ratio of proton

T_1 in pure H_2O/ deuteron T_1 in pure D_2O) $\simeq$ 0.3 s for the deuterated MCM-41. In order to make certain that full recovery of M_z is achieved a repetition time of 6 s was used. For the 0.2D sample a repetition time of 300 ms was used and 15 k scans were accumulated. The repetition time was increased with the hydration level of a sample; 1.2 s, 2 s and 5 s corresponding to samples 0.6D, 1.6D and FullD, respectively. 2 k accumulations were used for samples 0.6D and 1.6D, while 500 scans were used for the FullD sample.

4.7.2 ^{1}H Spectra

A single pulse sequence [90^o_x— $t(Aqc)$] was used for all ^{1}H MAS spectra at 500 MHz in this study. The pulse duration for the 90^o pulse is set to 5 μs with a repetition time of 9 s for the dry sample and 5 s for the hydrated samples. The spinning rate was set to 10 kHz. All ^{1}H spectra were accumulated at room temperature.

4.7.3 ^{1}H - ^{29}Si CPMAS

The ^{1}H- ^{29}Si CPMAS spectra were acquired at 99.36 MHz with a spinning rate of 10 kHz. The pulse sequence is described in detail in section (2.4). Different mixing times, from 1 ms to 12 ms, were tested to check for the maximum signal intensity. The result indicated that the signal intensity slowly increased to reach a peak at around 8 ms and then dropped slowly when increasing the mixing time beyond 8 ms. Therefore, the mixing time was set to 8 ms for all ^{1}H- ^{29}Si CPMAS measurements. The repetition time was set to 3 s. All spectra were signal averaged by accumulating 10 k scans that took approximately 9 hours. In the case of the dry sample (0H800) of MCM-41, 70 k accumulation were performed with a repetition time of 5 s that took 4 days of acquisition. All spectra were acquired at room temperature.

4.7.4 2D Measurements

2D measurements were carried out only for the 0.2D sample at different temperatures, in order to further investigate exchange between different spin groups within this sample. Two different experiments were performed. For the first 2D measurements the pulse sequence used consist of four 90^o pulses described as

$$90^o_x - t_1 - 90^o_x - Mixing\ Time(t_m) - [\ 90^o_x - t_e - 90^o_y\ ] - t_2(Aqc) - Rep.\ Time$$

The first 90^o_x pulse creates transverse magnetization. The evolution time $\mathbf{t}_1$ is included to serve as frequency-labeling of the various magnetization components by their Larmor frequencies, as described in detail in section (2.6). The data were obtained at 233 K, 253 K, and 293 K. To remove the possibility of interfering artifacts due to multiple quantum coherences, which appear as cross peaks, a series of 32 phase cycling [111] was used. This is extremely useful, especially if one needs to study magnetization exchange rates at very small $\mathbf{t}_m$ values [112]. Multiple mixing times $\mathbf{t}_m$ were used. The 90^o pulse was set to 9 μs and 256 scans were accumulated during the $\mathbf{t}_2$ period and 128 scans during the evolution time $\mathbf{t}_1$**.** The increment for $\mathbf{t}_1$ was done automatically by the Bruker spectrometer. The starting value for $\mathbf{t}_1$ was set to 20 μs. The probe dead timing parameter was set to 4.5 μs**.**

In the second 2D measurements (at room temperature), Cos Cos and Sin Sin pulse sequences, as explained in section (2.6), were used. These measurement were aimed at dealing with the cross peaks in the powder pattern that are not due to exchange processes. Such data were acquired only at room temperature for different mixing times ($\mathbf{t}_m$ = 100 μs, 200 μs, 600 μs, 1 ms, 10 ms, 20 ms, and 50 ms). In this case, the 90^o pulse was set to 4.5 μs and 1 k scans along $\mathbf{t}_2$ were recorded for each of 128 values of $\mathbf{t}_1$.

4.7.5 Double Quantum Measurements

The reason for measuring double quantum spectra in this study was to estimate the time range of the double quantum coherences that would participate in producing some of the cross peaks artifact in the 2D measurements. Double quantum spectra were measured using a pulse sequence of three 90^o pulses ([9] and [110]) as follows

$$90^o_{\varphi 1} - \tau - 90^o_{\varphi 2} - t - 90^o_{\varphi 3} - Aqc.$$

where τ is the evolution time which is set to different values in order to obtain different double quantum spectra. 90^o was set to 9 μs. Acquisition involved 15 k accumulations with a repetition time of 300 ms, a probe dead time set to 4.75 μs, and a dwell time of 3.32 μs. In order to generate double quantum coherences, the phase cycle summarized in the following Table was used.

1st pulse	**2nd pulse**	**3rd pulse**	**Receiver**
0	0	0	0
0	0	60	180
0	0	120	0
0	0	180	180
0	0	240	0
0	0	300	180

Table 4.2: Phase cycles used for the double quantum measurements.

Evolution times of 20, 40, 60, 160, 220, 280, 350, 400, 450, and 500 μs were used for the double quantum spectra at room temperature for the 0.2D sample only.

Chapter 5

Results and Discussion

5.1 Dry MCM-41

As a starting point for the study of the behavior of water molecules in mesoporous MCM-41, it is important to characterize the pore surface silanol groups as these also contribute to the overall NMR signal when water is introduced. For this reason the ^{2}H spectrum of a dry, deuterated sample (0D) was recorded (Figure (5-1)). In this sample all the O-H groups have been replaced by O-D. The spectrum, which consists of contributions from all the silanol groups (single and H-bonded), was fitted to a Gaussian line with a FWHM of 32.6 kHz. This line width is considerably less than the splitting expected for deuterons of OD in the rigid lattice regime ($\nu_q \simeq 160$ kHz [105][106]). In addition, the line did not exhibit structure (e.g., powder pattern features). In part this can be attributed to a certain degree of motional averaging (in particular for the single OD groups) as an OD group rotates about the Si-O bond. In addition, the pulse width of 9 μs used in this experiment does not have sufficient spectral width to fully excite the complete ^{2}H resonance so that the integrated signal does not fully represent the sample magnetization and spectral features tend to be diminished.

The T_1 of the dry, deuterated sample was not measured because of the sample's low signal-to-noise ratio (the spectrum of Figure (5-1) took about 25 hours

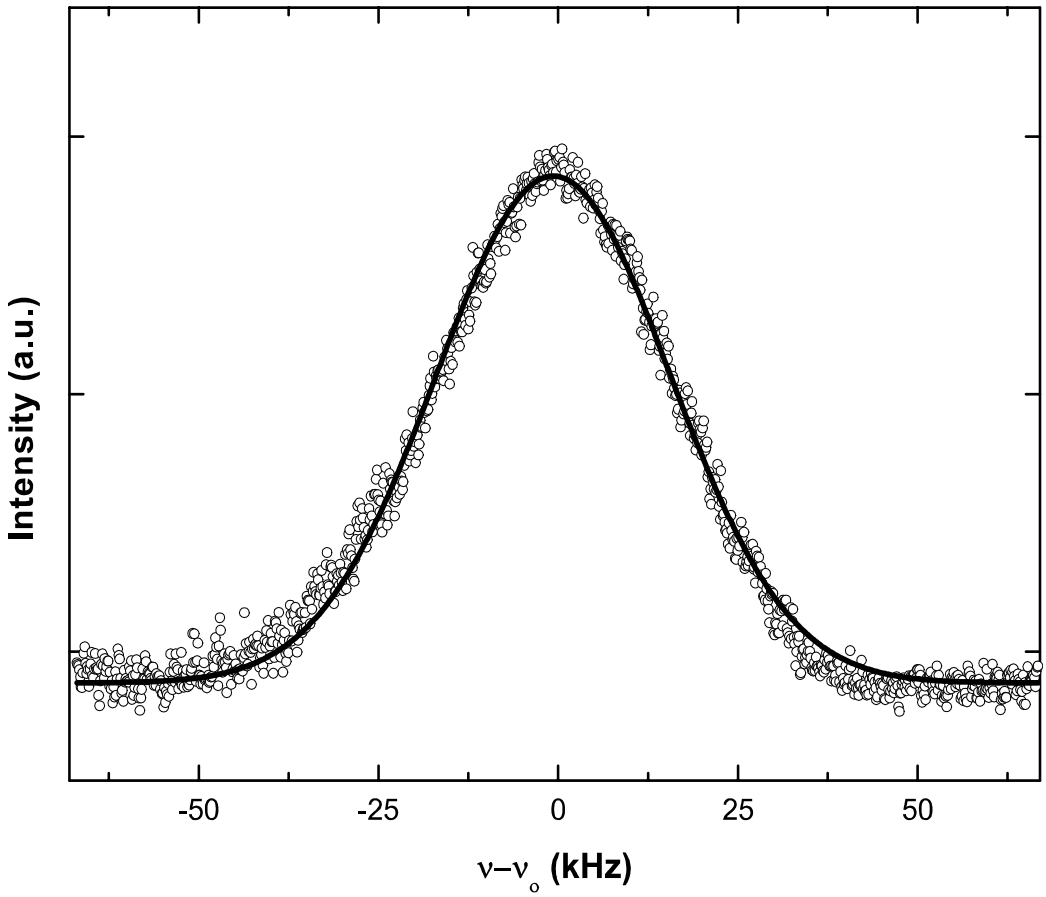

Figure 5-1: ^{2}H spectrum for the dry, deuterated sample of MCM-41 (0D) at room temperature and 76.6 MHz. The solid line represents the fit of a Gaussian curve with FWHM of 32.6 kHz to the data. The quadrupolar echo sequence, with repetition time of 6 s, was used and 15 k scans were accumulated.

to acquire). However, a rough estimate of T_1 ($\simeq$ 0.3 s) for this case was made in section (4.7.1). In the present experiments a repetition time of 6 s was used.

5.2 Low Hydration Sample

When water molecules are added to the dry powder of MCM-41, they will bond to the silanol groups via hydrogen bonds. In order to study water behavior, in the pores of MCM-41 extensive ^{2}H spectral measurements were first made in samples hydrated to 0.2 monolayer, which corresponds to approximately one water molecule per OD group. In such low-hydration samples, no free (bulk) water is expected. The spectra were recorded over the range of temperatures from 223 K to 243 K, using a spectral width of 1 MHz.

Figure (5-2) shows a typical ^{2}H spectrum for the 0.2D sample at room temperature. The spectrum shows three different signal components. The broad component that extends over about 90 kHz with FWHM of about 30 kHz (if a Gaussian curve is fitted to this part) can be assigned to the OD groups on the MCM-41 pore surface (see spectrum for dry, deuterated MCM-41, Figure (5-1)). A powder pattern with a splitting of about 4 kHz, and a Lorentzian line at the center with FWHM of about 400 Hz (see inset of Figure (5-2)), can be assigned to water molecules adsorbed at different sites with different environments. It also may be noted that the central line is not due to a free water pool as the sample hydration is too low.

Throughout the temperature range studied, the broad resonance line associated with the OD groups maintains its shape and amplitude suggesting that it is not affected by magnetization exchange between OD groups and water deuterons. Therefore, in the magnetization exchange scenario discussed here, this group has been excluded and the focus is only on the exchange between water deuterons.

Figure (5-3) shows the experimental water deuteron spectra for the 0.2D sample over the temperature range from 213 to 333 K. Each individual spectrum

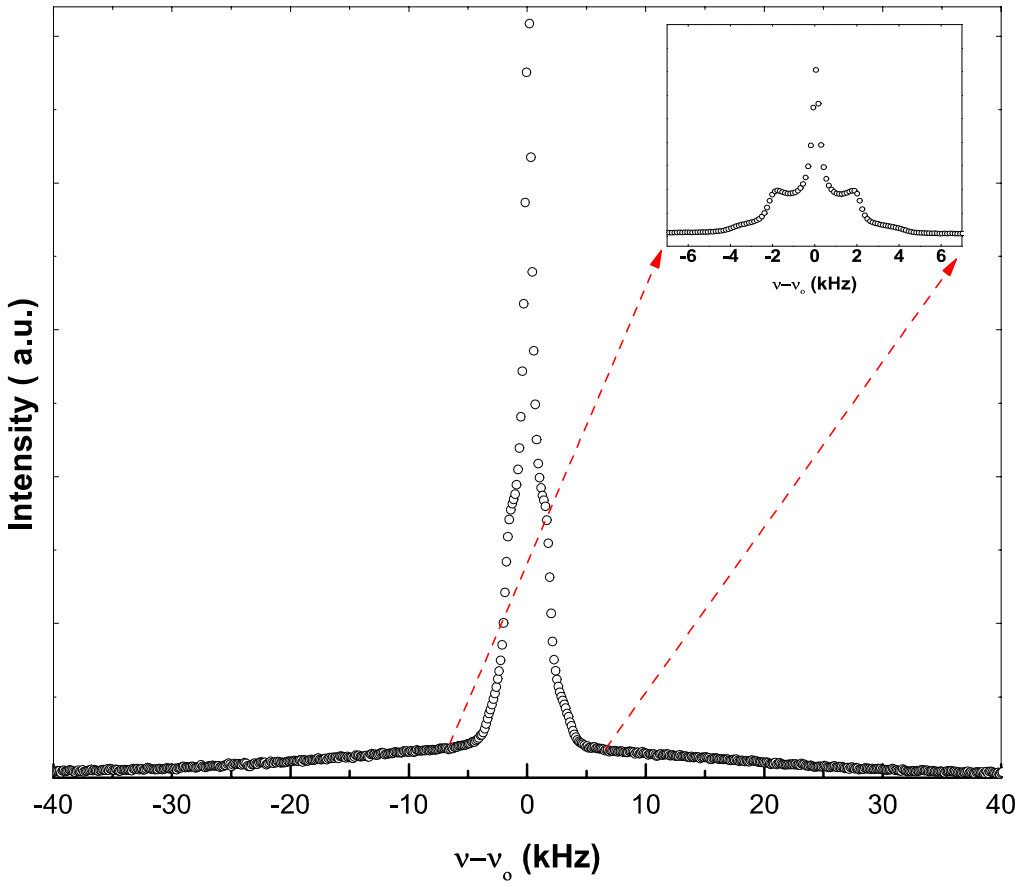

Figure 5-2: Typical ^{2}H spectrum of low- hydration sample of MCM-41 (0.2D) at room temperature. The inset shows an expanded view of the spectral part within the arrows.

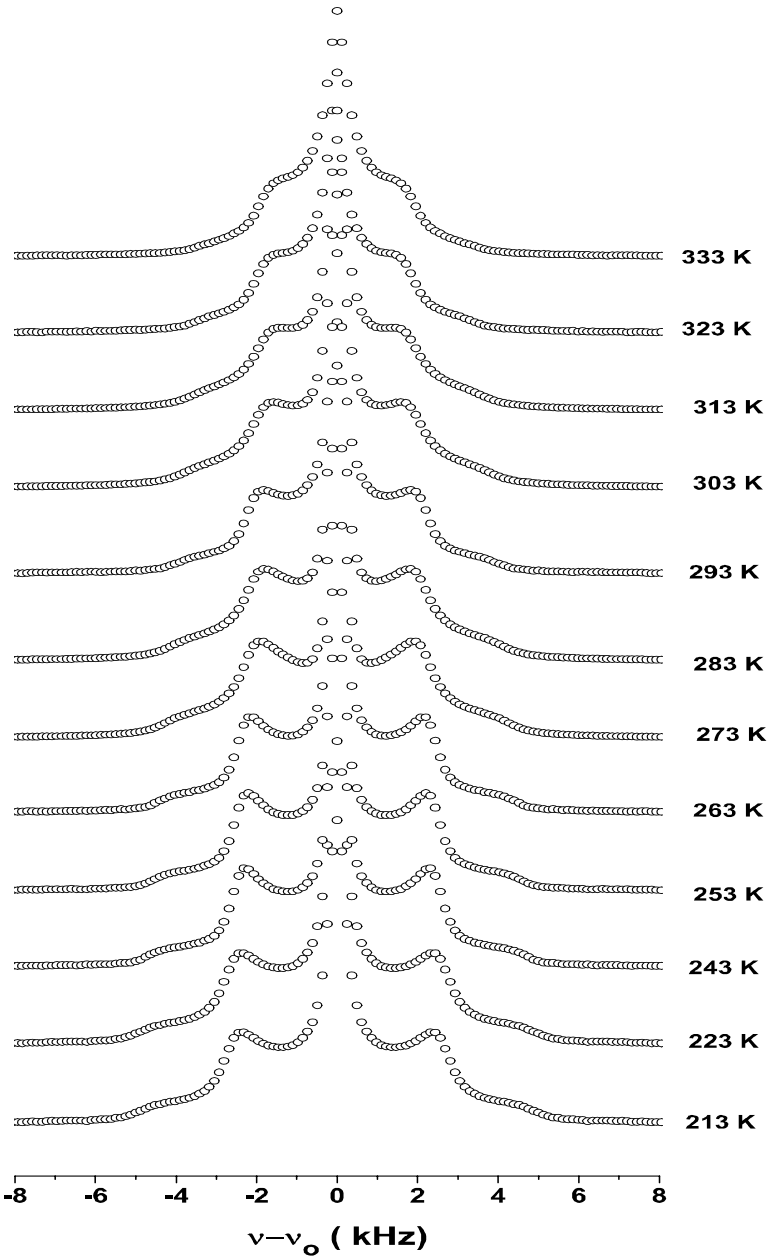

Figure 5-3: Experimental ^{2}H spectra for 0.2D sample versus temperature. Each spectrum exhibits a powder pattern line shape and a Lorentzian line at the center. 15 k scans with a 300 ms repetition time, were utilized.

exhibits a Pake powder pattern [6] and a Lorentzian line at the center. Such spectra have been observed in the literature for MCM-41 [9] and compare well to the spectra of Figure (5-3). The powder pattern is due to deuterons of molecules undergoing anisotropic motion that does not completely average out the secular part of the quadrupolar Hamiltonian (equation (2.32) on page 14). The Lorentzian line is due to some of the water molecules undergoing more rapid and less anisotropic motion that tends to further motionally average the quadrupolar Hamiltonian. In other words, the data suggests that water molecules in MCM-41 are in two different dynamical environments. Furthermore, the powder pattern has a much smaller splitting than that for the rigid lattic case (the latter has a splitting of about 160 kHz [105][106] while here the splitting is about 3-5 kHz throughout the temperature range studied). This suggests that the anisotropic motion has a component with frequency larger than the rigid lattice linewidth (see section 2.3).

Figure (5-3) shows that as the temperature increases the splitting of the powder pattern becomes smaller, while the Lorentzian line gets broader. This is an indication that exchange it occurs between these water deuterons and that such exchange is thermally activated. This kind of exchange is not trivial to treat as it occurs between a site with Lorentzian line and a site with a powder pattern line shape. Although the literature contains many investigations of exchange between groups with Lorentzian resonance lines, the present exchange scenario does not appear to be treated in the literature.

Before utilizing exchange models to analyze the present data a ^{2}H simulation program (MXQET) is introduced and used to simulate some cases of motional exchange in order to acquire insight into the effect of certain molecular motions on the spectra (e.g., [18][113][114][115]).

5.2.1 Simulation of Spectra using Exchange Motion Model

As already suggested above, the first inclination is to assign the powder pattern and Lorentzian resonance line features to separate water groups within the sample. However, the possibility that all water molecules are undergoing specific dynamics at their hydration sites such as to yield the observed water deuteron lineshape needs to be addressed.

Different programs have been used for ^{2}H lineshape simulation. A commonly used simulation program is MXQET[1] which is a FORTAN program described in the literature [116][117]. The program calculates quadrupolar powder patterns for n site exchange with different jumping frames. The main feature that distinguishes MXQET from many other ^{2}H spectra simulation programs is that MXQET works on the basis of producing time domain data rather than frequency domain data. The main application of the MXQET program is to calculate FID data points following the echo, produced using the quadrupolar echo pulse sequence. Such data are Fourier transformed in order to generate the lineshape. The program takes into consideration effects on the spectra which can arise when exchange processes (due to molecular motion) occur on a time scale comparable to the inverse of the splitting. The full mathematical description of this program is given in reference [116].

The input to MXQET consists of the number of sites, the Euler angles that determine the orientation of the eq_{zz} of each site with respect to a rotation axis in the molecule under study, the exchange rates between the sites, the duration of the 90^o pulse in the quadrupolar echo sequence, and the time between the two pulses. MXQET is capable of performing simulations for different exchange scenarios such as exchange between nearest neighbors, exchange between all sites or mutual exchange between specific sites.

The program begins by calculating the site frequencies and the exchange matrix, and then the echo signal, followed by powder averaging to account for dif-

[1] MXQET stands for Multi Axes Quadrupolar Echo Tiling.

ferent orientations of crystallites in the sample. The final step involves Fourier transformation of the time domain data in order to obtain the ^{2}H lineshape. Visual comparison between experimental and simulated lineshapes is usually used in an iterative process to determine best agreement between the two cases and thus to finalize the exchange details.

A few representative ^{2}H lineshape simulations for two-site and three-site exchange models are presented in Figures (5-4) and (5-5), respectively. Exploring various possibilities it became apparent that the observed spectrum cannot be represented using this model. A case that resembles the observed spectrum insofar as the presence of the central peak is concerned, is that shown in Figure (5-6) for intermediate exchange. However, inclusion of the central peak always resulted in the absence of the classical step- like termination of the wings of the powder pattern.

Within the present context most of the simulation programs, including MX-QET, are designed to address motional exchange in which the motion makes the atoms exchange position with the neighboring atoms within the same molecule. In the present case whole molecules are expected to exchange with each other as suggested by the ^{2}H spectra of Figure (5-3). Therefore the magnetization exchange of water deuterons in MCM-41 is further analyzed using two-site and multi-site exchange models as discussed in the next two sections.

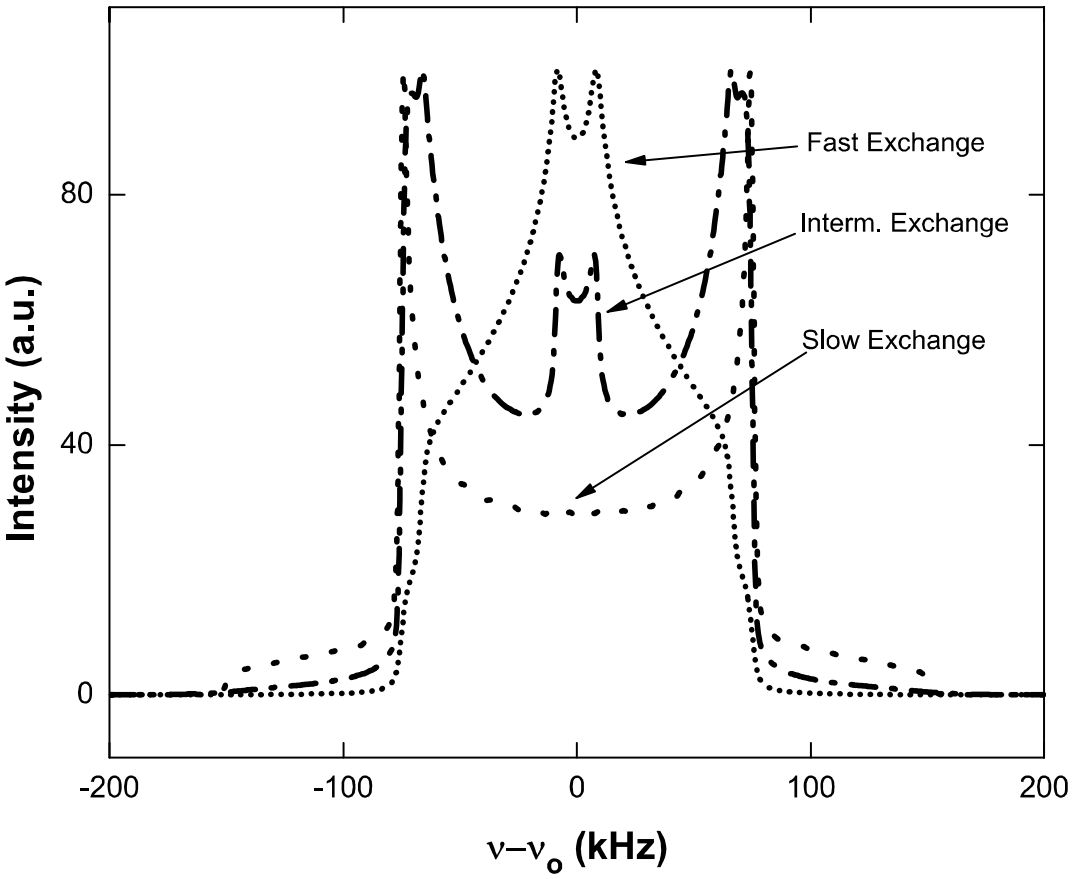

Figure 5-4: ^{2}H lineshape simulation for a two-site exchange scenario for different exchange rates using the MXQET program. Notice the reduction of the quadrupolar splitting as the exchange rate becomes much larger than the rigid lattice splitting. In this simulation the angle between eq_{zz} at a site and the director was set to 52.5^o and the direction of eq_{zz} at the two sites are separated by an angle of 180^o.

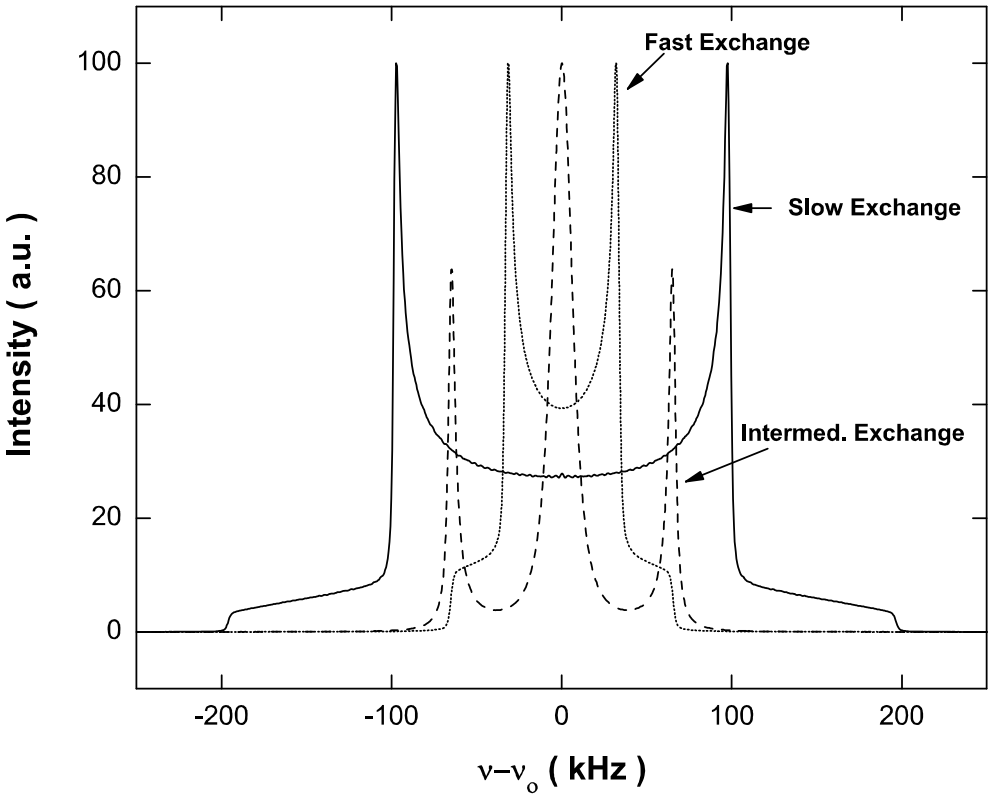

Figure 5-5: Simulated ^{2}H lineshape of deuterons within a three-site exchange scenario at different exchange rates using the MXQET program. The angle between eq_{zz} at each site and the director was set to 109.5^o, while the directions of eq_{zz} at the sites are separated by an angle of 120^o.

5.2.2 Simulation of Spectra using Two-Site Exchange Model

The magnetization exchange between water deuterons was analyzed using a two-site exchange model described in section (2.5.1). This exchange model is applicable to exchange between two spin systems exhibiting Lorentzian resonance lines (or exponential FIDs). Although such a model will not give precise, quantitative result for the present case involving exchange between the water deuteron spin groups in MCM-41 with Lorentzian and powder pattern resonance lines, it is expected to give insight into the exchange process in this system.

Each ^{2}H spectrum of the low hydration sample (0.2D) was de-convoluted into a powder pattern and a Lorentzian line, as described in section (2.2) using Mathcad software (see Appendix B). A typical de-convolution result is shown in Figure (5-6) for 273 K. The parameters obtained from the de-convolution process, as a function of temperature, are summarized in Table (5.1). The magnetization fractions, at each temperature, were calculated from the area under the powder pattern and Lorentzian line using the de-convoluted curves. T_2 for the Lorentzian line was calculated from the FWHM ($\Delta\nu_L$ of Table 5.1) value using equation (2.52) on page (28).

The magnetization fractions and T_2 values are plotted as a function of 1000/T in Figure (5-7). T_2, labelled "liquid-like" , increases with increasing temperature, reaches a maximum at approximately 243 K and then starts to decrease with increasing temperature. Such behaviour is an indication of magnetization exchange between the two water sites. To fit the two-site model to the data, T_2 values in the low temperature range, below 243 K, were assumed to be intrinsic values. The straight line behaviour over this temperature range suggest that an Arrhenius law applies. A fit of $T_2 = T_{a0} \exp(-E_a/RT)$ to these data gives an activation energy of 4 kcal/mole and T_{a0}= 8039 ms. The solid lines in Figure (5-7) represent the best fit using a program developed in our laboratory [30], which is based on equations (2.48) and (2.49) on pages 26 and 27 for two-site exchange. The parameter tau_{ex} is the time constant for exchange of magnetization from the water molecule

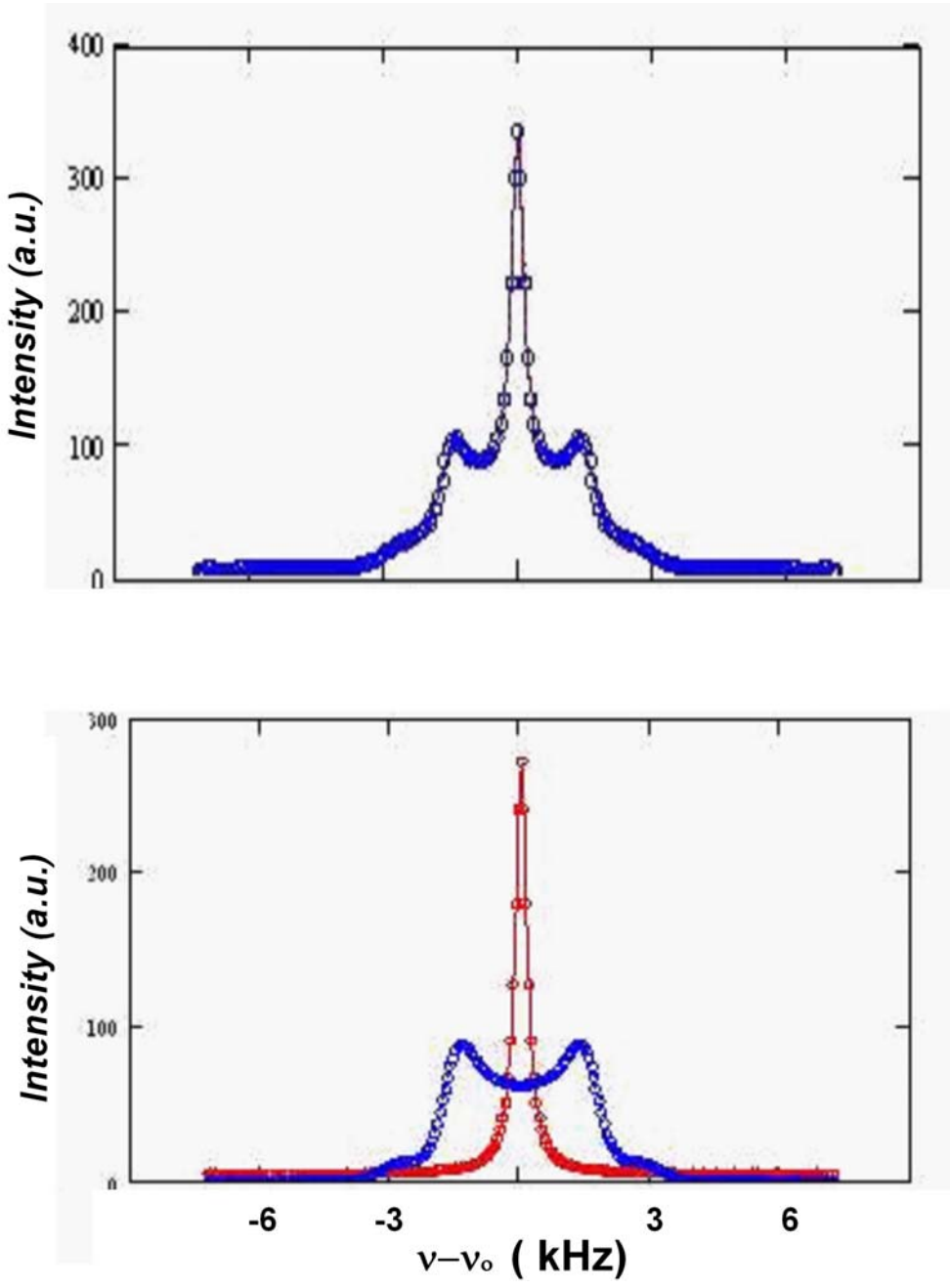

Figure 5-6: Typical de-convolution of ^{2}H spectrum of 0.2D sample, at 273 K, using the method described in section (2.2). The spectrum is de- convoluted into a powder pattern and a Lorentzian line.

T(K)	**1000/T(K)**	**PA(%)**	**LA(%)**	$\Delta\nu_Q$**(Hz)**	**C1**	**C2**	$\Delta\nu_L$**(Hz)**
223	4.5	61.7	38.3	5390	13.17	231	498
228	4.4	62.0	38.0	5320	13.45	227	309
233	4.3	61.5	38.4	5190	13.56	228	284
238	4.2	61.8	38.2	5110	13.58	220	263
243	4.1	62.2	37.8	5040	13.64	213	256
248	4.0	62.7	37.3	4970	13.79	209	248
253	3.9	63.2	36.8	4910	13.95	205	253
257	3.9	62.8	37.2	4840	13.86	202	257
263	3.8	62.4	37.6	4750	13.78	199	273
273	3.7	62.9	37.1	4570	13.78	191	283
283	3.5	62.7	37.3	4410	13.87	189	322
293	3.4	61.3	38.7	4340	13.52	189	388
303	3.3	60.9	39.1	4090	13.64	192	441
313	3.2	59.6	40.4	3880	13.39	196	526
323	3.1	58.5	41.5	3690	13.34	198	613
333	3.0	56.5	43.5	3500	12.93	205	695
343	2.9	54.0	45.9	3360	24.85	431	775

Table 5.1: Parameters obtained from de-convolution of the deuteron spectra of 0.2D sample using equations explained in section (2.2). PA and LA are the areas under the powder pattern and Lorentzian line, respectively. The labels L and Q refer to Lorentzian and powder pattern, respectively and b refers to the baseline of each spectrum. C1 and C2 are the scaling factors. The absolute uncertainties of these parameters were found not to depend on temperature, and are 60 Hz and 10 Hz for the quadrupolar splitting and Lorentzian line width, respectively, and 0.5% for PA and LA.

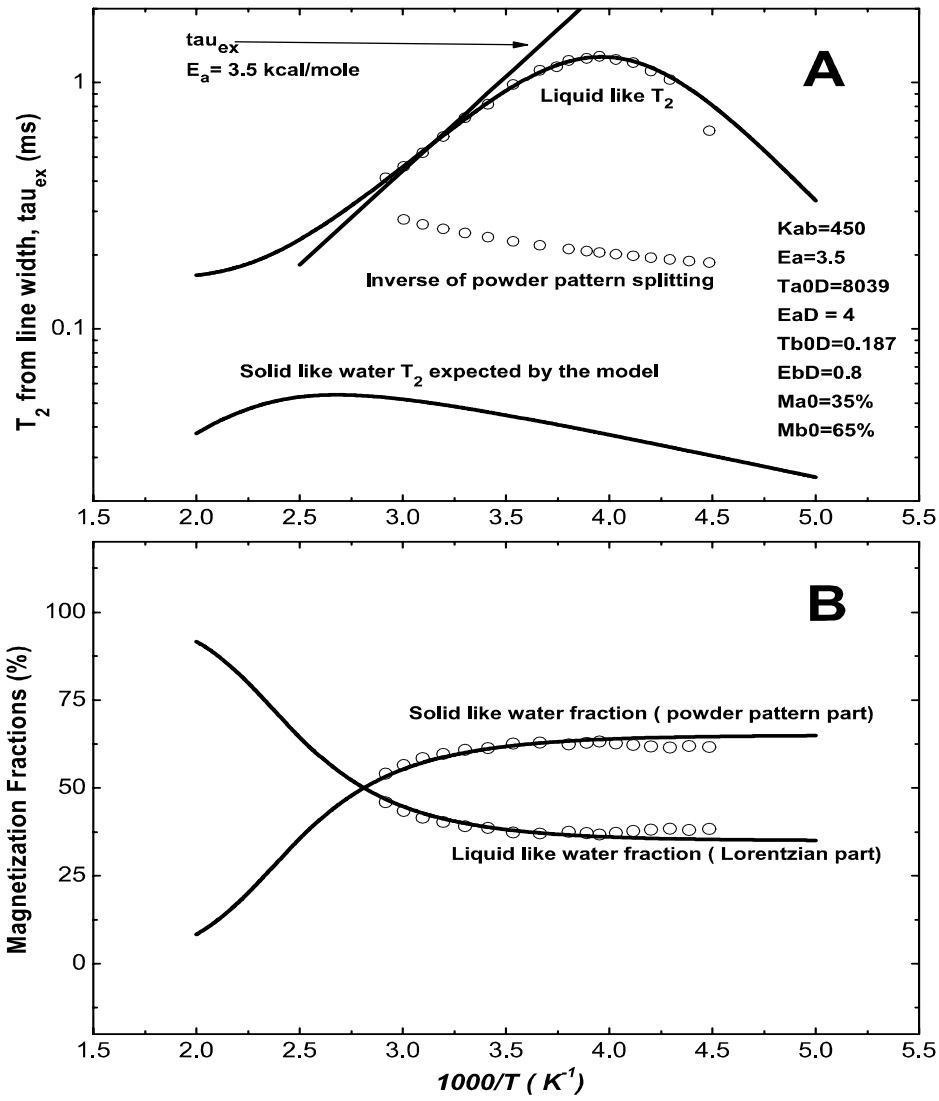

Figure 5-7: Water deuteron magnetization fractions (B) and T_2 values (A) versus inverse temperature for the 0.2D sample. For the powder pattern the inverse splitting is plotted as "T_2". The lines are calculated from the two-site exchange model discussed in the text. The list of parameters on the right hand side of (A) are the adjustable parameters in the model producing the best fit to the data. Here "a" and "b" are labels used for the Lorentzian and powder parts, respectively. Kab is the exchange rate at infinite temperature and Ea is the activation energy for the exchange rate. Ta0D and Tb0D are the T_2 at infinite temperature for deuterons at sites a and b, respectively, and EaD and EbD are the corresponding activation energies. Ma0 and Mb0 are the intrinsic magnetization fractions.

site with Lorentzian line to the site with the powder pattern line shape. In the fitting process, all the components were calculated simultaneously but only the T_2 of the Lorentzian and the two magnetization fractions were used as adjustable parameters. The fitted model parameters are given in part (A) of Figure (5-7). The fit predicts the shorter T_2 to be below the inverse of the powder pattern splitting. The activation energy for the exchange time constant tau_{ex} obtained from this preliminary approach is 3.5 kcal/mole, which is consistent with results for similar low-hydration samples of MCM-41 studied using dielectric relaxation spectroscopy [90], but somewhat lower than the value (5.2 kcal/mole) found in a recent proton NMR study [30] in MCM-41.

5.2.3 Simulation of Spectra using Multi-Site Exchange Model

The ^{2}H data of low hydration sample (0.2D) versus temperature have been analyzed using a multi-site exchange scenario proposed by Woessner [31] described in section (2.5.2). In this approach, anisotropic spectrum (powder pattern lineshape in our data) of ^{2}H spectra can be expressed by multi-Lorentzian lines of equal linewidths but with different populations described by equation (2.57) on page (29). These Lorentzian lines cover the envelope of the powder pattern line. Using this approach, the exchange process in our sample converts to an exchange among many Lorentzian lines.

The powder pattern shape of ^{2}H spectra of the 0.2D sample was represented by 48 Lorentzian lines of equal linewidths, 636 Hz (T_2= 0.5 ms) and the center line is expressed using only one Lorentzian line. From initial simulation tests, a smaller number of sites was not enough to reproduce the experimental shape and a higher number of sites did not generate a more accurate result but needed more time for the computer simulation. A computer program based on the Woessner approach [31] within Origin Pro 7 software (see [30]) was used to simulate the ^{2}H spectrum at a given temperature. Different parameters including the magnetization exchange rate constant were optimized in the fitting. Low temperature T_2 of the central Lorentzian line of the ^{2}H spectra were fitted to an Arrhenius type equation in order to extract intrinsic[2] T_2 for the deuterons with the Lorentzian line over the entire temperature range studied (see Figure 5-10). This fit gives an activation energy E_a of 3.8 kcal/mole and a pre-exponential factor of 3.9x10^3 ms. The intrinsic values of the powder pattern splitting ($\Delta\nu_Q$) were taken from a straight line fit (on $\Delta\nu_Q^{-1}$ versus 1000/T plot, Figure 5-10) to the experimental values of $\Delta\nu_Q^{-1}$ from 223 to 273 K ($\Delta\nu_Q^{-1}$(ms)=0.36-0.04(1000/T)). The intrinsic populations for both sites were estimated by averaging the low temperature (from 223 to 273 K) populations for each site (see Figure 5-10). This way the

[2]labeled T21 in the multi-site exchange model program used here for the simulation.

T(K)	1000/T(K)	$\mathbf{Y_o}$(a.u.)	$1/2\Delta\nu_Q$(Hz)	**T**21x10^{-3}(s)	**V**1(s^{-1})
223	4.5	5.94	2700	0.66	83.89
233	4.3	6.14	2562	1.0	157.23
243	4.1	6.18	2518	1.36	173.89
253	3.9	4.95	2435	1.86	257.83
263	3.8	6.11	2359	2.5	316.23
273	3.7	5.24	2288	3.3	422.78
283	3.5	5.59	2222	4.2	512.23
294	3.4	5.87	2160	5.3	670.13
303	3.3	5.99	2100	6.6	793.47
313	3.2	5.68	2050	8.1	953.21
323	3.1	5.80	2000	9.8	1090.99
333	3.0	5.14	1952	11.0	1302.43
343	2.9	11.4	1900	13.0	1502

Table 5.2: Parameters optimized during fitting of ^{2}H spectra in the 0.2D sample using the multi-site exchange model discussed in the text. The parameters are defined in the text. Typical uncertainties for these parameters, for all temperatures, are indicated in connection with the fit at 243 K as in Figure (5-8).

intrinsic magnetization fractions M_P= 2.0 and M_L= 1.2 (corresponds to M_P= 62.3% and M_L= 37.6%) were obtained. The subscripts P and L label the powder pattern and the Lorentzian line of the ^{2}H spectra. The adjustable parameters in the simulation were the scaling factor (mag), base line (Y_o) and exchange rate constant (V1) described in section (2.5.1). A typical simulation result, along with the best-fit parameters, is shown in Figure (5-8) while Figure (5-9) shows a stack-graph of all experimental spectra together with the lines calculated using parameters obtained from the fitting. The best-fit parameters are summarized in Table (5.2).

Figure (5-10) shows a re-plot of experimental data (from Figure 5-7) for the 0.2D sample along with the corresponding parameters obtained from the multi-site exchange model used here. In general the figure shows good correspondence between them and reaffirms applicability of this model to such a system.

The magnetization exchange rates k_{LP} can be calculated using the exchange constants V1 obtained from the multi-Lorentzian model and the intrinsic powder

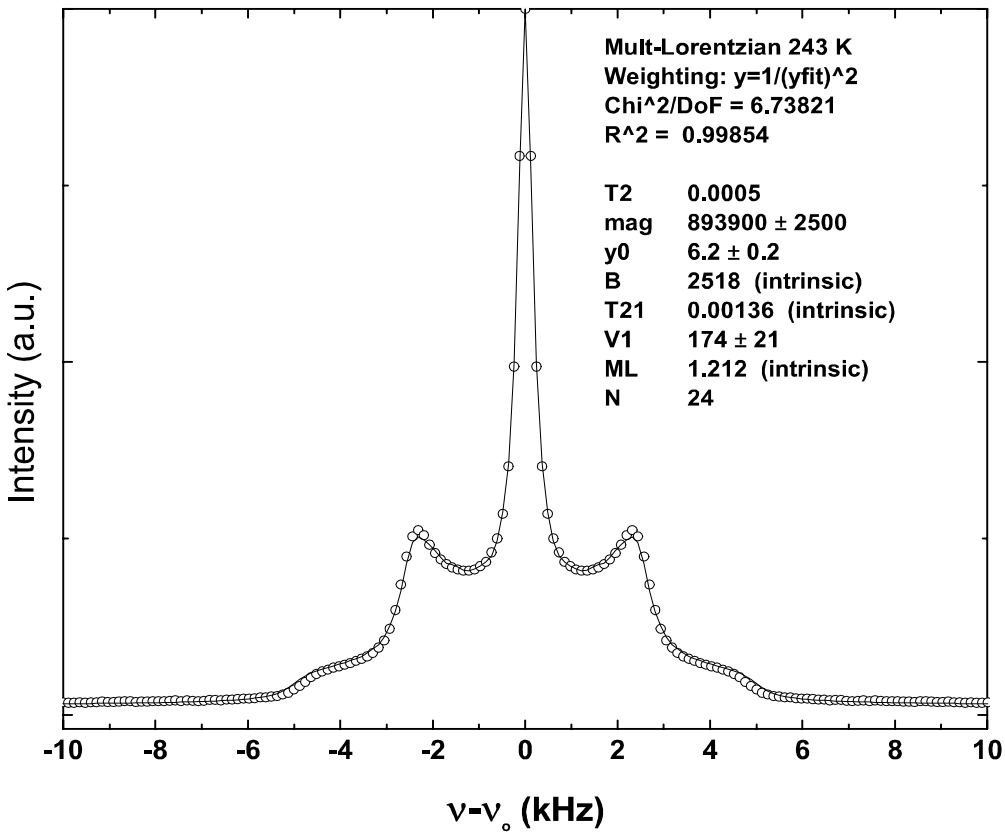

Figure 5-8: ^{2}H spectrum of the 0.D sample at 243 K. The solid line is the best simulation result using the multi-Lorentzian line model discussed in the text. Forty-eight Lorentzian lines were used for the powder pattern part (N=24) with equal T_2s (= 0.5 ms). Parameter mag is the scaling factor used in the final equation. B is half of the intrinsic powder pattern splitting, T21 is the intrinsic T_2 of the center Lorentzian line. V1 is the exchange rate constant between individual Lorentzian lines of the powder pattern and the central Lorentzian line. M1 is the intrinsic fraction of the central Lorentzian line.

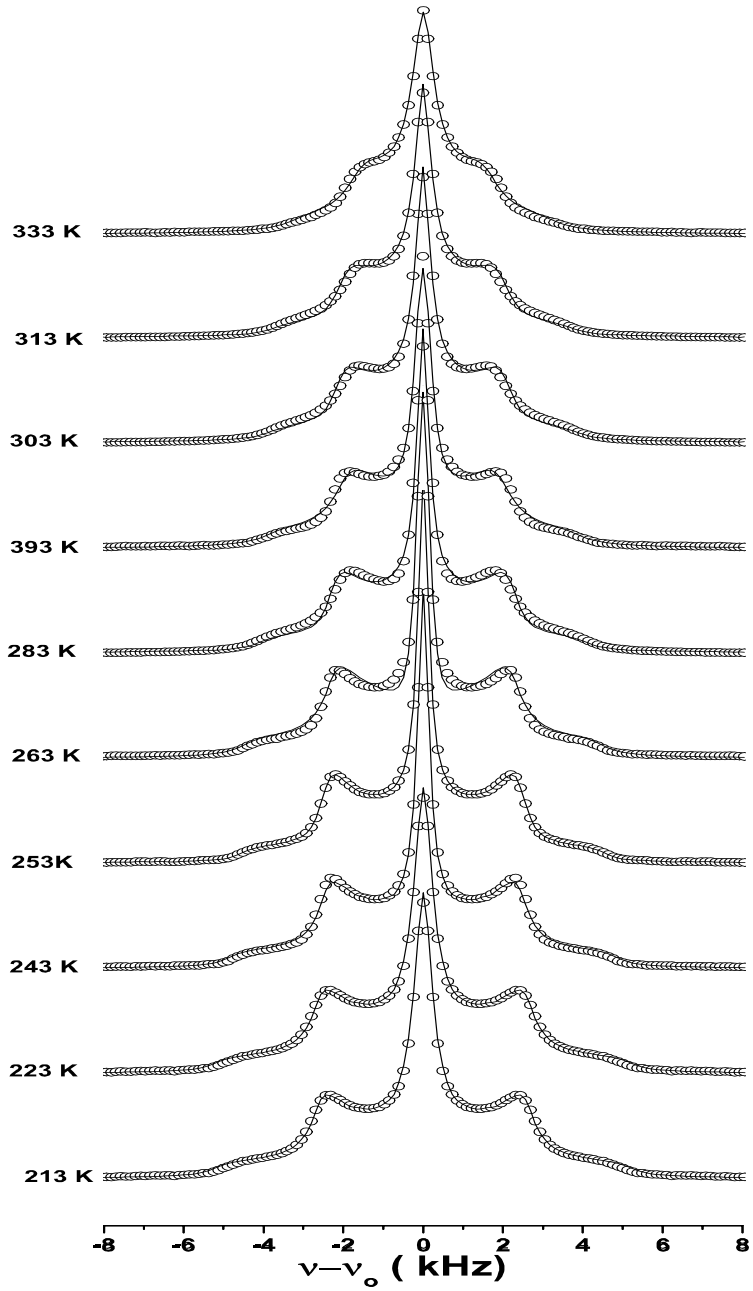

Figure 5-9: ^{2}H spectra versus temperature for the 0.2D sample (as in Figure 5-3). Solid lines are calculated using the multi-site exchange model with best-fit parameters.

pattern fraction M_P such that k_{LP}=V1 M_P as described in the detailed balance equation in section (2.5.1). These exchange rates are plotted versus temperature in Figure (5-11). These values are consistent with the reported values for similar low hydration sample in MCM-41 using double quantum and spin-lattice relaxation technique [9]. The solid line in the figure is the best fit to the exchange rates using the Arrhenius type equation that yields an activation energy for the exchange equal to 3.4± 0.1 kcal/mole with a pre-exponential factor of (4.4± 0.1)x 10^5 ms.

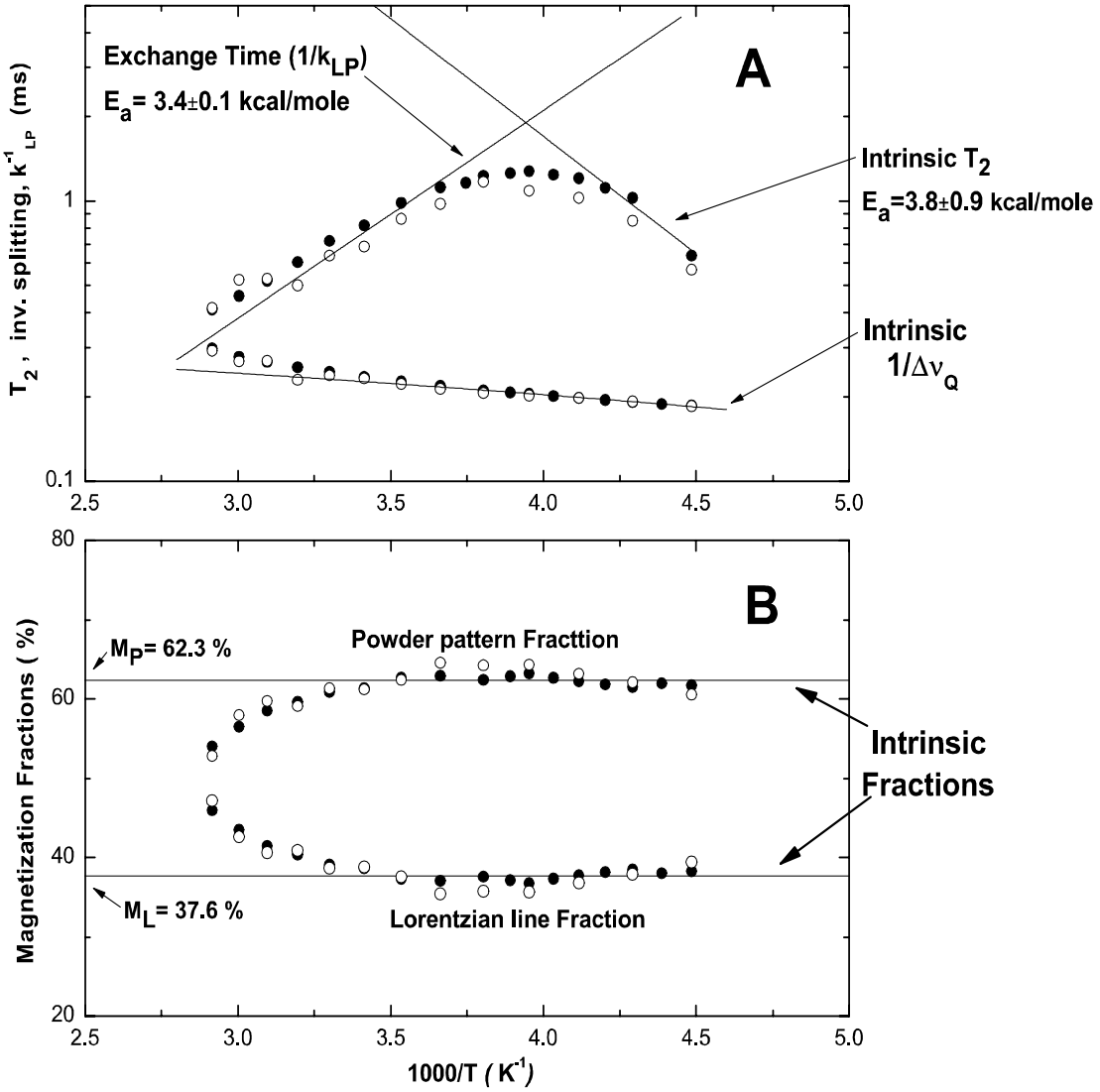

Figure 5-10: Experimental magnetization fractions, inverse of powder pattern splitting, and T_2s of the Lorentzian line along with the corresponding values obtained from the simulation, based on the multi-site exchange model. Solid circles represent experimental data while the open circles represent the values obtained from the simulation.

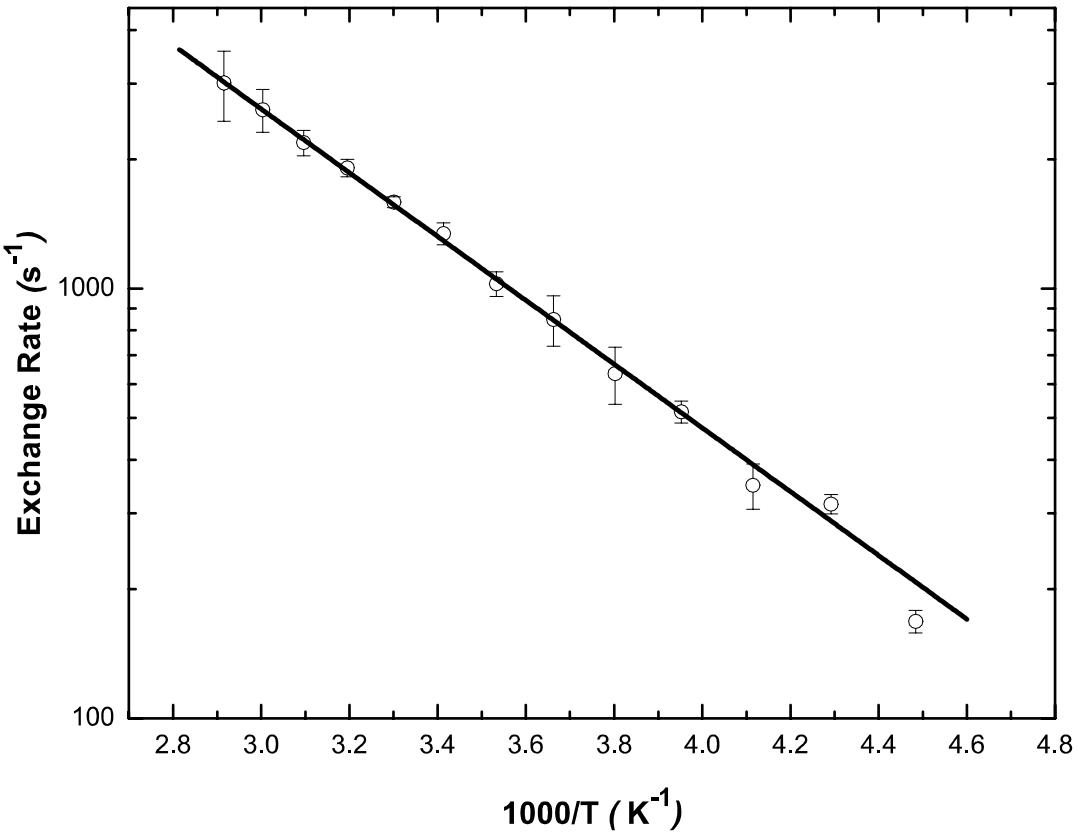

Figure 5-11: Rate of exchange of magnetization of water deuterons at the Lorentzian site to the water deuterons at the powder pattern site (k_{LP}) for the 0.2D sample. The value of k_{LP}=V1M_p is calculated at each temperature by using the powder pattern population (=2.0) and exchange rate constant V1 obtained from the ^{2}H simulation. The solid line is calculated using an Arrhenius type equation with activation energy E_a of 3.4 kcal/mole and a pre-exponential k_{LP0} of 4.4x 10^5 s^{-1}.

5.3 Hydration Sites: Identification and Water Molecule Dynamics

5.3.1 Identification of Hydration Sites

It is important to identify the hydration sites in order to gain insight into the kind of motions water molecules undergo to produce the observed ^{2}H spectra (e.g., Figure (5-3) on page 72). So far no definitive assignment of hydration sites has been published for MCM-41; which silanol group type is associated with the more liquid-like and Lorentzian signal and which group offers a more anisotropic environment to water so as to produce a powder pattern.

It is known from the literature [66] that the MCM-41 surface may contain geminal, single and H-bonded silanol groups. In addition, the hydroxyls of geminal groups may form hydrogen bonds. As the fraction of geminal sites is relatively small, it would appear reasonable to suggest that the two distinct ^{2}H NMR signals (Figure (5-3)) are associated with the single and H-bonded OH groups. Without additional information (discussed below) it is difficult to identify which specific silanol groups give rise to specific environments for the adsorbed water such as to produce the Pake doublet and the Lorentzian line Figure (5-3). Additional information about specific hydration sites can be obtained from ^{1}H- ^{29}Si CPMAS experiments. Such experiments report directly on the Si (of silanol) – H (of silanol OH) connectivities, and therefore provide a reliable way to identify silanol surface groups. Figure (5-12) shows the ^{1}H- ^{29}Si CPMAS spectrum of a 0.2H MCM-41 sample. The spectrum was well fitted to a sum of three Lorentzian lines with the peak positions and relative areas under the peaks listed in Table (5.3). It is seen

	Q^2			**Q^3**			**Q^4**	
Sample	δ (ppm)	A%	N_{OH}	δ (ppm)	A%	N_{OH}	δ (ppm)	A%
0.2H	-90	3	3	-100.8	76.8	97	-110.8	20.2

Table 5.3: Decomposition of ^{1}H- ^{29}Si CPMAS spectrum . The significance of the parameters is explained in the text.

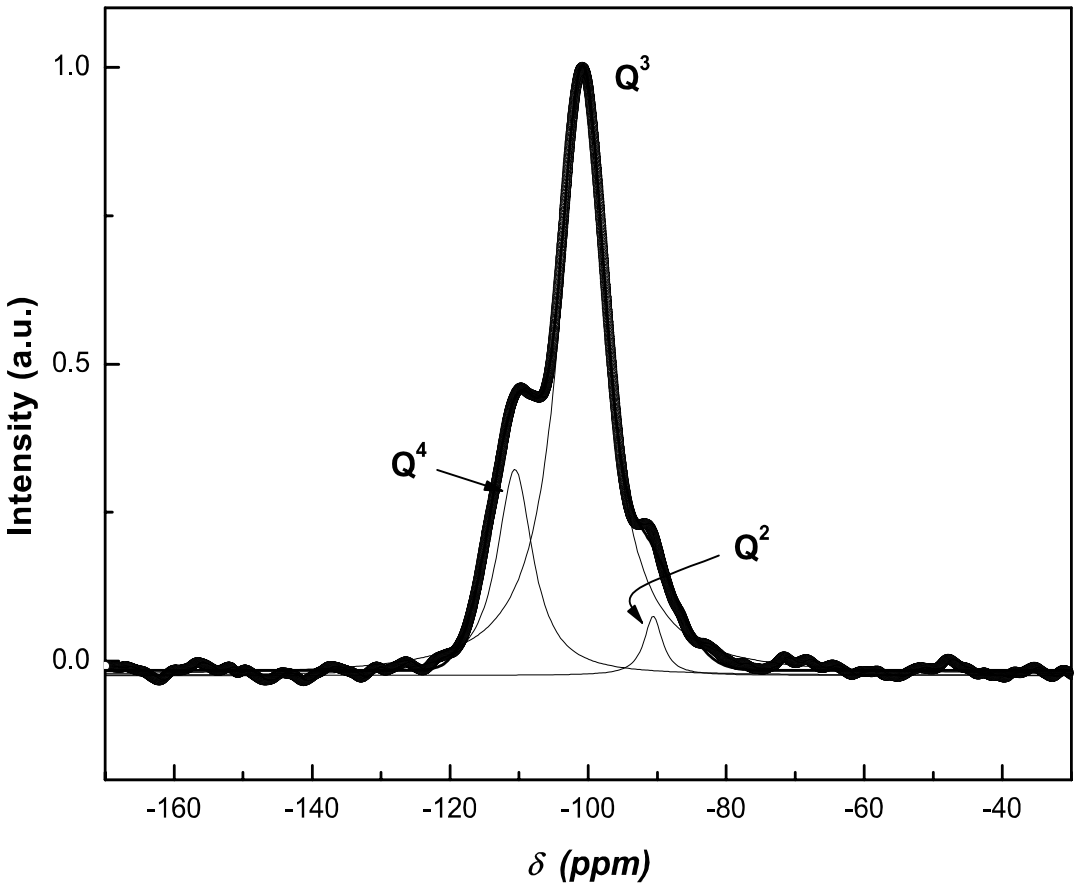

Figure 5-12: ^{1}H- ^{29}Si CPMAS spectrum of the 0.2H normal MCM-41 sample at room temperature. The spectrum was fitted to three Lorentzian lines with parameters given in Table (5.3). The sizes of the Q^2, Q^3 and Q^4 groups are 3%, 76.8% and 20.2%, respectively.

that the three resonances correspond well to the silanol groups Q^2, Q^3 and Q^4 (at δ = -90, -101 and -110 ppm, respectively) quoted in other studies of MCM-41 ([68] and [69]). The signal Q^2 (2 siloxane bonds) is assigned to silicon of geminal groups, Q^3 to silicon with one OH group (which may be H-bonded to another OH group or exist as a single OH group), and Q^4 to silicon without OH groups. As only the Q^2 and Q^3 signals monitor OH group types, the corresponding areas in Table (5.3) may be renormalized to sum to 100%. This shows that 3% of the sample's hydroxyls are associated with geminal groups. Although the single and hydrogen bonded silanols have clearly distinguished IR absorption lines ([70] and [71]), they both have δ= -101 ppm and are indistinguishable in this ^{1}H- ^{29}Si CPMAS experiment.

Since the water deuteron spectrum, Figure 5-3, is indicative of only two major hydration site types, and the geminal OH groups amount to only 3% of the sample OH population, we assume for simplicity that this group can be neglected when considering hydration details. It may be noted that the signal/noise ratio for the ^{1}H- ^{29}Si CPMAS experiment in the 0H400 sample was lower than for the fully hydroxylated case, making quantification difficult. The signal for the 0H800 sample was nearly non-existent, consistent with the removal of all OH groups.

Direct information about which hydration site gives rise to the powder pattern and which to the Lorentzian line in the water ^{2}H spectrum can be obtained by removing one of the types of hydration sites (the H-bonded OH groups) by heating MCM-41 to 400 ^{o}C, rehydrating it and then comparing the resulting ^{2}H spectrum in such a sample to that of Figure (5-3). Figure (5-13) shows the ^{2}H spectra for the 0.2D400 sample, with the NMR acquisition starting a) immediately after sample hydration (solid circles) and b) 5 days after sample hydration (open circles). The spectrum of case (a) exhibits similar features as that of the room temperature spectrum of Figure (5-3), except that the powder pattern is now only a small fraction of the signal. Fitting the spectrum to equation (2.38) on page (16) gives a line width of about 291 Hz and relative area of about 88% for the Lorentzian line, and a line splitting of about 3.25 kHz and relative area of about

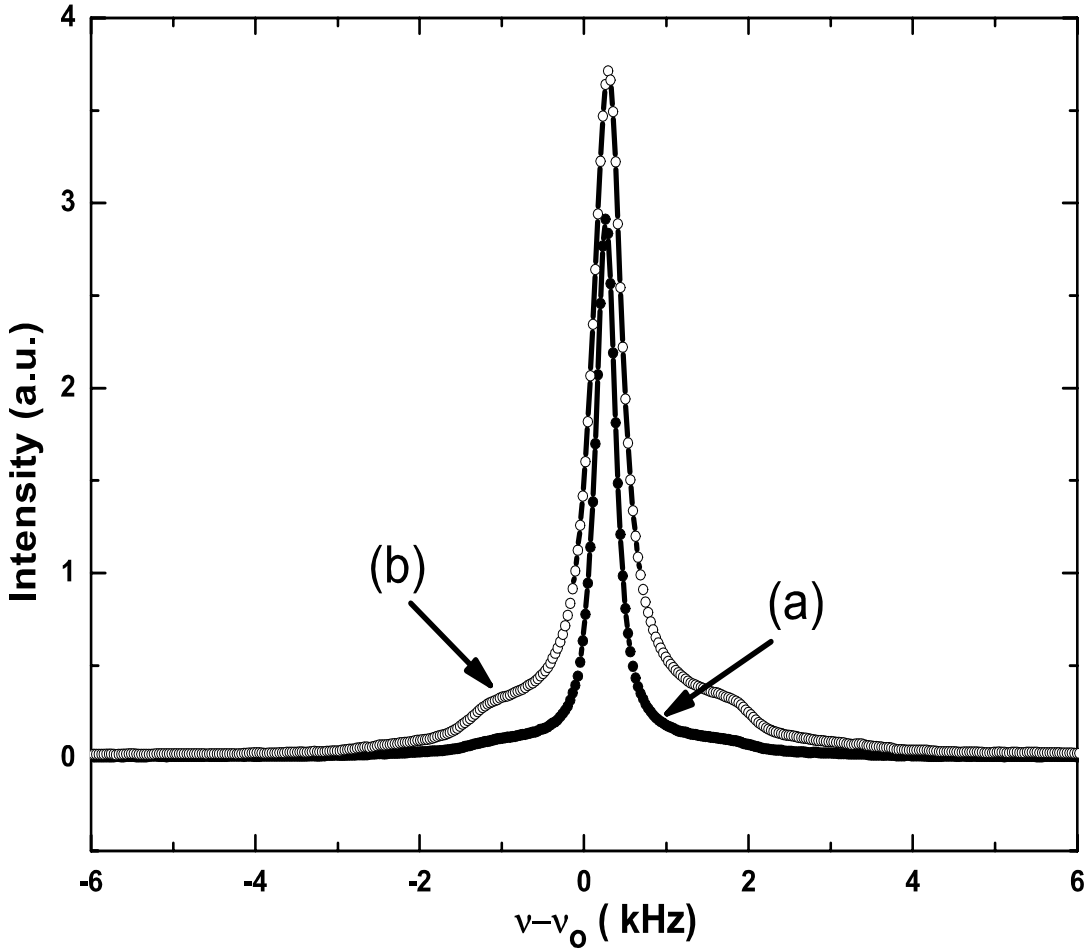

Figure 5-13: ^{2}H spectra of the 0.2D400 sample taken at room temperature. (a) Just after hydration of the sample (solid circles), and (b) 5 days after hydration of the sample (open circles). In (a) the solid line was calculated from equations described in section (2.2) with the relative areas, width, and splitting parameters given in the text.

12% for the powder pattern. As MCM-41, heated to 400 ^{o}C, contains essentially only single OD groups and most of the water deuteron signal in the 0.2D400 sample, case (a), is a Lorentzian, strongly suggests that this signal component is associated with water hydrating the single OD groups. The small powder pattern component is expected to arise from water molecules residing on H-bonded OD groups that reformed due to the presence of the water during the hydration process [71]. After 5 days considerable rehydroxylation and reformation of H-bonded silanol groups is expected ([70], [71]). Thus, after 5 days some of the hydration water in the 0.2D400 sample has been used to reform H-bonded OD groups, and the remaining water in the sample has redistributed among these newly-formed OD groups and the single OD groups. This is clearly reflected in the considerable growth of the powder pattern component in case (b), Figure (5-13).

To substantiate the above suggestion that the regrowth of the powder pattern is the result of water molecules hydrating the H-bonded hydroxyls that have reformed through the vapour phase, a set of proton MAS experiments were performed in MCM-41. Figure (5-14) shows a ^{1}H MAS spectrum of the 0H sample. The spectrum shows two distinct peaks; one at 1.8 ppm that was assigned to the single silanol groups [99] and a broad line, extending to about 7 or 8 ppm, assigned to H-bonded silanol groups (see Table 5.4). The areas under the curves

Sample	$\boldsymbol{\delta_{sh}}$(ppm)	$\mathbf{M_{sh}}$(%)	$\boldsymbol{\delta_{bro}}$(ppm)	$\mathbf{M_{bro}}$(%)
0H normal	1.80	34	4.27	66
0H400	1.71	100	–	0
0H400-7h	1.79	86	3.16	14
0H400-16h	1.77	55	3.40	45

Table 5.4: .
Parameters obtained from fitting the spectra of different samples to two Lorentzian lines. The subscript ' sh' and 'bro' refer to the sharp and the broad Lorentzian fitted components. M is the component fraction.

for the single and H-bonded silanols are 34 and 66%, respectively. Figure (5-15) shows the ^{1}H MAS spectrum of the 0H400 sample. This graph only shows

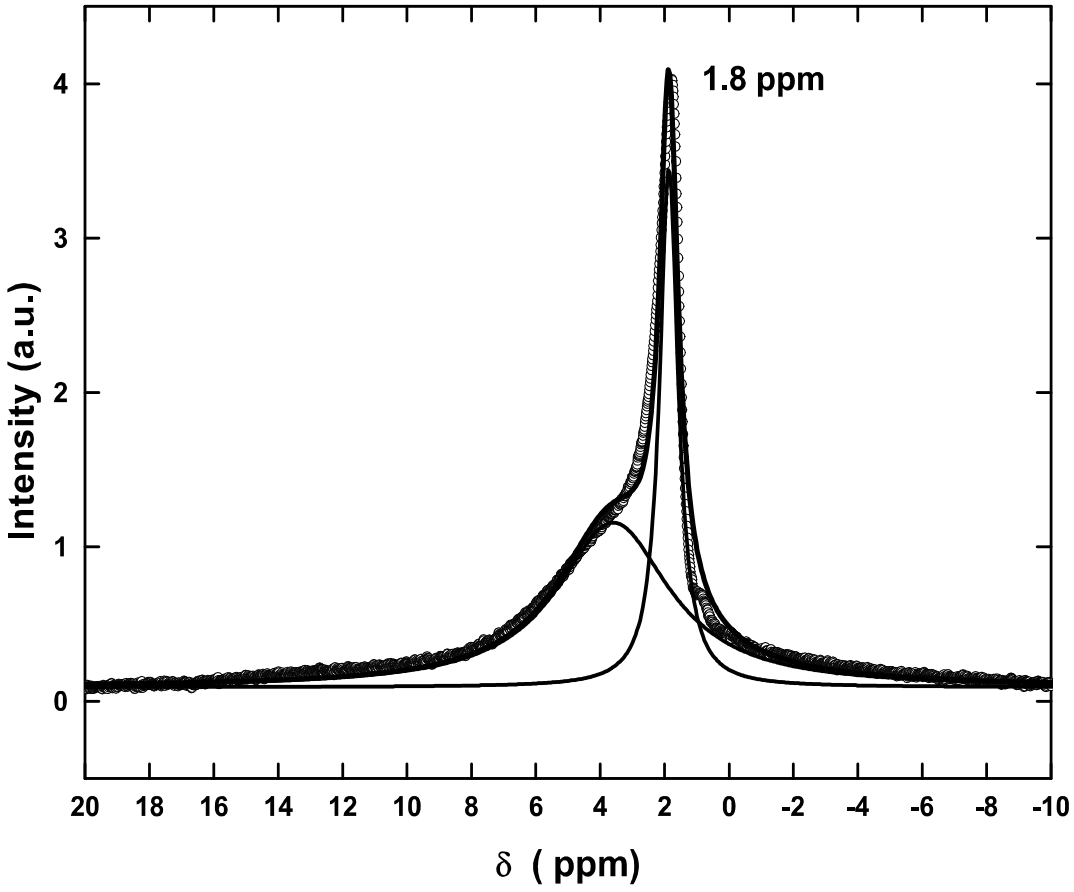

Figure 5-14: ^{1}H MAS spectrum of the dry sample, 0H, of normal MCM-41 at room temperature and at 10 kHz spinning rate. Two Lorentzian lines are fitted to the spectrum. The sharp line has a chemical shift of 1.8 ppm with 34% of the total signal. This component was assigned to the single silanols. The broad band with chemical shift centered at 4.2 ppm and amounting to 66 % of the total signal, was assigned mostly to the H-bonded silanol groups.

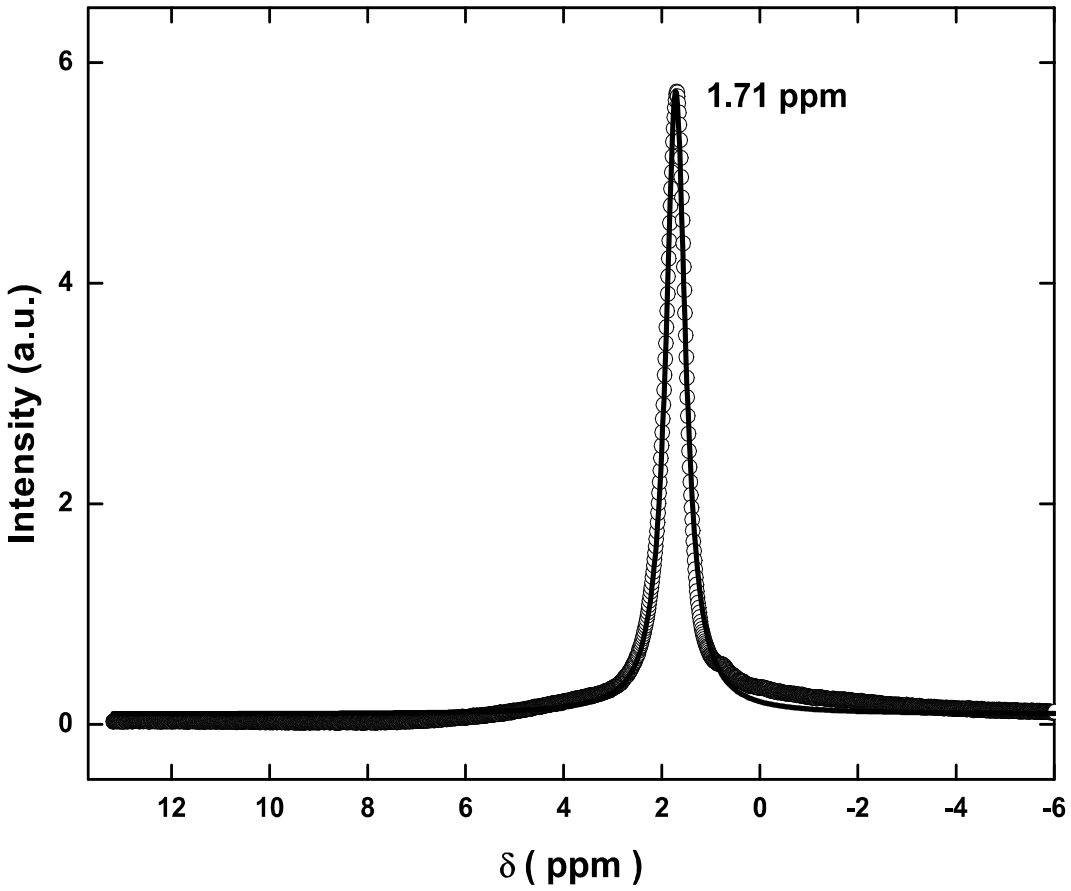

Figure 5-15: ^{1}H MAS spectrum of the dry sample, 0H400, at a spinning rate of 10 kHz. As expected heating to the high temperature removed H-bonded silanol groups. Thus, the broad line appearing Figure (5-14) is not seen here. Only the sharp peak remains. The solid line represents the best fit of a Lorentzian line to the data (see Table 4.2).

one peak at 1.7 ppm, as expected. Previous IR studies ([70][71][79]) indicate that heating MCM-41 to 400 ^{o}C removes H-bonded silanol groups. The present experiment is consistent with such observation as the broad peak appearing in Figure (5-14), that has been assigned to H-bonded silanols, is absent in Figure (5-15).

To study the rehydroxylation of the previously dehydroxylated H-bonded OH groups, spectra were measured in the 0H400 sample that had been hydrated for 7 hours (B) and 16 hours (C) through the vapour phase and then dried under vacuum. The corresponding samples are labelled 0H400-7h and 0H400-16h. Figure (5-16) shows these spectra (B) and (C), as well as spectrum (A) taken from Figure (5-15). In spectra B and C the recovery of the signal assigned to the H-bonded OH protons and the decrease of the signal of the single OH group protons is observed. This confirms the conversion of single silanols into H-bonded groups in the presence of water vapor. The signal from H-bonded OH protons recovered to 14% and 45% of the total population in samples 0H400-7h and 0H400-16h, respectively. The parameters for H-bonded protons obtained from the ^{1}H MAS experiments for the various samples are plotted versus hydration time in Figure (5-17). The solid line represents a fit to the data of $f_{H-bond} = f_{H-bond(max)}$ (1-exp(-t/C)) where $f_{H-bond(max)}$ is the maximum fraction of H-bonded OH groups, and C is a time constant for the formation of the H-bonded hydroxyl groups. Here C=17$\pm$3 hours.

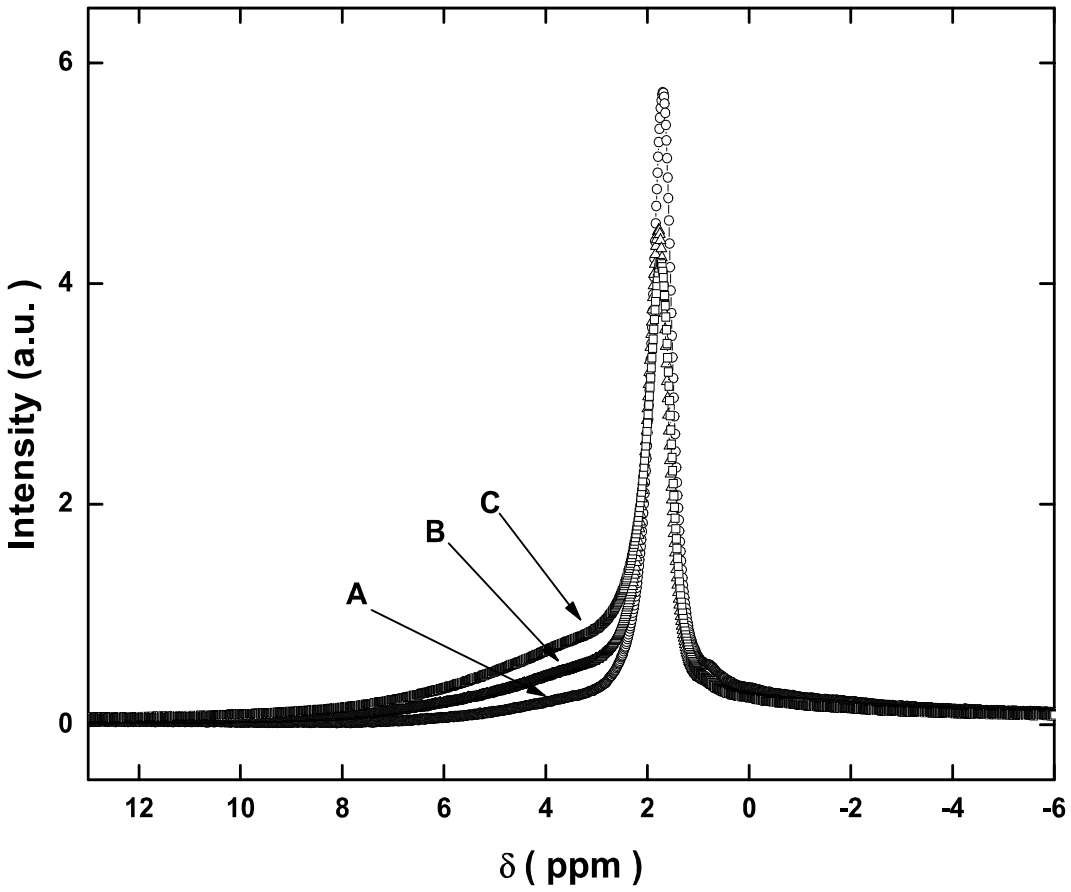

Figure 5-16: ^{1}H MAS spectra for samples 0H400 (A), 0H400-7h (B), and 0H400-16h (C) at room temperature and 10 kHz spinning rate. The parameters obtained from the fit of two Lorentzians to each of the spectra are summarized in Table (5.4).

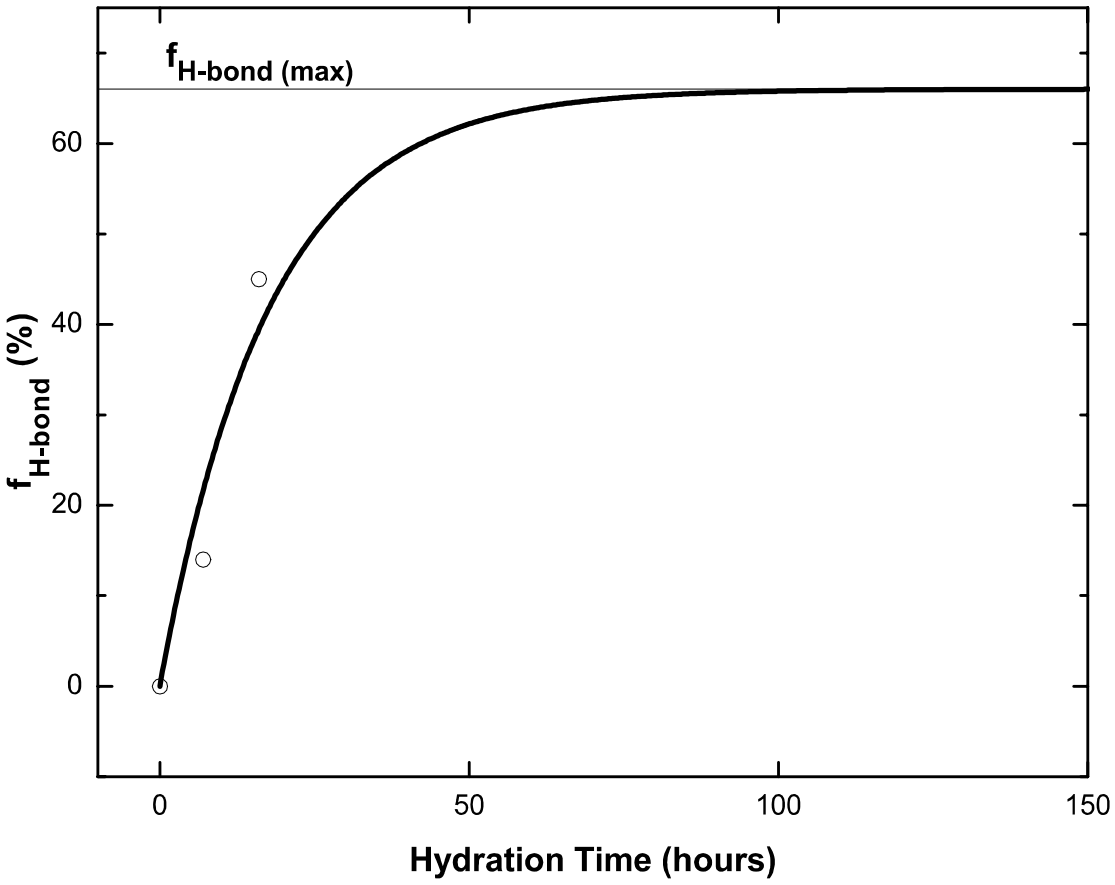

Figure 5-17: Fractions of protons on H-bonded OH groups plotted versus hydration time for 0.2H sample. The maximum value of 66 % is taken from Figure (5-14). Assuming exponential behaviour, the time constant for the rehydroxylation of H-bonded OH groups through the vapor phase equals approximately 17 hours.

5.3.2 Water Molecule Dynamics at Hydration Sites

Water molecules that are hydrogen bonded to the single silanol groups are expected to be more mobile than those bonded to H-bonded silanols. In the former case, the rotation of a water molecule about the hydroxyl group OD bond and of motion of the silanol group itself (rotation of the OD bond about the Si-O bond) is expected to contribute to the dynamics. The mobility of surface silanols has been reported in the literature for the MCM-41 pore surface [90] and similar surfaces [104]. In addition, water molecules may exhibit a wobbling motion [9] around the OD bond. These motions combine to average the quadrupolar Hamiltonian (equation (2.27) on page 13) to a considerable degree. As a result a Lorentzian line of FWHM of around 400 Hz is seen for the water deuterons at the single silanol groups at room temperature (Figure (5-3)).

The deuterons of water bound to H-bonded silanol groups produce the powder pattern in the ^{2}H spectra (see Figure 5-3). The motion of these silanols is restricted because of the presence of hydrogen bonds between them and likely each water molecule at these sites takes part in additional hydrogen bonds to other water molecules or to H-bonded OD groups. Therefore, the motion of water molecules bound to these groups is less effective in averaging out the quadrupolar Hamiltonian. In this case, a reduction in the splitting from approximately 160 kHz [9] to about 5.4 kHz (at 223 K) is observed (Figure 5-3). One half of this reduction can be realized for the dynamic model involving rapid (compared with the quadrupolar splitting) molecular rotation about one axis. For example, a possible water molecule coordination at the H-bonded hydration sites might be as depicted in Figure (5-18). Here the water molecule is undergoing rapid rotation about the hydrogen bond axis (Figure 5-18). Using equation (2.42) on page (20) for this case gives $\Delta\nu_Q = \Delta\nu_Q(RL)[(3\cos^2\beta - 1)/2] = (3/4)213[(3\cos^2(52.5^o) - 1)/2]$ =8.9 kHz. It may be noted that for $\Delta\nu_Q$ =5.4 kHz the angle β =53.37^o. Considering the geometric arrangement of the water molecule's near tetrahedral orbitals, it stands to reason that β is greater than 52.5^o. In addition, wobbling motion could

reduce the splitting somewhat so that a value of 5.4 kHz is quite reasonable. A wobbling motion for water molecules at the O-^{2}H group was also suggested in [9].

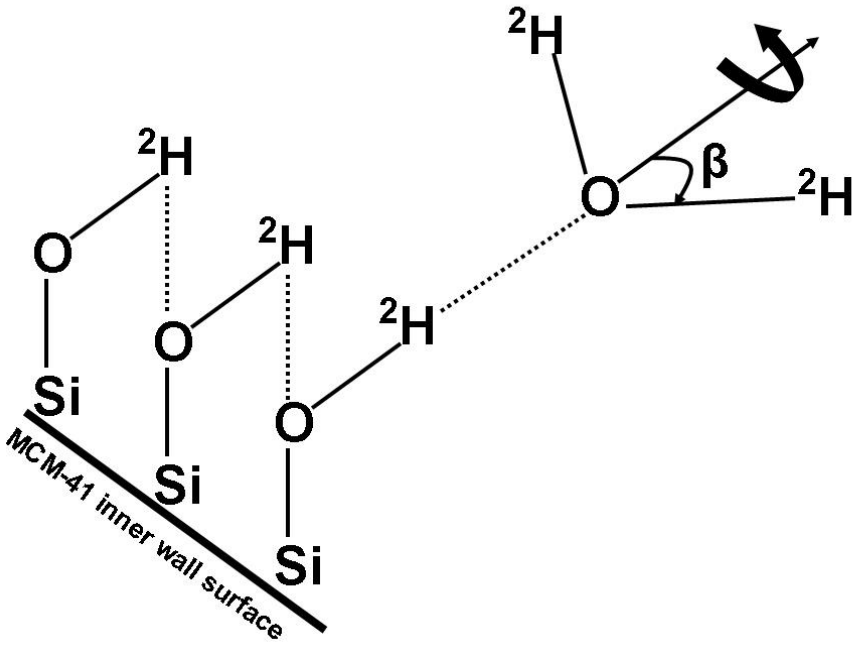

Figure 5-18: A simple model for water molecule dynamics at a H-bonded silanol group. The dotted lines are hydrogen bonds. The rotation frequency of the water molecule, around the O–^{2}H bond is assumed to be much faster than the rigid-lattice quadrupolar splitting.

5.4 2D ^{2}H Spectral Measurements

In addition to using 1D ^{2}H spectra to investigate the magnetization exchange between water deuterons in the low hydration (0.2D) sample, 2D ^{2}H spectroscopy was used to shed additional light on such exchange. 2D data were collected at different temperatures using a pulse sequence consisting of four 90^o pulses as described in section (2.6). Figure (5-19) shows 2D contour maps at different mixing times at 233 K and Figure (5-20) shows 2D spectra as surface plots, for two different mixing times, also at 233 K. Each spectrum exhibits a diagonal powder pattern and a Lorentzian line, similar to the 1D spectrum, as well as cross peaks. Two different kinds of cross peaks are seen. One (at about -30, +30 ppm and +30, -30 ppm, Figure 5-19 A) is seen in the spectrum at all mixing times including the shortest mixing time of 5 μs (Figure 5-19). However, the exchange time determined from 1D data was much longer than 1 ms at this temperature, so that the cross peaks at these positions are not due to exchange. These peaks could be due to double quantum coherences or produced by the dual Fourier transformation of the time domain signal of the spin 1 nucleus [32][34]. The former possibility is considered first. It should be noted that such 2D contour maps, measured by us in a separately prepared 0.2D sample, were indistinguishable from those shown in Figure (5-19).

Double quantum coherences (signals) [110] can be produced by using a three- or four 90^o-pulse sequence as was used for the 2D spectra recorded here. These cross peaks typically decay faster than cross peaks produced by exchange. Double quantum coherence cross peaks decay on the T_2 time scale whereas exchange cross peaks initially evolve on the exchange time scale and finally decay on the T_1 time scale [34]. In order to test for the presence and importance of double quantum coherences, double quantum spectra were collected for different evolution times (Figure 5-21). It can be seen, that the signal starts to decay at about 500 μs. This result is consist with that found in a similar study on MCM-41 using double quantum NMR techniques [9]. The present data indicate that dou-

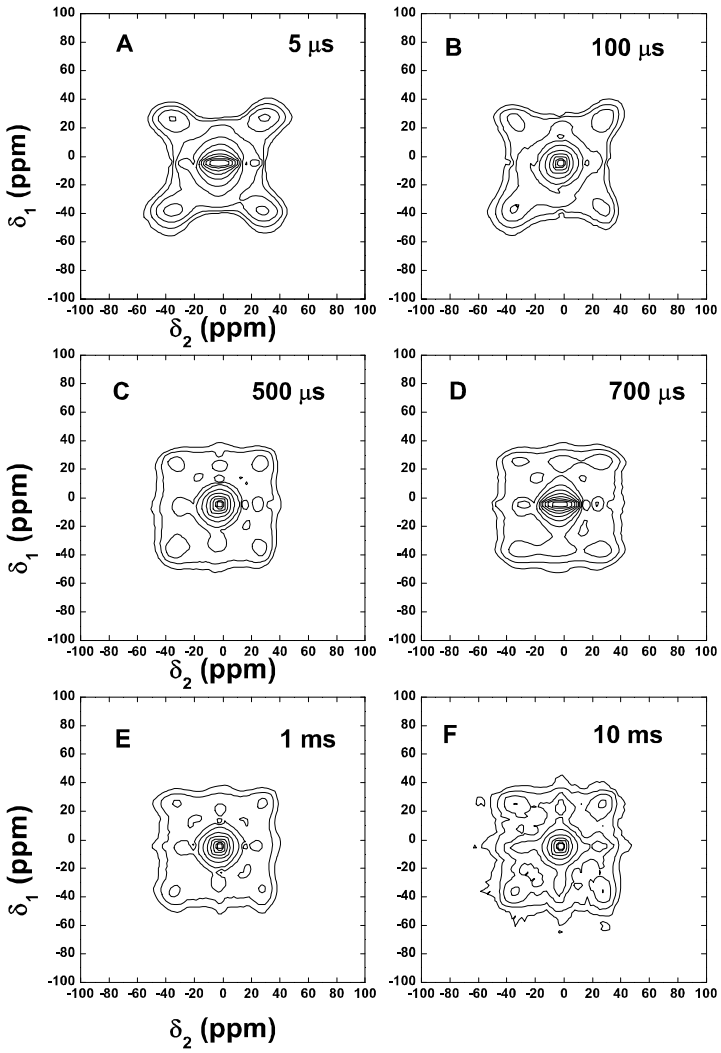

Figure 5-19: 2D contour maps for the 0.2D sample at 233 K at different mixing times (indicated within each contour). The pulse sequence consists of four 90^o pulses as described in section (2.6). The cross peaks appearing in A are not due to exchange but rather to artifacts produced by the Fourier transformation of the time domain signal and double-quantum coherences.

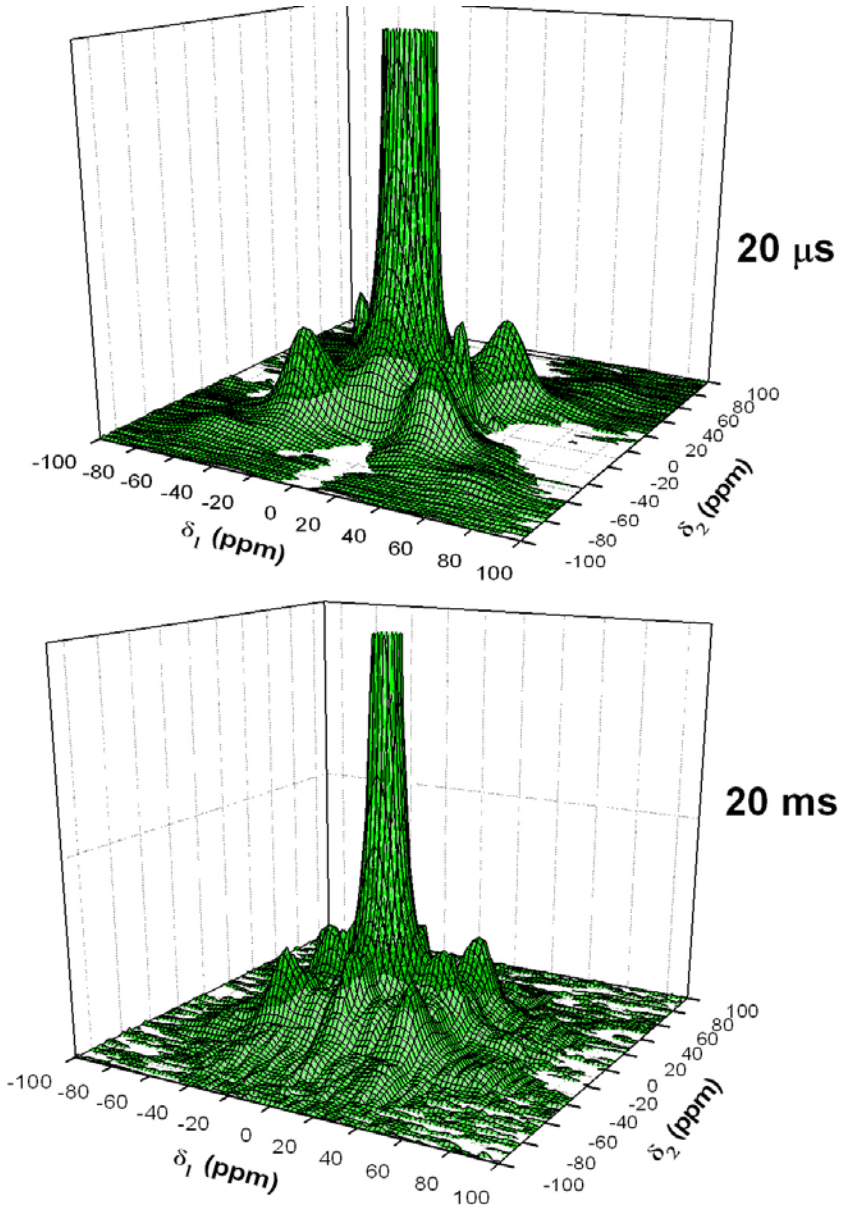

Figure 5-20: 2D surface plots of spectra for the 0.2D sample at 233 K at mixing times of 20 μs and 20 ms as indicated on the right side of each spectrum. A pulse sequence of four 90^o pulses as described in section (2.6) was used.

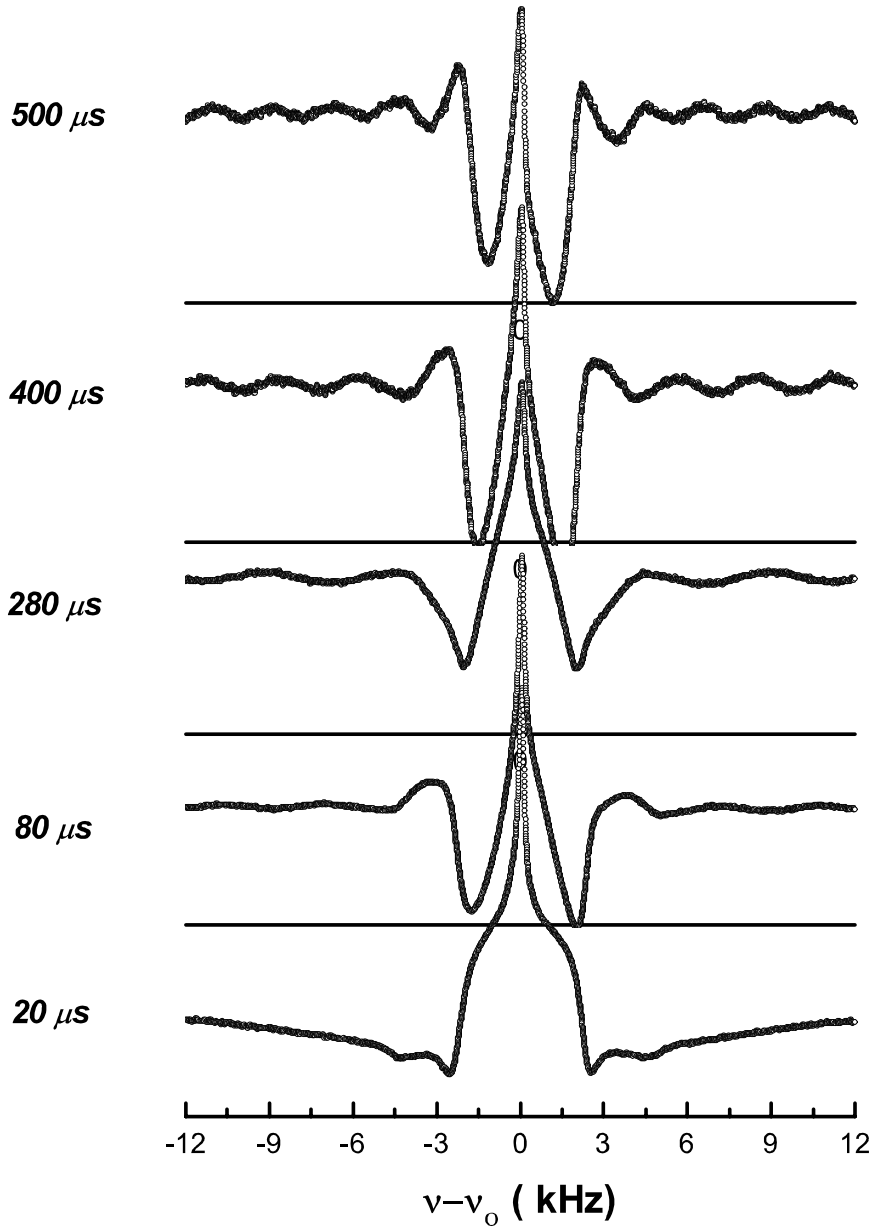

Figure 5-21: Double Quantum spectra at different evolution times for the 0.2D sample at room temperature. Evolution times are indicated on the left side of each spectrum.

ble quantum coherences contribute to some extent to the cross peaks, in the 2D spectra especially between mixing times from zero to 500 μs. Beyond this mixing time the cross peaks persist, and must originate from artifacts produced by the Fourier transformation of the time domain signal for spin 1 case that gives a powder pattern. The quadrupolar Hamiltonian for spins giving the Lorentzian line shape is largely averaged out and no cross peaks are generated. This means that the cross peaks in the 2D spectra (Figures 5-19, 5-20) for very small mixing times (till about 500 μs) are due to the Fourier transformation of the dual frequency of the spin 1 nucleus (in particular for the powder pattern part) and quantum coherence contributions, while at later times the former effect persists.

To obtain a pure absorption spectrum for the powder pattern in this case it is necessary to use dual pulse sequences as described in detail in reference [34] and as presented in section (2.6). These sequences are called Cos Cos and Sin Sin pulse sequences. Thus, for every mixing time two 2D data sets are needed. The 2D absorption spectrum for a specific mixing time is produced by subtracting the Sin Sin spectrum from the Cos Cos spectrum. Figure (5-22) shows such spectra measured at room temperature for the 0.2D sample. Ignoring the center line for the small mixing time (first 2 graphs in the first row) it seems that subtracting Sin Sin part from Cos Cos part produces an absorption 2D spectrum without cross peaks due to the Fourier transformation artifact. At first glance, especially for low mixing time it appears that the Cos Cos spectra are similar to the normal 2D spectra given in Figure (5-19) and Sin Sin is consistent with the cross peaks due the Fourier transformation. For higher mixing times (second and third row graphs of the same figure) complicated spectra arise containing both artifacts and exchange effects. The spectra obtained from the subtraction of the Sin Sin spectrum from the Cos Cos spectrum yields the absorption spectrum for the powder pattern but not for the central Lorentzian lines. A different set of sequences would have to be developed in order to also obtain the pure absorption spectra for the complete 2D exchange scenario. An important point connected with our data is that the two kinds of cross peaks are separated and one can

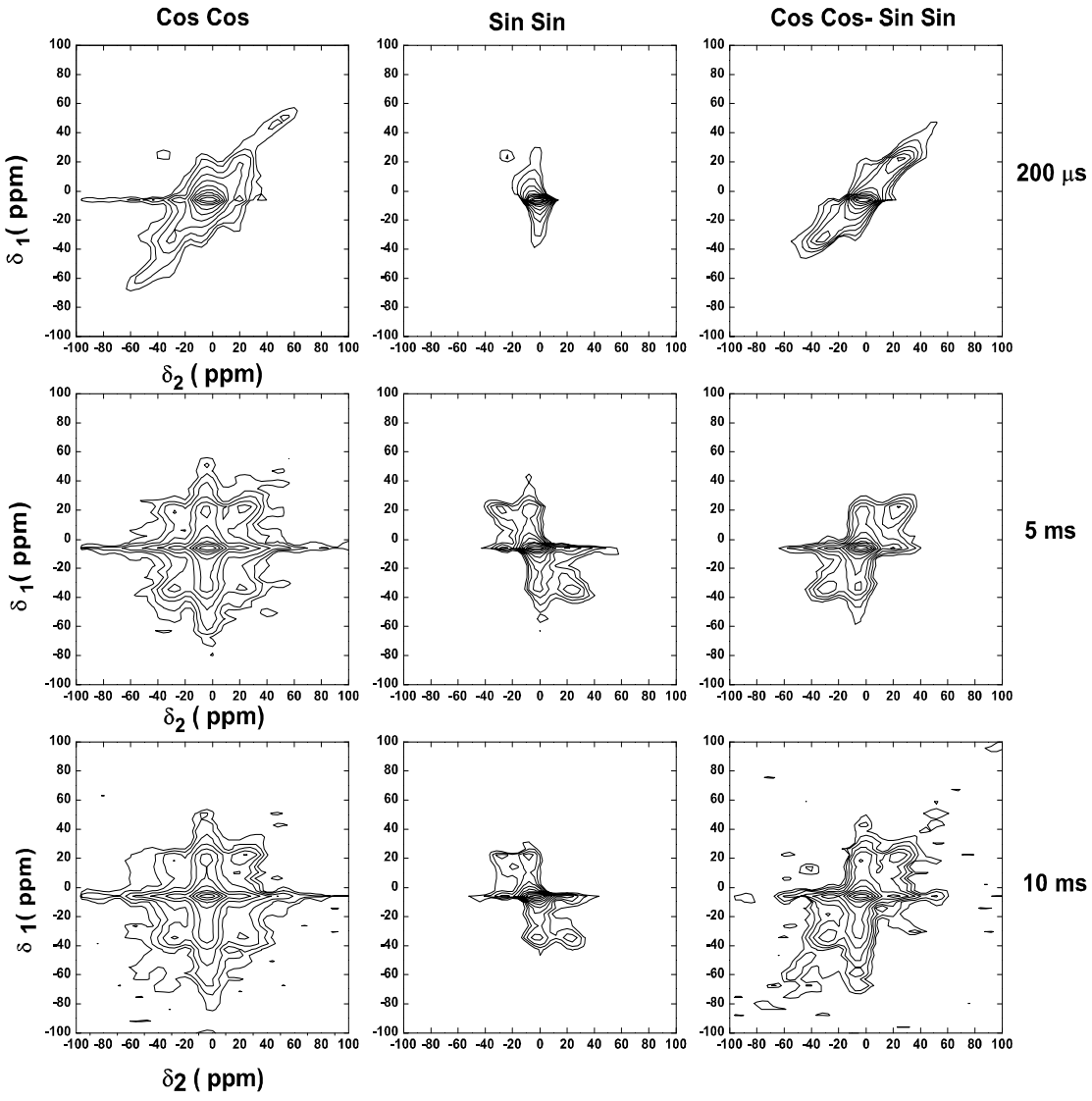

Figure 5-22: Experimental 2D contour maps at room temperature for Cos Cos (left part), Sin Sin (middle part) along with their differences (right part). Mixing times are indicated to the right of each row. The pulse sequences are described in section (2.6).

easily see the development of the real exchange cross peaks with higher mixing times from the figures (5-19, 5-20 and 5-22).

An attempt to simulate the data was made by ignoring the presence of the pseudo-cross peaks, and using the same multi-site approach as used for the 1D case except that the 2D equations described in section (2.6) were used. 48 Lorentzian lines were used to simulate the powder pattern and one line for the central Lorentzian line. For the calculations the chemical shift scale was used instead of the frequency scale. Most of the parameters used in the simulation are obtained from our 1D results. The exchange constant is set to 0.7 ms^{-1} (as obtained from the 1D exchange analysis at room temperature). No exchange was introduced between powder pattern sites. Origin software was used and the program is included in reference [30]. The simulated 2D contour maps along with the differences Cos Cos-Sin Sin (left part) of the experimental spectra are shown in Figure (5-23). The figure shows contour maps for a few different mixing times, indicated with each graph. From the simulation it is seen that the cross peaks due to magnetization exchange between the water deuterons with the powder pattern and the Lorentzian lineshapes develop with higher mixing times, as the spin groups have more time to exchange magnetization. At a very small mixing time (200 μs), no cross peaks are observed because this time is too short for noticeable exchange effects to develop. Any comparison with the experimental 2D contour maps should be done while ignoring the cross peaks due to double quantum coherences and Fourier transformation of time domain data for spin 1 nuclei.

Although qualitative comparison is possible, no quantitative comparison between experimental and simulated spectra (Figure 5-23) can be made. In particular, as the mixing time increases cross-peaks are seen to develop in both experimental and simulated spectra and these exhibit qualitatively similar peak intensity time progression as mixing time and temperature are varied.

The present 2D exchange spectroscopy experiments, although not adding quantitative information, are qualitatively consistent with the 1D exchange analy-

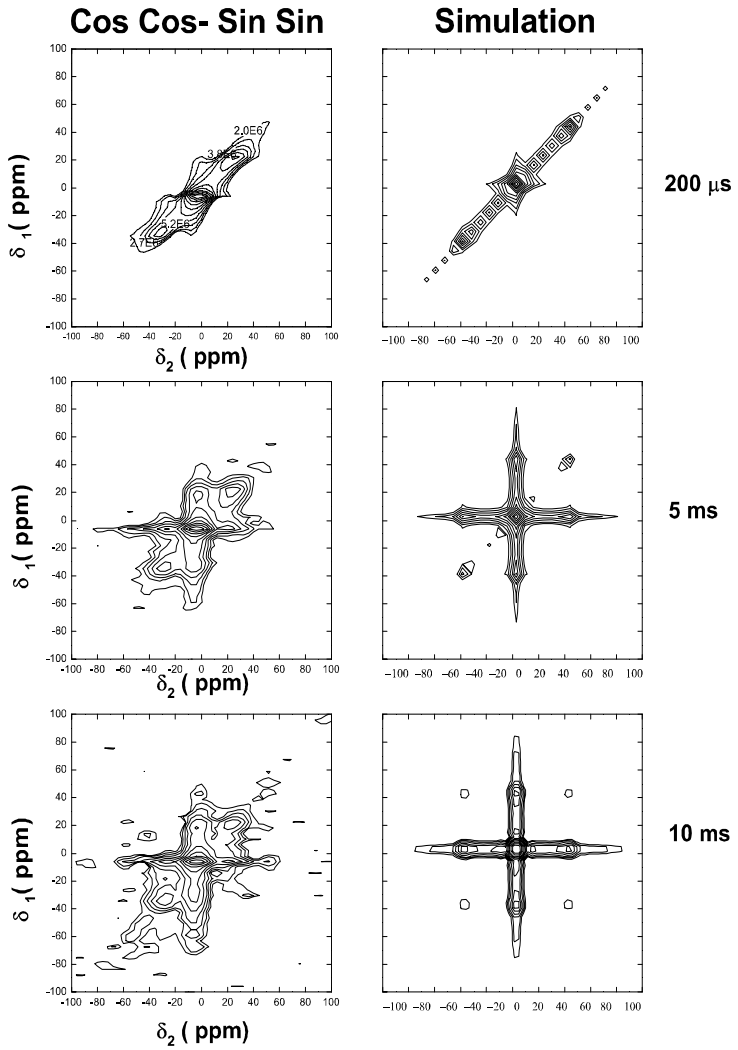

Figure 5-23: Simulated 2D contour maps at different mixing times along with corresponding experimental absorption maps. At a very small mixing time the cross-peaks are not seen, but at higher values of mixing time these become noticeable.

sis presented in section (5.2.3). These experiments thus add support to the two-site (H-bonded hydroxyl and single hydroxyl sites) water molecule exchange model. In addition, the above 2D experiments point to the need, in the present application, for the development of different pulse sequences than those typically used in ^{2}H exchange experiments. Such development has the makings of an interesting theoretical research project.

Chapter 6

Conclusions and Recommendations

In dry MCM-41 only one magnetization component exhibiting a Gaussian line shape with FWHM of about 30 kHz, was observed. This magnetization component arises from MCM-41 surface silanol groups (Si-O-^{2}H). In MCM-41 hydrated to a 0.2 monolayer level with D_2O, in addition to the surface silanol deuterons, two other magnetization components are distinguished. These are assigned to deuterons at two different water hydration sites with different water molecule motion environments. A fraction (61%) of the water deuterons undergo anisotropic motion that produces a powder pattern with splitting of about 4.2 kHz and the other fraction (39%) of water deuterons undergo more rapid and less anisotropic motion that gives rise to a Lorentzian line with FWHM of about 400 Hz at room temperature. The observed ^{2}H line shapes could not be modelled correctly using exchange motion scenarios for a single spin group. Instead, magnetization exchange occurs between these two groups. Classic two-site magnetization exchange models can not be used to describe this exchange as such models describe exchange between two Lorentzian lines while the magnetization exchange in our sample is between spins with Lorentzian line and spins with a powder pattern line shape. A multi-site exchange model was applied to quantify

this exchange. The magnetization exchange rate obtained from such exchange analysis of the 1D ^{2}H spectra obeys the Arrhenius law over the temperature range 223 to 333 K. The rate of magnetization exchange from water deuterons with Lorentzian line shape to water deuterons with powder line shape has an activation energy of 3.4 kcal/mole and is about 1.3 ms^{-1} at room temperature.

Two dimensional $^{\mathbf{2}}$H data of $D_{\mathbf{2}}O$ in MCM-41 hydrated to the 0.2 monolayer level, shows the development of cross peaks that represent the exchange between the water molecules at the two sites (spins with Lorentzian and powder pattern line shapes). A 2D ^{2}H simulation was performed based on a multi-site exchange model that qualitatively accounts for the observed exchange. Although no quantitative result could be extracted from the 2D ^{2}H spectra obtained in this study, a qualitative comparison between the experimental and simulated 2D contour maps supports the use of the multi-site magnetization exchange approach.

One of the main findings of this research is connected with hydration site identification. Using ^{1}H-^{29}Si CPMAS, ^{1}H MAS and ^{2}H spectral measurements, it is proven that water deuterons exhibiting a powder pattern are bound to the H-bonded silanol groups and undergo anisotropic motion. Water molecules bound to the single silanols have more motional freedom, undergo less anisotropic motion and the deuterons involved give rise to a Lorentzian line. A simple, two-correlation time anisotropic motion model involving fast rotation of the water molecule, at a H-bonded silanol group, about the water molecule-hydroxyl group hydrogen bond approximately satisfies the observed quadrupolar splitting.

Heating MCM-41 powder to a temperature of 400 °C removes the H-bonded silanol groups. Re-hydroxylation experiments have shown that the time constant for re-formation of these groups is about 17 hours.

Recommendations for further work

The following points need further investigation and are suggested topics for future research:

- ^{2}H spectra taken in samples with hydration levels > 0.2 monolayer (given in Appendix A) as part of this study show interesting features with temperature. These data need to be fully analysed for exchange to ascertain the importance of contributions from exchange and from possible water phase changes.

- The 2D ^{2}H exchange data point to the need for the development of different techniques (e.g., pulse sequences) that permit the acquisition of a proper 2D absorption spectrum for the present case involving magnetization exchange between a Lorentzian line and a powder pattern.

- It would be very useful to perform a similar study as presented here in different pore sizes of MCM-41. As the importance of the surface is effectively changed as the pore size is varied, such a study would yield direct information about the significance of surface relaxation.

- A study of the temperature dependence of water deuteron spin-lattice relaxation times in MCM-41 samples with different hydration levels should be performed in order to obtain information about water molecule dynamics with short correlation times.

Appendix A

Appendix: **Data not elaborated upon in the main text**

Samples hydrated to a higher level than 0.2 monolayer (referred to as 'high hydration' samples) were investigated to gain additional insight into the dynamics of water molecules in MCM-41. ^{2}H spectra at different temperatures (213 K to 243 K) were acquired for 0.6D, 1.6D and FullD samples. Here we show their ^{2}H spectra versus temperature. At the higher hydration levels of 0.6 and 1.6 monolayers, the deuterons exhibit a Lorentzian line except at temperatures below 243 K. In the fully hydrated sample only Lorentzian lines are observed. Such single Lorentzian line behaviour of the water deuteron resonance at these high hydration levels has been attributed to rapid exchange between a surface component with powder pattern line shape and a component where water molecules are able to undergo more isotropic motion so as to produce only a single Lorentzian line that was observed over the temperature range 223 to 333 K.

These results need to be analysed in detail in order to obtain additional information about exchange and the behaviour of water in MCM-41 at higher hydration level.

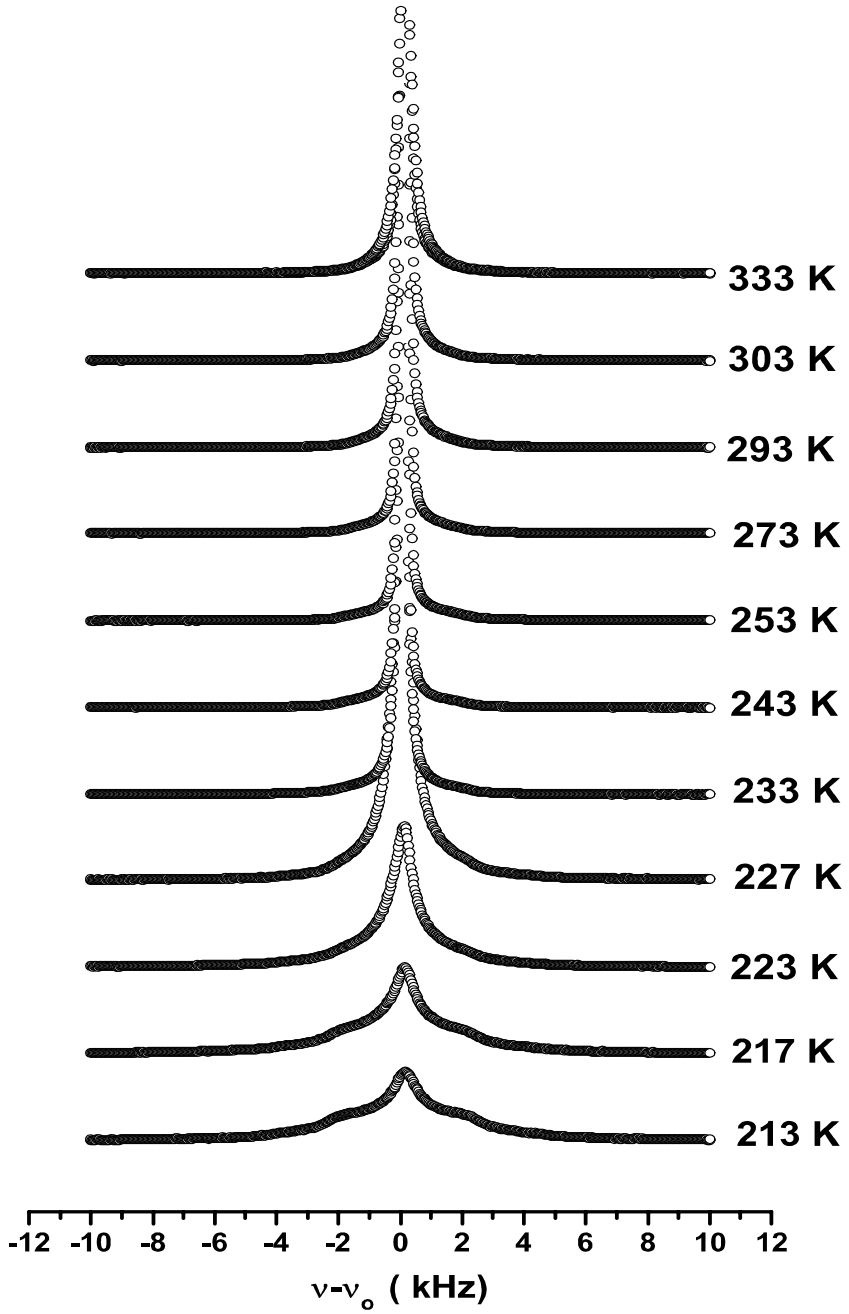

Figure A-1: ^{2}H spectra for 0.6D MCM-41 sample versus 1000/T. Spectra at the low temperature range exhibit two magnetization components.

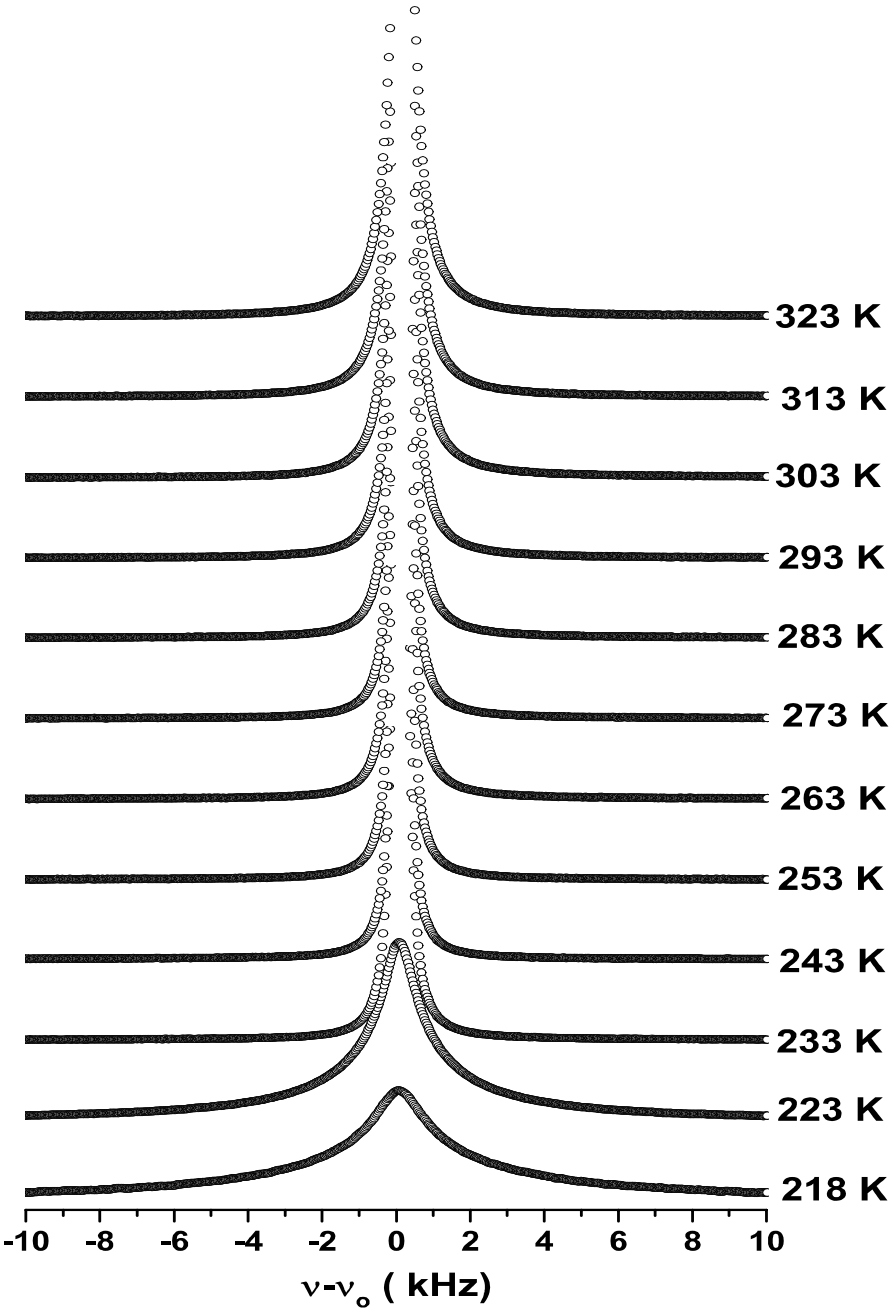

Figure A-2: ^{2}H spectra for the 1.6D sample versus 1000/T. Each spectrum exhibits a single NMR component represented by a single Lorentzian line with slight spectral change below 243 K.

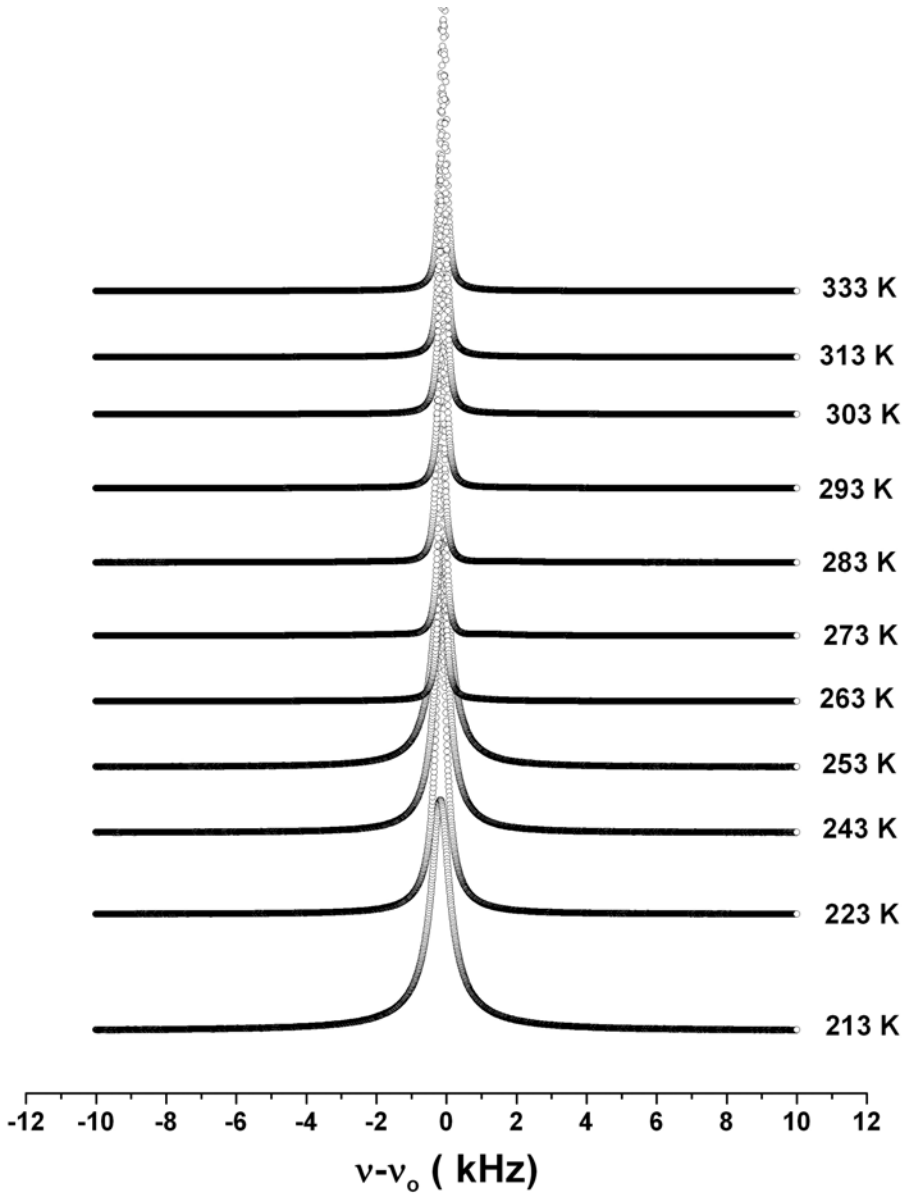

Figure A-3: ^{2}H spectra of the FullD sample versus 1000/T. Each spectrum exhibits a single NMR component represented by a single Lorentzian line.

Appendix B

Appendix: De-Convolution Script

The following is the program written within Mathcad software for de-convolution of the ^{2}H spectra for the 0.2D sample into a powder pattern and a Lorentzian line. The equations are described in Chapter 2 (pages 16).

```
ORIGIN:=1
data:=.............. // here experimental data are entered
                        as two col. frequency VS intensity.
```

$Ga(x,\beta) = \frac{1}{\beta\sqrt{2\pi}} e^{-\frac{x^2}{2\beta^2}}$ // Shape function(Gaussian).

$$f(x,\alpha,C1,base) := base + C1(-\tfrac{x}{\alpha}+1)^{-0.5} \quad if \ -2\alpha < x < -\alpha$$
$$\infty \quad if \ x = -\alpha$$
$$= base + C1\left[(-\tfrac{x}{\alpha}+1)^{-0.5} + (\tfrac{x}{\alpha}+1)^{-0.5}\right] \quad if \ -2\alpha < x < \alpha$$
$$\infty \quad if \ x = \alpha$$
$$= base + C1(\tfrac{x}{\alpha}+1)^{-0.5} \quad if \ \alpha < x < 2\alpha$$

$$Lo(\gamma,x,C2,\alpha,base) := base + \frac{2.\gamma.C2.\frac{\alpha}{\alpha}}{\pi[4.(x^2)+\gamma^2]} \quad if \ -\alpha < x < \alpha$$
$$F1(\omega',\omega_o,\alpha,\beta,C1,base) := \int_{-2\alpha}^{+\alpha} f(\omega-\omega_o,\alpha,C1,base).Ga(\omega'-\omega,\beta)dw$$
$$F2(\omega',\omega_o,\alpha,\beta,C1,base) := \int_{-\alpha}^{+\alpha} f(\omega-\omega_o,\alpha,C1,base).Ga(\omega'-\omega,\beta)dw$$
$$F3(\omega',\omega_o,\alpha,\beta,C1,base) := F2(\omega',\omega_o,\alpha,\beta,C1,base) + Lo(\gamma,x,C2,\alpha,base)$$
$$F4(\omega',\omega_o,\alpha,\beta,C1,base) := \int_{\alpha}^{+2\alpha} f(\omega-\omega_o,\alpha,C1,base).Ga(\omega'-\omega,\beta)dw$$
$$Fpowder(\omega',\omega_o,\alpha,\beta,C1,base) := \int_{\alpha}^{+2\alpha} f(\omega-\omega_o,\alpha,C1,base).Ga(\omega'-\omega,\beta)dw$$
$$F(\omega',\omega_o,\alpha,\beta,C1,C2,\gamma,base) := base + F1(\omega',\omega_o,\alpha,\beta,C1,base) + F3(\omega',\omega_o,\alpha,\beta,C1,base) + F4(\omega',\omega_o,\alpha,\beta,C1,base)$$

// Entering parameters initial values
// the following values are for ^{2}H spectrum at temperature of 233K
$\omega' := -12000, -11900..12000$ // range of the frequency axis.

$\omega_o := 0$ // center frequency for the Lorentzian line.
$C1 := 14.374$ // the pre- factor with the powder pattern equation.
$C2 := 241500$ // the pre-factor with the Lorentzian line equation.
$\alpha := 2597$ // half splitting of the powder pattern part of the spectrum.
$\beta := 488.0$ // FWHM of the shape function (Gaussian line)
$base := 4.0$ // spectrum base line.
$\gamma := 480.7$ // FWHM of the Lorentzian line.
$SSR(\omega_o, \alpha, \beta, C1, C2, \gamma, base) := \sum_{i=1}^{n} [(data^{\langle 2 \rangle})_i - F[(data^{\langle 1 \rangle})_i, \omega_o, \alpha, \beta, C1, C2, \gamma, base]]^2$
$SSR(\omega_o, \alpha, \beta, C1, C2, \gamma, base) =$
//The following are the parameters optimization step.
Given

$$\begin{pmatrix} \omega_o \\ \alpha \\ \beta \\ C1 \\ C2 \\ \gamma \\ base \end{pmatrix} := Minimize(SSR, \omega_o, \alpha, \beta, C1, C2, \gamma, base)$$

TotalAreaFit:=$\int_{-3\alpha}^{+3\alpha} F(\omega', \omega_o, \alpha, \beta, C1, C2, \gamma, base) d\omega'$

PowderPartArea:=$\int_{\alpha}^{+2\alpha} Fpowder(\omega', \omega_o, \alpha, \beta, C1, base) d\omega'$

LorentzArea:=TotalAreaFit-PowderPartArea

$$\begin{pmatrix} TotalAreaFit \\ PowderPartArea \\ LorentzArea \end{pmatrix} = \begin{pmatrix} ..... \\ ..... \\ ..... \end{pmatrix}$$

Bibliography

[1] J. Sandstrom, *Dynamics NMR Spectroscopy*, Academic Press, New York, Ch.2 (1982).

[2] M. Mehring, *Principles of High Resolution NMR in Solids*, 2nd edition, Springer-Verlag Berlin Heidelberg (1983).

[3] C. P. Slichter, *Principles of Magnetic Resonance*, Ch.3 (1996).

[4] R. C. Weast, *Handbook of Chemistry and Physics*, The Chemical Rubber Co., Ohio (1970).

[5] D. J. Griffiths, *Introduction to electrodynamics,* 2nd edition, Prentice-Hall Inc. New Jersey (1989).

[6] G. E. Pake, J. Chem. Phys. **16**, 327 (1948).

[7] R. Eggenberger, S. Gerber, H. Huber, D. Searles, M. Welker, J. Chem. Phys. **97**, 5898 (1992).

[8] D. E. Woessner, J. Chem. Phys. **40**, 2341 (1964).

[9] D. W. Hwang, A. K. Sinha, C-Yuan Cheng, T-Yan Yu, L. P. Huang. J. Phys. Chem. B, **105**, 5713-5721 (2001).

[10] A. Abragam, *The Principles of Nuclear Magnetism*, Oxford University Press: London, Ch.7 (1961).

[11] D. Canet, *Nuclear Magnetic Resonance: concepts and methods*, John Wiley & Sons Ltd. , England, p55 (1991).

[12] E. Fukushima, S. B. W. Roeder, *Experimental Pulse NMR: A nuts and bolts approach*, Addison-Wesley Publishing Company, Massachusetts (1981).

[13] D. E. Woessner, B. S. Jr, Snowden, J. Chem. Phys. **50**, 1516 (1969).

[14] J. H. Davis, In *Isotopes in the Physical and Biomedical Sciences*, edited by E. Buncel and J. R. Jones, Elsevier Science Publishers B. V., Amsterdam., **2**, 99-157 (1991).

[15] J. P. Kintzinger, in *Basics Principles and Progress*, 17^{th} ed. P. Diehl, E. Fluck, R. Kosfeld, Springer-Verlag Berlin Heidelberg, Germany, p8 (1981).

[16] H. W. Spiess, in *Developments in Oriented Polymers*, 1^{st} ed. Ward, I. M. Applied Science Publishers, London, p50 (1982).

[17] J. H. Davis, K. R. Jeffrey, M. Bloom, M. I. Valic, T. P. Higgs, Chem. Phys Lett., **42**, 390 (1976).

[18] G. H. Penner, Y. C. P. Chang, H. M. Grandin, Can. J. Chem. **77**, 1813-1820 (1999).

[19] G. Penner, *Topics in NMR spectroscopy*, University of Guelph, Guelph, Graduate Course, Winter (2006).

[20] E. Reardon, *Aqueous Geochemistry and Modeling*, University of Waterloo, Waterloo, Graduate Course, Winter (2006).

[21] E. D. Isaacs, A. Shukla, P. M. Platzman, D. R. Hamann, B. Barbiellini and C. A. Tulk, J. Phys. Chem. Solids **61** 403-406 (2000).

[22] A. Khan, J. Phys. Chem. **104**, 11268-11274 (2000).

[23] S. J. Suresh, V. M. Naik, j. Chem. Phys. **113** (21), 9727-9732 (2000).

[24] F. Franks, *Water: 2nd Edition A matrix of life*, Royal Society of Chemistry, Cambridge, 2000; can also see http://www.lsbu.ac.uk/water/ref2.html#112.

[25] A. Rahman, *One and two dimensional NMR spectroscopy*, Elsevier Science Publisher, New York, Ch.11 (1989).

[26] E. O. Stejskal, J. D. Memory, *High Resolution NMR in the Solid State: Fundamental of CP/MAS*, Oxford University Press, Oxford, Ch.2 (1994).

[27] S. Vega, *Cross polarization experiment, an coherence interpretation*, Lecture in Waterloo NMR Summer School, Waterloo (2006).

[28] S. R. Hartmann, E. L. Hahn, Phys. Rev. **128**, 2042 (1962).

[29] R. K. Harris, *Nuclear Magnetic Resonance Spectroscopy*: A physicochemical View, Longman Scientific& Technical, UK (1986).

[30] J. Liang, Master thesis, University of Waterloo, Waterloo (2006).

[31] D. E. Woessner, Mol. Phys. **34**, 4, 899-920 (1977).

[32] R. R. Ernst, G. Bodenhausen, A. Wokaun, *Principles of nuclear magnetic resonance in one and two dimensions*. Oxford University Press (1987).

[33] J. Jeener, B. H. Meier, P. Bachmann, R. R. Ernst, J. Chem. Phys. **71**, 4546 (1979).

[34] C. Schmidt, B. Blümich, H. W. Spiess, J. Magn. Reson. **79**, 269-290 (1988).

[35] A. M. Wachner, Master Thesis, University of Guelph, Guelph (1999).

[36] J. Bear, *Dynamics of Fluids in Porous Media*, Dover, New York (1988).

[37] J. Bear, Y. Bachmat, *Introduction to Modeling of Transport Phenomena in Porous Media*, Kluwer Academic, Dordrect (1991).

[38] F. A. L. Dullien, *Porous Media: Fluid Transport and Pore Structure*, Academic Press, San Diego (1992)

[39] P. M. Adler, *Porous Media: Geometry and Transport*, Butterworth-Heinemann, Boston, Oxford (1994).

[40] C. M. Case, *Physical Principles of Flow in Unsaturated Porous Media*, Clarendon Press, Oxford (1994).

[41] M. Sahimi, *Flow and Transport in Porous Media and Fractured Rock: From Classical Methods to Modern Approaches*, VCH, Weinhein (1995).

[42] S. Anandan, M. Okazaki, Microporous Mesoporous Mater., **87**, 77-92 (2005).

[43] X, Zhao, G. Q. Lu, G. J. Millar, Ind. Eng. Chem. Res. **35**, 2075-2090 (1996).

[44] G. D. Stucky, A. Monnier, F. Schüth, Q. Huo, D. Margolese, D. Kumar, M. Krishnamurty, P. Petroff, A. Firouzi, M. Jancke, B. F. Chmelka, Mol. Cryst. Liq. Cryst., **240**, 187 (1994).

[45] Q. Huo, D. I. Margolese, G. D. Stucky, Chem. Mater., **8**, 1147 (1996).

[46] J. C. Vartuli, K. D. Schmitt, C. T. Kresge, W. J. Roth, M. E. Leonowicz, S. B. McCullen, S. D. Hellring, J.S. Beck, J.L. Schlenker, D.H. Olson E. W. Sheppard, Chem. Mater., **6**, 2317(1994).

[47] C. Y. Chen. H. X. Li, M. E. Davis, Microporous Mater. **2**, 17 (1993).

[48] These images were taken from the web.

[49] F. Mansour, R. M. Dimeo, H. Peemoeller, Phys Rev E **66**, 41, p 041307/1-041307/7 (2002).

[50] J. S. Beck, J. C. Vartuli, W. J. Roth, M. E. Leonowicz, C. T. Kresge, K. D. Schmitt, C. T-W. Chu, D. H. Olson, E. W. Sheppard, S. B. McCullen, J. B. Higgins. J. L. Shlenker , J. Am. Chem. Soc.,**114**, 10834 (1992).

[51] Beck, J. S. , U. S. 5, 057, 296 (1991).

[52] C. T. Kresge , M. E. Leonowicz, W. J. Roth, J.C. Vartuli. J.S. Beck, Nature, **359**,710 (1992).

[53] A. Corma, Q. Kan, M. T. Navarro, J. Pariente, F. Rey, Chem. Mater., **9**, 2123-2126 (1997).

[54] L. Liu, G. Zhang, J.X. Dong, Tenside Surfactants Deterg, **41**, 2 (2004).

[55] B. Lindlar, A. Kogelbauer, P. J. Kooyman, R. Prins, **44-45**, 89-94 (2001).

[56] S. J. Gregg, K. S. W. Sing, *Adsorption, Surface Area and Porosity*, Academic Press, London (1982).

[57] R. Schmidt, E. W. Hansen, M. Stocker, D. Akropiaye, O. H. Ellestad, J. Am. Chem. Soc.**117**, 4049 (1995).

[58] G. D. Halsey, J. Chem. Phys., **16**, 931 (1948).

[59] S. Brunauer, P. H. Emmett, E. Teller, J. Am. Chem. Soc., **60**, 309-319 (1938).

[60] I. Langmuir, J. Am. Chem. Soc.**40**:1361- 1405 (1918).

[61] IUPAC, Manual of Symbols and Terminology for Physicochemical Quantities and Units, see sec.1.1.6; can also see http://www.iupac.org/reports/2001/colloid_2001/manual_of_s_and_t/node16.html#sec:1.1.6.

[62] R. K. Iler, *The chemistry of silica: Solubility, polymerization, colloid and surface properties*, and biochemistry, New York: Wiley (1979).

[63] K. G. Soga, Master Thesis, University of Waterloo, Waterloo (1990).

[64] E. P. Barrett, L. G. Joyner, A. Halenda, Langmuir **13**, 6267-6273 (1997).

[65] F. Rouquerol, J. Rouquerol, K. S. W. Sing, *Adsorption by powders and porous solids: principles, methodology, and applications.*, San Diego: Academic Press. xvi, P467 (1999).

[66] X. S, Zhao, G. Q. Lu, A. K. Whittaker, G. J. Millar, H. Y. Zhu, J. Phys. Chem. *B.*, **101**, 6525 (1997).

[67] J. Rathousky, M. Zukalova, A. Zukal, J. Had, Collect. Czech. Chem. Commun. **63**, 1893 (1998).

[68] C. F. Cheng, D. H. Park, J. Klinowski, J. Chem. Soc., Faraday Trans., **93**(1), 193-197 (1997).

[69] D. Baute, V. Frydman, H. Zimmermann, Sh. Kababya, D. Goldfarb, J. phys. chem. *B*, **109**, 7807-7816 (2005).

[70] H. Landmesser, H. Kosslick, W. Storek, R. Fricke, solid state Ionics **101-103**, 271-277 (1997) .

[71] J. Chen, Q. Li, H. Ding, W. Pang, R. Xu, Langmuir, **13**, 2050-2054 (1997).

[72] I. G. Shenderovich, G. Buntkowsky, A. Schreiber, E. Gedat, S. Sharif, J. Alberecht, N. S. Golubev, G. H. Findenegg, H-H. Limbach, J. Phys. Chem. B, **107**, 11924-11939 (2003).

[73] J. L. Shen , Y. C. Lee. Y. L. Lui , P. W. Cheng, C. F. J. Phys.: Condens. Matter. **15**, L297-L304 (2003).

[74] Y. Inaki, H. Yoshida, T. Yoshida, T. Hattori, J.Phys. Chem. B., 9098-9106 (2002).

[75] R. K. Iler, *The Chemistry of Silica*, Wiley: New York (1979).

[76] Y. Inaki, H. Yoshida, K. Kimura, S. Inagaki, Y. Fukushima, T. Hattori. Phys. Chem. Chem. Phys., **2**, 5293 (2000).

[77] I. S. Chuang, G. E. Maciel. J. Phys. Chem. B, **101**, 3052 (1997).

[78] A. Taguchi, F. Schüth, Microporous Mesoporous Mater., **77**,1-45 (2005).

[79] R. R. Sever, R. Alcala, J. A. Dumesic, T. W. Root, Microporous Mesoporous Mater., **66**, 53-67 (2003).

[80] D.E. Woessner, J. Magn. Reson. **39**, 297-308 (1980).

[81] K. Overloop, V. Gerven, J. Magn. Reson. A, **101**, 179-187 (1993).

[82] F. Hanus, P. Gillis, J. Magn. Reson. **59**, 437-445 (1984).

[83] K. Klier , J. H. Shen. A. C. Zettiemoyer, J. Phys. Chem. **77**, 11, 1458 (1973).

[84] V, Ostroverkhov, G. A. Waychunas, Y. R. Shen, Physcial Review Letters, **PRL94**, 046102 (2005).

[85] R. Holly, H. Peemoeller, C. Choi, M. M. Pintar, J. Chem. Phys. **108**, 10 (1998).

[86] S. Takahara, M. Nakano, S. Kittaka, J. Phys. Chem. B, **103**, 5814-1819 (1999).

[87] D. Morineau, F. Casas, C. Alba-Simionesco, A. Grosman, M. C. Bellissent-Funel, N. Ratovelomanana, J.Phys. IV France **10**, Pr7-95 to Pr7-98 (2000).

[88] Z. Tun, P. C. Mason. F. K. Mansour, H. Peemoeller, Langmuir **18**, 975-977 (2002).

[89] J. M. Zanotti, M. C. Bellissent- Funel, S. H. Chen, Phys. Rev. E, **59**, 3084 (1999).

[90] A. Spanoudaki, B. Albela, L. Bonneviot, M. Peyrard, Eur. Phys. J. E. **17**, 21-27 (2005).

[91] P. L. Llewellyn, F. Schuth,Y. Grillet, F. Rouquerol, J. Rouquerol, K. K. Unger, Langmuir **11**, 574-577(1995).

[92] K. J. Edler, P. A. Reynolds, J. W. White, D. Cookson, J. Chem. Soc. Faraday Trans. **93(1)**, 199-202 (1997).

[93] D. W. Aksnes, K. Forl, M. Stocker, Micro. Meso. Mater., **77**, 79-87 (2005).

[94] G. Dosseh, D. Morineau, C. Alba-Simionesco, J. Phys. IV France **10**, Pr7-99: Pr7-102 (2000).

[95] B. H. Wouters, T. Chen, M. Dewilde, P. J. Grobet, Microporous Mesoporous Mater., **44-45** , 453-457 (2001).

[96] E. W. Hanson, R. Schmidt, M. Stocker, D. Akporiaye, J. Phys. Chem. **99**, 4148-4154 (1995).

[97] E. W. Hanson, M. Stocker, R. Schmidt, J. Phys. Chem. **100**, 2195-2200 (1996).

[98] D. Akporiaye, E. W. Hansen, R. Schmidt, M. Stocker, J. Phys. Chem. **98**, 7, 1926-1928 (1994).

[99] B. Grünberg, T. Emmler, E. Gedat, I. Shenderovich, G. H. Findenegg, H. H. Limbach, G. Buntkowsky, Chem. Eur. J. **10**, 5689-5696 (2004).

[100] S. Pizzanelli, S. Kababya, V. Frydman, M. Landau, S. Vega, J. Phys. Chem. B. **109**, 8029-8039 (2005).

[101] J. Trebose, J. W. Wiench, S. Huh, V. S. Y. Liu, M. Pruski, J. Am. Chem. Soc. **127**, 3057-3068 (2005).

[102] P. J. Branton, P. G. Hall, K. S. W. Sing, J. Chem. Soc. Chem. Commun. 1257 (1993).

[103] NMR Nomenclature: Nuclear spin properties and conversions for chemical shifts- IUPAC recommendations, J. Magn. Reson. **156**, 323-326 (2002).

[104] A. J. Benesi, M. W. Grutzeck, Bernie, O'Hare, J. W. Phair, Langmuir, **21**, 527-529 (2005).

[105] H. W. Spiess, B. B. Garrett, R. K. Sheline, J. Chem. Phys. **51**, 1201 (1969).

[106] P. Waldstein, S. W. Rabideau, J. Chem. Phys. **41**, 3407 (1969).

[107] C. Amman, P. Meier, A. E. Merbach, J. Magn. Reson. **46**, 319-321 (1982).

[108] A. D. Ronemus, R. L. Vold, R. R. Vold, J. Mangn. Res. **70**, 416-426 (1986).

[109] E. S. Mananga, Y. S. Rumala, G. S. Boutis, J. Magn. Res. **181**, 296-303 (2006).

[110] Y. H. Chen, L. P. Hwang, J. Phys. Chem. B. **103**, 5070 (1999).

[111] S. Macura, Y. Huang, D. Suter, R. R. Ernst, J. Magn. Reson. **43**, 259-281 (1981).

[112] S. Macura, K. W*ü*thrich, R. R. Ernst, J. Magn. Reson. **46**, 269-282 (1982).

[113] M. Auger, D. Carrier, I. C. P. Smith, H. C. Jarrel, J. Am. Chem. Soc. **112** (4), 1373 (1990).

[114] A. J. Vega, Z. Luz, J. Chem. Phys. **86** (4), 1803 (1987).

[115] F. A. Bovey, L. Jelinski, P. A. Mirau, *Nuclear Magnetic Resonance Spectroscopy*, 2^{nd} ed., AT&T Academic press, California, USA, section 8.8, p422 (1988).

[116] M.S. Greenfield, A. D. Ronemus, R. L. Vold, R. R. Vold, P.D. Ellis, T. E. Raidy, J. Magn. Reson. **72**, 89 (1987).

[117] R. R. Vold, R. L. Vold in *Advance in Magnetic and Optical Resonance*, edited by W. S. Warren, Academick, San Diego, 16, p85 (1991).